National Atmospheric and Oceanic Administration under Grant NA67RJ0152 Amend. 34

SENSITIVITY OF THE SOIL MOISTURE INITIALIZATION IN THE GENESIS OF TWO SIMULATED MESOSCALE CONVECTIVE SYSTEMS

by William Y. Y. Cheng

William R. Cotton, P.I.

Colorado State University

Department of Atmospheric Science

Paper No. 731

SENSITIVITY OF THE SOIL MOISTURE INITIALIZATION IN THE GENESIS OF TWO SIMULATED MESOSCALE CONVECTIVE SYSTEMS

by

William Y. Y. Cheng

Department of Atmospheric Science

Colorado State University

Fort Collins, Colorado 80523

Research Supported by

National Atmospheric and Oceanic Administration

under Grant NA67RJ0152 Amend 34

November 26, 2002

Atmospheric Science Paper No. 731

ABSTRACT

SENSITIVITY OF THE SOIL MOISTURE INITIALIZATION IN THE GENESIS OF TWO SIMULATED MESOSCALE CONVECTIVE SYSTEMS

This study examines the sensitivity of the horizontal heterogeneities of the soil moisture initialization (SMI) in the cloud-resolving grid of two real-data mesoscale convective system (MCS) simulations during their genesis phase. We used a nested grid setup similar to some of the current realtime forecast models. Both systems were quasi-stationary. One system (Case 980726) formed in the Texas/Oklahoma border with a lifetime of 9h (from 2200 UTC, 26 July to 0700 UTC, 27 July 1998). The other system (Case 990802), also with a lifetime of 9 h, initiated in western Oklahoma around 1945 UTC, 2 August 1999 and dissipated around 0445 UTC, 3 August 1999.

Soil moisture for the finest nested grid (the cloud-resolving grid) was derived from the Antecedent Precipitation Index (API) using 4-km grid spacing precipitation data for a three-month period. In order to test the sensitivity of the heterogeneities of the SMI in the cloud-resolving grid, i) Barnes objective analysis was used to alter the resolution of the SMI, ii) the amplitude of the soil moisture field was reduced by 50%, iii) the position of a soil moisture anomaly was altered, and iv) two experiments with homogeneous soil moisture (31% and 50% saturation) were performed.

All of the experiments in Case 980726 with heterogeneous SMI produced a MCS with a quasi-circular cloud shield, similar to the observed timing, size and location. Even the experiment with a homogeneous SMI at 31% saturation produced a MCS with a quasi-circular

cloud shield. However, convection was delayed in the experiment with a homogeneous SMI at 50% saturation, and the evolution of the convective system differed substantially from the experiments with heterogeneous SMI or homogeneous SMI at 31%. The experiments in Case 990802 did not perform as well as Case 980726, but the model was able to reproduce some aspects of the observed system.

Large-scale forcing provided the favorable environment for convection to develop, but the distribution of the soil moisture determined where convection was likely to occur. The soil moisture anomalies generated physiographic-induced mesoscale systems (PIMSs), analogous to sea breeze, due to differential surface heating, and they assisted in organizing the convection as the MCS was developing. The larger soil moisture anomalies were more influential in initiating and/or interacting with convection. As the initial soil moisture was smoothed, the PIMSs associated with the larger soil moisture anomalies started to strengthen, but as the smoothing reached a cutoff wavelength of 80 km, the PIMSs began to weaken. Although the effects of the smaller soil moisture anomalies were not negligible in initiating and/or enhancing convective precipitation, they tended to lose their signatures with the smoothing operation. In the experiments, a negative feedback existed between wet soil and convective precipitation which tended to suppress convection over wet soil but favored convection at the periphery of the wet soil. Long-lived convective cells tended to track around the wet soil and to develop at the periphery of the wet soil.

William Y. Y. Cheng
Department of Atmospheric Science
Colorado State University
Fort Collins, Colorado 80523
Fall 2002

ACKNOWLEDGEMENTS

I would like to sincerely thank my advisor, Prof. Bill Cotton, for his guidance, suggestions and the opportunity to pursue my studies at CSU. Bill is down-to-earth and a great boss to work for. I also thank my committee members, Profs. Scott Denning, Paul Mielke, and Roger Pielke, for their suggestions, and their time for serving on my committee and reviewing this work.

I appreciate Chris Golaz's assistance during the past four years in working with RAMS, as well as providing other technical assistance. I also thank Ray McAnelly for his help in working with satellite and radar data, as well as numerous other assistance. Steve Saleeby is thanked for providing the API code, answering questions on RAMS and for being a messenger between our group and Bob Walko. I am also grateful for other (past and current) members of the Cotton group (especially Travis Ashby, Gustavo Carrió, Brian Gaudet, Louis Grasso, Hongli Jiang, Israel Jirak, Jeremy Krieger, Cristian Mitrescu, Jason Nachamkin, Scot Rafkin, Chris Rozoff, Sue Van den Heever, and Bob Walko), as well as Adriana Beltan, Chris Castro and Lixin Lu for their various assistance.

My thanks are extended to our past and current system administrators in our group, Jason Connor and Todd Gamber, respectively, for their great help in computer-related issues. I also thank Brenda Thompson for her help in administrative matters.

Prof. Pielke is acknowledged for suggesting the use of the NDVI dataset which was provided by Brad Reed and Susan Maxwell at USGS. I also thank Kevin Schaefer and Joe Eastman for their help in working with the NDVI dataset.

This reaserch was funded by NOAA under grant NA67RJ0152 Amend 34.

TABLE OF CONTENTS

1 INTRODUCTION **1**

2 BACKGROUND **3**

2.1 Physiographic-Induced Mesoscale Systems 3

2.1.1 Effects of heterogeneous vegetation 4

2.1.2 Effects of soil moisture 6

2.1.3 Effects of soil moisture and vegetation 11

2.2 Mesoscale Convective Systems 12

2.2.1 Squall lines 13

2.2.2 Mesoscale convective complexes 15

2.3 Motivation and Hypotheses 17

3 NUMERICAL MODEL AND METHODOLOGY **23**

3.1 Numerical Model 23

3.2 Soil Moisture 24

3.3 Normalized Difference Vegetation Index 27

4 JULY 26, 1998 MCS CASE **31**

4.1 Case 980726 31

4.2 Model Setup/Initial Conditions 32

4.2.1 Soil moisture and sensitivity experiments 34

4.3 Model Results 36

4.3.1 Grid 1 36

4.3.2 Grid 2 37

4.3.3 Pre-genesis phase: grid 3 38

4.3.4 Genesis phase: grid 3 41

4.4 Discussion 46

5 AUGUST 2, 1999 MCS CASE **83**

5.1 Case 990802 83

5.2 Model Initial Conditions 84

5.2.1 Model setup/initial conditions 84

5.2.2 Soil moisture and sensitivity experiments 86

5.3 Model Results 86

5.3.1 Grid 1 86

5.3.2 Grid 2 87

5.3.3 Pre-genesis phase: grid 3 88

5.3.4 Genesis phase: grid 3 89

5.4 Discussion 93

6 Unresolved Issues, Summary, and Future Work **127**

6.1 Unresolved Issues 127

6.1.1 Starting the model one day earlier 127

6.1.2 Effects of vegetation 128

6.1.3 Soil moisture-moist convection feedback 129

6.2 Summary 132

6.3 Suggestions for Future Work 135

Chapter 1

INTRODUCTION

The interaction between the Earth's surface and the overlying atmosphere is a major cause of cumulus convection (Pielke 2001). One important boundary condition in the land surface is the soil moisture. Soil moisture, next to sea-surface temperature (SST), is the second most important factor in controlling the predictability of the atmosphere (Dirmeyer and Shukla 1993; Dirmeyer 1995). Soil moisture has a memory on the time scale of 200-300 days (Liu and Avissar 1999; Pielke et al. 1999a) and according to Shukla (cited in Dirmeyer 1995), as a boundary condition, soil moisture may perhaps be more important than SST over the extratropical continents in the spring and summer. Soil moisture is also an important component of the hydrological cycle (Dirmeyer and Shukla 1993). In addition, initial soil moisture is known to have impact on climate simulations (Pielke et al. 1999a) and medium range forecasts (Yang et al. 1994) as well as short term simulations, e.g., 48 h or less (Bernardet and Cotton 1998; Grasso 2000b; Nachamkin and Cotton 2000). The variabilities of the soil moisture and other landscape variables are important in mesoscale and cumulus processes over land during the summer (Pielke et al. 1998). Soil moisture affects the soil heat capacity and shortwave albedo of the surface (Entekhabi et al. 1996). Furthermore, soil moisture has strong influence on the partitioning of surface latent and sensible heat fluxes, boundary layer evolution, and convective stability (Pielke 2001).

The effects of soil moisture on moist convection has been studied by various researchers, e.g., Yan and Anthes (1988), Emori (1998), Nachamkin and Cotton (2000), and Ashby et al. (2001). However, few studies have focussed the effects of soil moisture on a special kind of convective system, the mesoscale convective system (MCS), with the exception of Nachamkin and Cotton (2000) (also documented in Bernardet et al. 2000). The purpose of this study is to investigate the effects of soil moisture in the genesis of MCSs in cloud-resolving simulations. The outline of this dissertation is as follows. Chapter 2 covers the past research on soil moisture, vegetation, and MCSs, followed by the motivation and hypotheses of this study. Chapter 3 provides a brief description of the numerical model and the methodology employed. Chapter 4 presents the results of the sensitivity of the soil moisture initialization on a simulated MCS in the Texas/Oklahoma panhandle region in July 1998. The sensitivity of a second simulated MCS in August 1999 to the initial soil moisture is covered in Chapter 5. Finally, the summary of this study and suggestions for future work are presented in Chapter 6.

Chapter 2

BACKGROUND

2.1 Physiographic-Induced Mesoscale Systems

Surface heterogeneities in soil moisture, vegetation type or soil type can induce mesoscale circulations through surface sensible heat flux gradients (Pielke and Segal 1986; Segal and Arritt 1992; Pielke 2002). These surface sensible heat flux gradients result from spatial variations in surface evapotranspiration, solar irradiance reflection/absorption and thermal energy storage of the surface. Pielke (2002) identified these thermally-induced circulations as physiographic-induced mesoscale systems (PIMS). These PIMSs, much like sea breeze, can provide regions of convergence, triggering deep convection (Pielke 2001). A schematic of a PIMS is displayed in Fig. 2.1. Due to the different surface characteristics, the land patch on the left hand side is cooler (due to lower surface sensible heat flux) than the patch on the right hand side. As a result, warmer (cooler) air on the right (left) patch rises (sinks), and a PIMS develops. Most researchers have mainly focused on mesoscale circulations induced through heterogeneities in vegetation or soil moisture. An excellent review paper by Pielke (2001) covers many of the past research on the effects of vegetation and soil on convective rainfall.

2.1.1 Effects of heterogeneous vegetation

Vegetated regions are in general cooler than surrounding non-vegetated land due to difference in evapotranspiration. Thus, differential surface heating can also be created due to the heterogeneities in vegetation inducing PIMS. Segal et al. (1988) evaluated the effects of vegetation on PIMSs in northeastern Colorado and San Luis Valley in Colorado. They found that for mesoscale domains covered by an extended area of very dense vegetation (not under water or environmental stress) adjacent to bare soil area, the induced PIMS was comparable in magnitude to that of sea breeze. Reductions in the density of vegetation coverage (typical in most real world situations) reduce the impact of the PIMS induced by heterogeneous vegetation. Segal et al. (1989) investigated the impact of crop areas in northeastern Colorado on PIMSs during the midsummer by using observations and modeling. They found that the temperature contrast between crop and non-crop areas to be on the order of 10 K. However, during the daytime, the synoptic flow and the elevated, terrain-forced (i.e., thermally induced by heating over elevated terrain) flow masked the signature of the PIMS induced by the irrigated crop/dry land temperature contrast. Their result was also supported by their modeling study.

Pielke et al. (1997) performed sensitivity experiments to test the importance of landscape on thunderstorm development in the Texas/Oklahoma region. In one simulation, they used the current landscape (irrigated crops, shrubs, natural short-grass prairie) and the model produced deep convection. In the second experiment, they used just the natural landscape (short-grass prairie) and the model produced only shallow convection.

Stohlgren et al. (1998) studied the impact of the of landscape change in the plains of Colorado on the regional climate of the adjacent natural areas in the Rocky Mountains. Using a regional model, they found that alterations of the natural vegetation in the plains,

principally as a result of agriculture and urbanization, produced lower temperature in the mountains. The regional cooling can be attributed to the cooler and more humid air (from the plains as a result of irrigation) being advected to higher elevations by the upslope flow.

Greene et al. (1999) performed sensitivity studies of landscape in a regional climate model covering the entire continental United States (CONUS). The model included a parameterization for snowcover and snowmelt. In order to test the effects of deforestation, in one experiment, they used the *current vegetation distribution* (Run 1), and in another, *the trees were replaced with short grass prairie* to represent *deforestation* (Run 2). In Run 2, there was an 18% change (compared to Run 1) in the vegetation type across the entire domain, modifying the surface characteristics such as albedo, roughness, transmissivity of the vegetation canopy to incoming solar radiation, and leaf area index. Greene et al. (1999) found that in the deforestated simulation (Run 2), the temperatures were lower (higher) in the winter (summer). The summer result is easily explained by the lower evapotranspiration in the summer in Run 2 due to a lower leaf area index, thus a higher summer temperature. The winter result can be explained by the difference in albedo. For grasslands covered with snow in the winter, the albedo is equal to that of snow. For trees, the snow is masked by protruding vegetation, and the effective albedo is very close to the value of trees. Thus, with less trees and more grassland in Run 2, the albedo would be higher in the winter, leading to a lower temperature.

Pielke et al. (1999b) studied the influence of the landscape changes on summer weather in south Florida. Using a regional model, they performed a two-month integration with three sets of landscape: i) the observed landscape in 1973, ii) the landscape in 1993, and iii) the landscape in 1900. The 1900 landscape, prior to large anthropogenic changes, corresponded closely to the natural landscape. Pielke et al. found that in the two-month period over south Florida, there was a 9% (11 %) reduction in precipitation with the 1973 (1993)

landscape, using the 1900 landscape as a baseline. The average maximum temperature within the two-month period in south Florida increased by approximately 0.5 K between the 1900 and 1993 simulations. Pielke et al. verified the above results with the available (albeit limited) observations.

2.1.2 Effects of soil moisture

Soil moisture can be modified by precipitation or irrigation (Pielke and Segal 1986), and the influence of soil moisture on atmospheric circulation and convection has been investigated by various researchers in modeling studies. In an idealized experiment, Ookouchi et al. (1984) placed two land patches of different soil moisture availability (S_m, Manabe 1969) adjacent to one another. The soil moisture availability is defined by:

$$S_m = \frac{E}{E_p}, \tag{2.1}$$

where E is the surface evaporation rate and E_p is the potential surface evaporation rate. In an extreme case with one land patch with S_m of 1.0 adjacent to another land patch with S_m of 0.05, the maximum wind speed reached 4.5 m s^{-1} and the maximum temperature difference between the two land patches reached 13 K. These values are comparable to those of sea breeze in their study (5.6 m s^{-1} and 21 K). As mentioned earlier, similar temperature contrast ($\approx$10 K) has also been observed over irrigated areas/non-irrigated areas (Segal et al. 1989). In a less extreme case with one land patch with S_m of 0.1 adjacent to a land patch with S_m of 0.05, the maximum wind speed reached 2 m s^{-1}, while the maximum temperature difference between the two land patches reached 4 K.

McCorcle (1988) investigated the effects of soil moisture on the Great Plains low-level jet. The moisture transport, boundary layer convergence and vertical motion associated with the Great Plains low-level jet are important in nocturnal convection over the Great

Plains region. Due to the solar heating of the sloping terrain, a thermally direct circulation develops in which the buoyancy driven wind, pointing upslope during daytime, is turned clockwise by the Coriolis force, and contributes to the background southerly flow (Holton 1967). McCorcle (1988) found that wetter (drier) soil over the Great Plains strengthens (weakens) this buoyancy-driven component of the jet and its associated upward motion and nocturnal convection. On the other hand, wetter soil over the Rocky Mountains weakens the buoyancy-driven wind, thus diminishes the low-level jet and associated nocturnal convection. Ookouchi et al. (1984) had similar findings in their idealized study with sloping terrain. Specifically, Ookouchi et al. found that moistening the soil of the lower (higher) elevations of the slope created an anomalous mesoscale circulation that strengthened (weakened) the upslope flow due to alteration of the thermal gradients.

Yan and Anthes (1988), in a 2D idealized model, placed strips of dry and moist land adjacent to each other in a convectively unstable environment. They found that strips of 100-200 (24 and 48) km in width were (were not) effective in initiating convective precipitation.

Fast and McCorcle (1991) imposed idealized soil moisture distribution in a hydrostatic model with moist physics to study the effects of heterogeneous soil moisture on the passage of a summer cold front in the central United States. The model atmospheric conditions were initialized with real data. Heterogeneous soil moisture did not affect the position of the front, but the thermal and wind fields were sufficiently altered. Heterogeneous soil moisture altered the surface air temperature (surface specific humidity) by up to 6 K (7 g kg^{-1}).

Chen and Avissar (1994a) investigated the impact of spatial variation of land surface wetness on mesoscale heat fluxes, and found that the strongest mesoscale heat fluxes occurred for surface forcings with wavelengths corresponding to the local Rossby radius of

deformation (80-130 km). In earlier research by Dalu et al. (1991) as well as Dalu and Pielke (1993), they found similar results with idealized models in their investigation of the impact of surface thermal inhomogeneities on atmospheric flow. In a followup study, Chen and Avissar (1994b) found that strongest precipitation, from shallow convection, occurred when the wavelength of the land surface moisture discontinuity was close to the local Rossby radius (80-140 km). Even when the length scale of the land surface moisture discontinuity was on the order of 20 km, the induced mesoscale circulations could still produce strong precipitation. The results of Chen and Avissar (1994b) seem to differ from those of Yan and Anthes (1988) in which they found that strips of wet/dry land of 24 and 48 km in width were not effective in generating convective precipitation.

In a medium-range forecast (10 days), Yang et al. (1994) used the errors in surface air temperature and surface relative humidity to adjust the initial soil moisture. With the adjusted initial soil moisture, the first 5-day mean surface air temperature and mean surface relative humidity forecast errors over the relatively dry portion of the domain were reduced from 2.9 to 1.1 (2.4 to 1.3) ^{o}C and from 15 to 7.6% (15 to 8%) in the first (second) experiment.

Castelli and Rodriguez-Iturbe (1995) used a 2D semi-geostrophic model to study the influence of soil moisture-atmosphere in baroclinic instability. They found that when the ascending-moist (descending-dry) areas of the baroclinic wave developed on top of a wetter (drier) soil, the frontal collapse was reached sooner and the estimated precipitation higher. This is consistent with observations by Namias (1959) in which he found that soil moisture anomalies could assist in maintaining the persistence of atmospheric circulation anomalies. In particular, an anomalous trough over a moist soil area prevents the buildup of an upper-level ridge, and regions of dry soil (as a result of drought) are associated with an anomalous upper-level ridge.

Pan et al. (1996) investigated the effect of the soil moisture availability on the subgrid-scale precipitation in the Grell (1993) and the Anthes-Kuo (Kuo 1974; Anthes 1977) convective parameterization schemes (CPSs) in a real-data simulation with MM5. They found that the soil moisture impact was exaggerated in the Anthes-Kuo scheme when compared to the Grell scheme and the explicit moisture scheme (Hsie et al. 1984). In the Anthes-Kuo scheme, the subgrid-scale precipitation is largely a function of the integrated water vapor convergence, thus the subgrid-scale precipitation's sensitivity to the surface moisture flux. Pan et al. (1996) conjectured that in the Grell scheme, the subgrid-scale precipitation is influenced by the anomalous water vapor indirectly through the cloud work function (Arakawa and Schubert 1974), a quantity related to available moist static energy (or available moist enthalpy). They argued that variations in soil moisture did not alter the moist enthalpy flux from the surface, thus the smaller sensitivity of soil moisture in the Grell CPS. However, their argument about the Grell CPS was flawed. Pielke (2001) showed that the moist enthalpy is indeed very sensitive to changes in water vapor mixing ratio, more so than the temperature. Perhaps, there are other possible reasons for their results.

Koch et al. (1997) used satellite imagery and rain gauge data to improve on the initialization of relative humidity and surface moisture availability in a mesoscale simulation of a cold-frontal squall line. Proper representation of the evapotranspiration and atmospheric humidity was essential in simulating the rapid development of the squall line.

Emori (1998) used a 2D model (500 km wide at 2 km grid spacing) to investigate the interaction of cumulus convection with soil moisture distribution. He started out with a horizontally homogeneous soil moisture initialization and the model was initialized with a single sounding. As convection developed, wet and dry soil patches developed. Emori found that convection preferentially occurred over drier soil. Thus, Emori discovered a negative feedback between soil moisture and convective precipitation.

Gallus and Segal (2000) investigated the sensitivity of the convective precipitation in a small simulated convective system to soil moisture and CPS. In the experiments with the Kain-Fritsch convective parameterization scheme (Kain and Fritsch 1990), the larger initial soil moisture values delayed the onset of convection, but the precipitation maximum decreased with increasing soil moisture. This has to do with the fact that wetter soil tended to inhibit vertical motion, and the trigger function in the K-F depends on the vertical motion. In another set of experiments with Betts-Miller-Janjic CPS (Betts 1974; Betts and Miller 1986; Janjic 1994)[1], wetter soil tended to increase the precipitation maximum. For the experiments with Betts-Miller-Janjic CPS, the domain-accumulated precipitation increased with increasing soil moisture. The domain-accumulated convective precipitation was more complicated in the experiments with Kain-Fritsch CPS. For the 12-h (18-h) accumulation, wetter soil tended to increase (decrease) the domain-accumulated convective precipitation.

Grasso (2000b) tested the sensitivity of soil moisture initialization on a simulated dryline over Oklahoma (also in Bernardet et al. 2000). He found that heterogeneous soil moisture initialization was necessary in order for the model to produce the dryline. In an experiment with homogeneous soil moisture initialization, the dryline did not develop. Grasso found that soil moisture heterogeneites aided in the development and movement of the dryline. Moist soil areas increased the low-level water vapor mixing ratio. Differential heating as a result of soil moisture heterogeneites created PIMSs that assisted in converging water vapor between the two moist soil areas, leading to enhancement of the low-level water vapor mixing ratio gradient, thus strengthening the dryline. Also, the PIMSs aided in the eastward acceleration of the winds at the dry side of the dryline by enhancing the east-west pressure gradient. In an earlier work for his Ph.D. research, Grasso (1996) also found

[1]The Betts-Miller-Janjic CPS nudges the temperature and moisture to a specified reference profile.

similar results in the sensitivity of the soil moisture initialization in two simulated drylines. As in Grasso (2000b), Grasso (1996) found that with only homogeneous soil moisture initialization, the model was unable to produce a dryline. However, with heterogeneous soil moisture initialization, the model was able to produce a dryline when a long and thin region in the domain was preferentially heated, leading to rising motion in this region. Thus, low-level (moisture) convergence ensued, enhancing the moisture gradient in the dryline.

Nachamkin and Cotton (2000) used the Antecedent Precipitation Index (API, Chang and Wetzel 1991) method to initialize the soil moisture in a MCS simulation in northeastern Colorado on July 19, 1993. Because of the dry bias of the soil moisture (obtained from the API method) over the mountains, the soil moisture had to be altered to reduce the unrealistically high Mountain-Plains solenoidal circulation (Tripoli and Cotton 1989a,b) in order to achieve a more realistic simulation.

Golaz et al. (2001) studied the influence of soil moisture on cumulus clouds over land in large-eddy simulations (LESs). They found that the surface flux was dominated by latent (sensible) heat flux for wetter (drier) soil. In addition, they found that simulations dominated by sensible heat flux tended to have a more turbulent boundary layer and a higher cloud base. On the other hand, experiments dominated by latent heat flux had fewer but more intense updrafts in the cloudy regions.

2.1.3 Effects of soil moisture and vegetation

Chang and Wetzel (1991) examined the spatial variations of soil moisture and vegetation of the prestorm environment. They performed three experiments: i) VEG, ii) NOVEG, and iii) NOSPA. In VEG, the fractional coverage of vegeation and the soil moisture were horizontally heterogeneous. In NOVEG, the fractional coverage of vegetation was assumed

to be homogeneous, while the soil moisture was horizontally heterogeneous. In NOSPA, both fractional coverage and soil moisture were homogeneous. Small scale features present in the low-level divergent wind pattern for both VEG and NOVEG were absent in NOSPA. These small scale features could be important in determining the timing and location of local severe storms.

Clark and Arritt (1995) tested the sensitivity of soil moisture and vegetation cover in convective precipitation with a 1-D model with the Kain and Fritsch (1990) convective parameterization scheme (K-F CPS). Larger values of initial soil moisture delayed the timing of convection, consistent with the results of Gallus and Segal (2000). Clark and Arritt (1995) also found that increasing the initial soil moisture increased the accumulated convective precipitation. This result is similar to that of Gallus and Segal (2000). Clark and Arritt also found that vegetation cover enhanced convection, causing convection to occur earlier and the convective precipitation to be greater. Convection did not initiate over dry, bare soil, while moist, fully vegetated soil produced the most convective precipitation.

Pielke et al. (1999a) investigated the impact of altering the initial soil moisture and vegetation type in a seasonal regional climate simulation. They varied the amount of soil moisture and the current vegetation type. In their study, tall and short grasslands have been removed and replaced with agricultural regions to simulate the impact of human agricultural activities. The effect of decreased soil moisture resulted in a domain-wide increase in maximum daily temperature. However, the current vegetation tended to decrease the domain-averaged maximum daily temperature. In addition, they found that the interaction between soil moisture and vegetation was small.

2.2 Mesoscale Convective Systems

Mesoscale convective systems (MCSs) are a special class of convective system with horizontal length scales ranging from 20 to 500 km. MCSs contain organized convective circulations on the mesoscale which are distinct from the circulations of the individual convective cells and the synoptic circulation in which the mesoscale circulations are embedded (Zipser 1982). MCSs are ubiquitous; they can be found in the tropics as well as the mid-latitudes. MCSs account for a large percentage (30-70%) of summer rainfall in the central United States (Fritsch et al. 1986). In addition, MCSs such as squall lines and mesoscale convective complexes (MCCs) are associated with a large portion of severe weather during the spring and summer, especially flood-producing storms (e.g., Midwest floods of 1993: Kunkel et al. 1993; Bell and Janowiak 1995). On the other hand, too few MCSs in the central United States leads to drought. Hence, MCSs are important from a climatological and weather forecasting perspective.

Mesoscale convective systems often possess an extensive middle to upper tropospheric stratiform-anvil cloud of several hundred kilometers in horizontal dimension (Cotton and Anthes 1989) which appear as large cold cirrus cloud shields (Maddox 1980). Typical lifetime of MCSs is between 6 to 12 h, and sometimes, the stratiform-anvil region of the system can survive up to several days (Cotton and Anthes 1989). Two main types of MCSs are squall lines and MCCs[2]. Squall lines are a more linear MCS in which convective cells are organized as lines or bands. During the mature stage, squall lines are accompanied by light, stratiform precipitation areas i) ahead of or straddling the convective line, ii) or to the rear of or trailing the convective line (Johnson and Hamilton 1988). On the other hand, MCCs possess more circular cloud shields (Maddox 1980). However, some MCSs

[2]In the tropics, MCCs are called tropical cloud clusters (Cotton and Anthes 1989).

appear to be MCCs from a satellite perspective, but may look like squall lines from a radar perspective (Djurić 1994).

2.2.1 Squall lines

Using observations from the OK PRE-STORM[3] field campaign, Johnson and Hamilton (1988) observed many common squall line features that have emerged from previous studies (see summary in Cotton and Anthes 1989). The squall line air-relative flow contains two main currents (Fig. 2.2a): i) a sloping front-to-rear flow originating from low levels (ahead of the surface gust front) to high levels in the rear and ii) *rear-inflow jet* (coined by Smull and Houze 1987b). In a squall line with trailing stratiform precipitation, Johnson and Hamilton (1988) observed three surface pressure signatures: i) the pre-squall mesolow, ii) the squall mesohigh, and iii) the wake low (Fig. 2.2b).

The front-to-rear flow transports hydrometeors rearward from the convective line to the stratiform region where they contribute to the precipitation there (Smull and Houze 1985; Rutledge and Houze 1987). Additional precipitaton in the stratiform region comes from i) successive incorportation of old convective cells from the convective line and ii) the in situ production of new condensate by a mesoscale updraft (Brown 1979; Gamache and Houze 1982; Rutledge 1986; Smull and Houze 1987a; Rutledge and Houze 1987).

The rear-inflow jet descends towards the convective line through the stratiform region. The rear-inflow jet and its associated mesoscale descent appear to play an important role in determining the pressure distribution to the rear of the squall line. The wake low, a result of subsidence warming, is a surface manifestation of the descending rear-inflow jet. The subsidence warming is strongest at the back edge of the precipitation area where the evaporative cooling is too weak to offset the strong adiabatic warming.

[3]OK PRE-STORM stands for Oklahoma-Kansas Preliminary Regional Experiment for STORM-Central.

According to Hoxit et al. (1976), the pre-squall mesolow is caused by subsidence warming in the mid-to-upper troposphere ahead of the squall line. The squall mesohigh, rear of the squall line, is co-located with areas of heavy precipitation and convective downdrafts. Sawyer (1946) and Fujita (1959) attributed the mesohigh primarily to rainfall evaporation. However, Fujita (1959) noted that in certain situations, there could be additional nonhydrostatic contribution to rise in surface pressure by the precipitation downdraft impacting the ground. Hydrometeor loading could also contribute to the mesohigh (Sanders and Emanuel 1977).

Squall lines take on different forms of organization. Bluestein and Jain (1985) studied a 11-year radar reflectivity dataset from the National Severe Storms Laboratory in Norman, Oklahoma, and they found four types of (severe) squall lines: i) *broken line*, ii) *back building*, iii) *broken areal*, and iv) *embedded areal* (Fig. 2.3). *Broken line* formation has a tendency to form along cold fronts in a multicell environment (relatively weak vertical shear and large CAPE), whereas *back building* forms along any boundary in a supercell environment (high CAPE, moderate to high shear, high relative helicity). *Broken areal* squall lines develop from interaction of thunderstorm outflow boundaries. *Embedded areal* squall lines may be examples of warm-frontal bands and wide cold-frontal bands, and occur when a convective line appears within a larger area of stratiform precipitation. *Embedded areal* squall lines possess relatively low values of CAPE, and probably develop through some hydrodynamic instability or ducted gravity waves. Of the four modes documented by Bluestein and Jain (1985), the *embedded areal* mode occurs the least frequently.

2.2.2 Mesoscale convective complexes

The MCC represents a more circular MCS, and the exact definition was first introduced by Maddox (1980) and is shown in Table 2.1. From a composite obtained from ten MCC

cases, Maddox (1983) found common large-scale features associated with the development of MCCs in the United States, such as weak mid-level short-wave trough, east-west quasi-stationary front, low-level jet coupled with strong low-level θ_e advection. Specifically, MCCs typically form in the vincinity of a weak surface front, with a pronounced, southerly low-level jet transporting warm, moist air into the region. While MCC formation is linked to a weak, eastward propagating short-wave trough at midlevels, the primary forcing apparently is due to low-level warm advection. Cotton et al. (1989) and Laing and Fritsch (2000) found similar results for MCCs in the central United States and worldwide, respectively. In addition, Maddox (1983) found that the MCC is a warm-core (cold-core) system in the mid-troposphere (upper-troposphere). Low to mid-level convergence feeds a strong upward mass flux. The warm-core structure results in a meso-anticyclone and strong outflow at upper levels, but the relative flow at midlevels is very light.

Table 2.1: The definition of Mesoscale Convective Complex (Maddox 1980)

Size	(A) Cloud shield with IR temperature $\leq$ -32 ^{o}C, must have an area $\geq$ 100,000 km^2 (B) Interior cold cloud region with temperature $\leq$ -52 ^{o}C, must have an area $\geq$ 50,000 km^2
Initiate	Size definitions A and B are first satisfied
Duration	Size definitions A and B must be met for a period $\geq$ 6h
Maximum extent	Continuous cold cloud shield (IR temperature $\leq$ -32 ^{o}C) reaches maximum size
Shape	(minor axis/major axis) $\geq$ 0.7 at time of maximum extent
Terminate	Size definition A and B no longer satisfied

McAnelly and Cotton (1986) examined the meso-β characteristics of 12 MCC cases over the central United States from 3-10 August 1977. They classified the MCCs into "western" versus "eastern" MCCs. MCCs with origins along the eastern slopes of the Rockies and High Plains were named "western" MCCs. On the other hand, the MCCs with

origins further east over the more level and lower terrain of Missouri and Iowa were called "eastern" MCCs. The MCCs in the sample had a tendency to occur in the vicinity of, and track along, a quasi-stationary front. McAnelly and Cotton further categorized the MCCs according to size. The *smaller* (*larger*) MCCs had an average area (enclosed by the -53 ^{o}C isotherm) less than 120,000 km^2 (greater than 270,000 km^2). There were three MCCs in each of the four subcategories. The *larger* MCCs tended to have a longer lifetime than *smaller* MCCs, and the *western* MCCs had a longer lifetime than the *eastern* MCCs. The thunderstorms in the MCCs were organized into meso-β-scale convective clusters or bands. The *larger* MCCs had multiple meso-β clusters/bands throughout their lifecycle, while the *smaller* MCCs were dominated by a single meso-β component. The *larger western* MCCs developed on the High Plains from the growth, interaction, and merger of several meso-β convective features. The *larger eastern* MCCs, generated in Iowa and Missouri, involved fewer discrete meso-β components in their formation, with a tendency to develop upscale from one or two vigorous meso-β convective clusters. The meso-β clusters in the *larger western* MCCs were more chaotic and random.

In a followup to their earlier work, McAnelly and Cotton (1989) found that i) the small, less organized systems were "drier" than the similar sized but better organized MCCs; ii) large systems were "rainier" than smaller ones; iii) large eastern systems were "rainier" than large western MCCs; and iv) the eastern systems, both large and small, had a more coherent and intense core of heavy precipitation throughout its lifecycle than the western systems, presumably due to a more steady-state, less chaotic evolution of the convective substructure.

Cotton et al. (1989) found that the area enclosed by the -32 ^{o}C isotherm of a *mature* mid-latitude MCC to be 322 km or slightly larger than the Rossby radius of deformation

λ_R. The Rossby radius of deformation is defined as:

$$\lambda_R = \frac{NH}{(\xi + f)^{1/2}(2VR^{-1} + f)^{1/2}}, \tag{2.2}$$

where N is the Brunt-Vaisala frequency, H the scale height of the circulation, ξ the vertical component of the relative vorticity, f the Coriolis parameter, and V the tangential component of the wind at the radius of curvature R. Quoting Cotton et al. (1989), hence a mature MCC "represents an inertially stable mesoscale convective system which is nearly geostrophically balanced and whose horizontal scale is comparable to or greater than λ_R." The difference between a tropical MCC (tropical cloud cluster) and a mid-latitude MCC is that due a smaller Coriolis parameter in the tropics, λ_R is larger, hence given the same geometric dimensions, tropical cloud clusters are not as balanced.

2.3 Motivation and Hypotheses

As mentioned previously in this chapter, past modeling studies have demonstrated the sensitivity of convection to soil moisture distribution, but many of them were initialized with idealized atmospheric conditions. Also, with the exception of Ashby et al. (2001), Chen et al. (2001b), and Nachamkin and Cotton (2000), few studies have examined the sensitivity of real-data convective storm simulations to initial soil moisture on the cloud-resolving scale (i.e., with a grid spacing of 4 km or less, see Weisman et al. 1997). Finally, even fewer studies have investigated the sensitivity of initial soil moisture in cloud-resolving simulations of MCSs.

When the model grid spacing is too coarse, convective parameterization is required to account for the subgrid scale convective processes. The treatment of convective parameterizations is dependent on the grid spacing, and closure relies on the statistical correlation between subgrid scale and grid scale processes (Kain and Fritsch 1990). Thus, no convective

parameterization is perfect and there are always uncertainties involved. Cloud-resolving simulations, using no convective parameterization, avoid many of the problems in simulations with coarse resolutions where convective parameterization is required. Currently, many academic institutions, e.g., at Colorado State University, are already running their realtime forecast models at cloud-resolving scales and with the affordability of computing resources, seasonal simulations with regional models can be nested down to the cloud-resolving scale. Thus, testing the impact of soil moisture initialization in cloud-resolving simulations of MCSs would have applications in forecasting and seasonal prediction in areas where MCSs are prevalent. Besides forecasting and seasonal prediction, understanding the impact of soil moisture on convection and MCSs has applications in agriculture and water resource management.

The focus of this research is to test the following hypotheses:

- Mesoscale circulations generated by soil moisture anomalies can be important in initiating and organizing convection (Pielke 2001).
- The PIMS generated by a larger soil moisture anomaly (on the order of 100 km in size) should be weakly dependent on the internal fine-scale features within the soil moisture anomaly (Entekhabi et al. 1996).
- Although smaller soil moisture anomalies (20-40 km in size) generate weaker mesoscale circulations, their impact on convective precipitation may not be entirely negligible (Xian and Pielke 1991; Chen and Avissar 1994b).
- Extrapolating the 2D study by (Emori 1998), convection should be suppressed or delayed over wetter soil, even though wetter soil has a higher convective available potential energy (CAPE).

To test the above hypotheses, we simulated two typical summer MCS cases in the central United States using real data initialization. Although MCSs develop "upscale" from ordinary convective cells (McAnelly et al. 1994), synoptic and mesoscale features such as frontal boundaries, dry lines, upper-level and low-level jets often provide a favorable environment for mid-latitude MCSs to develop (Cotton and Anthes 1989). Thus, using real data initialization allows convection to develop realistically and avoids the use of "warm bubbles" to trigger convection as in many idealized simulations. We examined the sensitivity of the model to soil moisture initialization from a high resolution dataset during the genesis phase of the MCS. We focussed on the genesis phase because as mentioned in the previous section, a mature MCS (especially a MCC) is a more inertially stable system. Thus, it is anticipated that the surface fluxes and PIMSs would be more (less) influential in the MCS's incipient (mature) stage.

We varied i) the resolution of the soil moisture initialization (SMI) by applying the Barnes (1964) objective analysis as a smoothing operator, ii) the amplitude of the SMI to evaluate the strength of the PIMS generated by the wet soil moisture anomalies, and iii) the location of a soil moisture anomaly to test whether a wet soil moisture anomaly can suppress convection. Understanding the importance of the resolution of the soil moisture initialization needed to properly simulate convection is an important issue because we can optimize our resources to obtain the minimum resolution of soil moisture data to economize cost. In addition, we performed experiments with homogeneous SMI to contrast with experiments with heterogeneous SMI. We wish to emphasize that we were not trying to replicate the event to 100% accuracy, but only to study sensitivity of the cloud-resolving MCS simulation to the SMI. By running real-data simulations, we can see how a model with realistic initial atmospheric conditions respond to different SMI, and how the PIMSs generated by the soil moisture anomalies influence the development of the MCS.

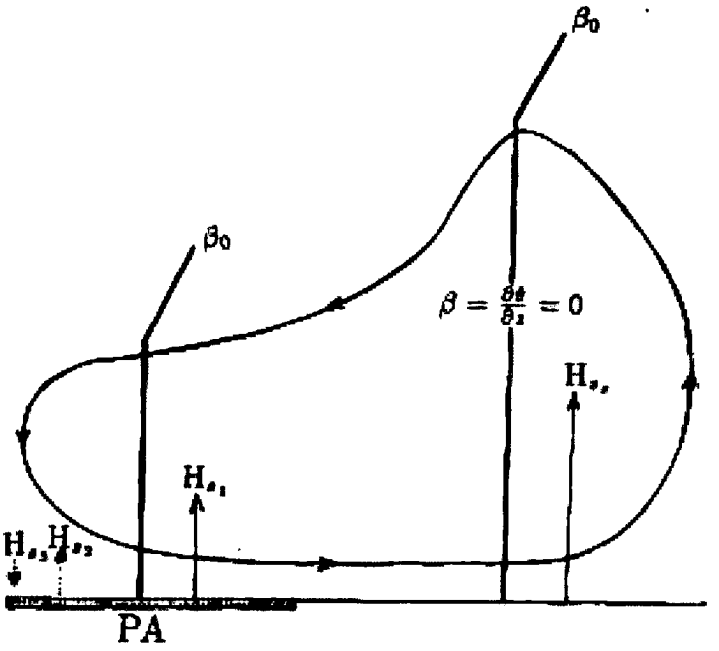

Figure 2.1 A typical PIMS vertical cross section over land. *PA* represents an area with reduced surface sensible heat flux (positive H_{s1}, H_{s2}) compared to surrounding (H_{ss}). In some cases, the surface sensible heat flux of *PA* might even be negative (H_{s3}). Over *PA*, a suppressed convective boundary layer or occasionally even a stable boundary layer, occurs over *PA* as compared to surroundings. Taken from Segal and Arritt (1992).

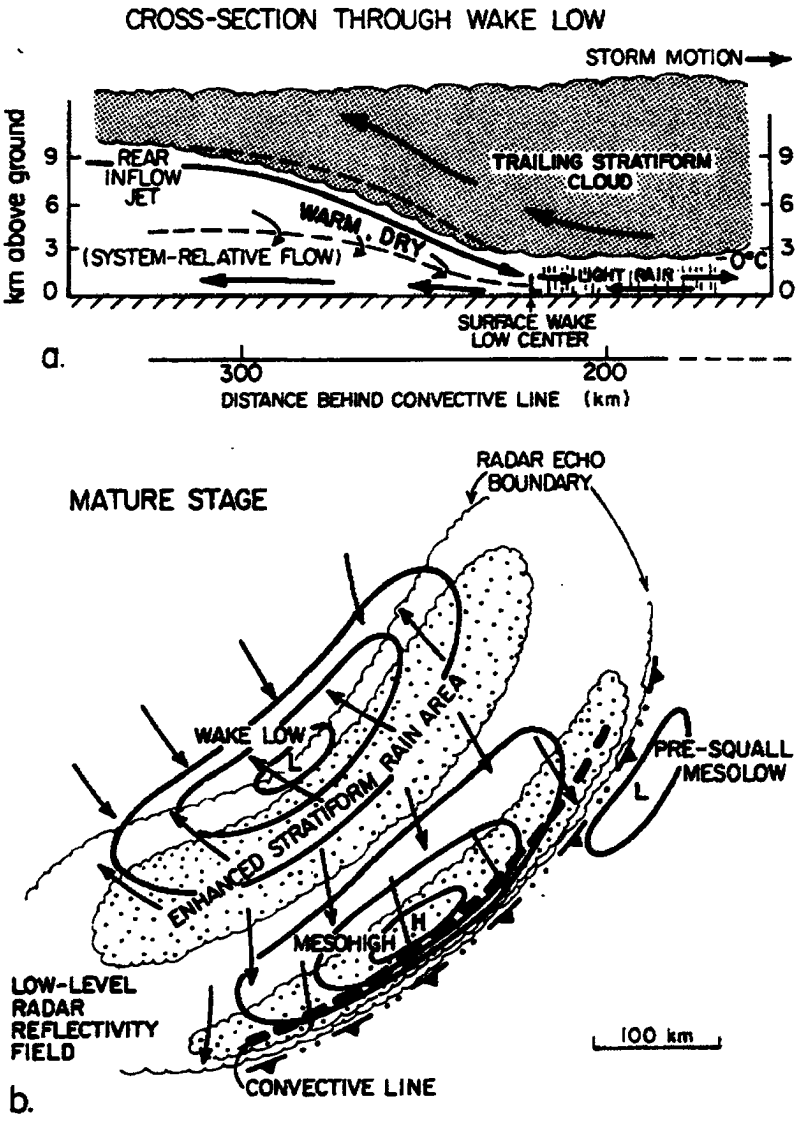

Figure 2.2 a) Schematic cross-section through wake low; b) surface pressure and wind and precipitation of a mature squall line; Dashed line in (a) denotes zero relative wind. Arrows indicate streamlines, not trajectories. Taken from Johnson and Hamilton (1988).

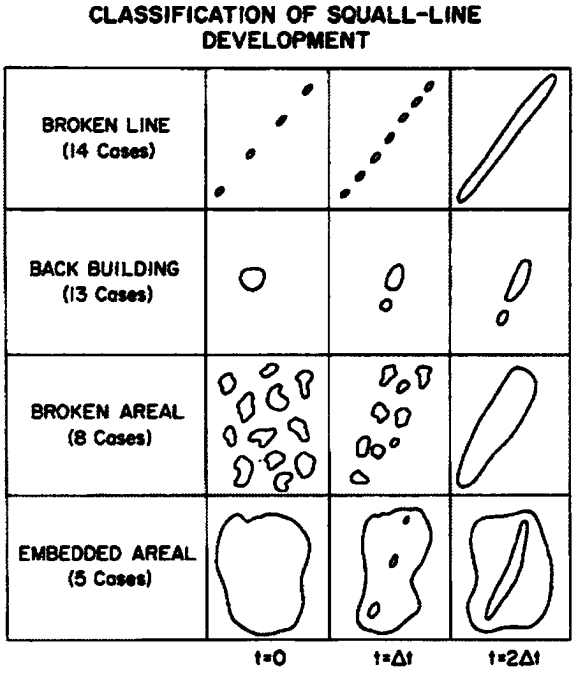

Figure 2.3 Classification of squall line development. Taken from Bluestein and Jain (1985).

Chapter 3

NUMERICAL MODEL AND METHODOLOGY

3.1 Numerical Model

In this study, we used the Colorado State University Regional Atmospheric Modeling System (RAMS) Version 4.29 (Tripoli and Cotton 1982; Pielke et al. 1992; Cotton et al. 2002). RAMS is a versatile modeling system, capable of simulating atmospheric flows from the hemispheric scale down to the large-eddy scale. As a research model, RAMS has been used to simulate a variety of cloud systems, e.g., supercells (Grasso 2000a; Finley et al. 2001), tornadoes (Grasso and Cotton 1995), mesoscale convective systems (Olsson and Cotton 1997; Bernardet and Cotton 1998; Nachamkin and Cotton 2000), boundary layer clouds (Golaz et al. 2001), and cirrus clouds (Wu et al. 2000; Cheng et al. 2001). Also, RAMS has been used as a regional climate model (e.g., Copeland et al. 1996; Pielke et al. 1997; Stohlgren et al. 1998; Greene et al. 1999; Pielke et al. 1999a; Eastman et al. 2001a,b; Liston and Pielke 2001; Lu et al. 2001), In additon, RAMS is currently being used in operational weather forecasting at i) Colorado State University, ii) NOAA Air Resources Laboratory Transport Modeling and Assessment Group and iii) Laboratorio per la Meteorologia e la Modellistica Ambientale (Italy).

Some key features of the model include: i) the interactive Land Ecosystem-Atmosphere Feedback model (LEAF-2, Walko et al. 2000), ii) a two-moment bulk microphysics package (Harrington et al. 1995; Meyers et al. 1997), iii) a two-stream radiative transfer model that is coupled to the microphysics package (Harrington 1997; Harrington et al. 1999). No convective parameterization was used at all.

LEAF-2 prognoses the temperature and water content of soil, snowcover (non-existent for this study), vegetation and canopy air and also accounts for the turbulent and radiative fluxes i) amongst the above mentioned components and ii) between the atmosphere and the above mentioned components. In addition, LEAF-2 contains a hydrological model that accounts for the surface and subsurface downslope lateral transport of groundwater. An additional feature of LEAF-2 allows the surface grid area to be divided into multiple subgrid area or "patches" of distinct land types with their own surface characteristics. Each patch interacts with the overlying atmosphere with a weight proportional to its fractional area. We used *four* land patches in this study. The land surface characteristics for the *four* patches in each grid surface area are selected from the four most dominant land types.

The two-moment microphysics package prognoses the number concentrations and mixing ratios of rain, pristine ice, aggregates, snow, graupel and hail. The cloud water mixing ratio is prognosed while the cloud water number concentration is specified. Vapor mixing ratio is diagnosed. In addition, through the coupling with the two-moment cloud microphysics, the two-stream radiation model accounts for the habit (the non-sphericity) of the ice hydrometeors in the radiative transfer equations (Harrington 1997; Harrington et al. 1999). A summary of the model physics used in this study is given in Table 3.1.

Table 3.1: Model options used in RAMS (with parts taken from Cotton et al. 2002).

Basic equations	• Non-hydrostatic time-split compressible.
Vertical coordinate	• Terrain-following σ_z coordinate (Tripoli and Cotton 1982).
Map projection	• Oblique stereographic coordinate.
Grid structure	• Arakawa C-grid (Arakawa and Lamb 1977). • Telescopically nested grids.
Time differencing	• Hybrid combination of leapfrog and forward-in-time (Tripoli and Cotton 1982).
Turbulence closure	• Grids 1 and 2: Mellor-Yamada level 2.5 scheme with ensemble averaged TKE (Mellor and Yamada 1982). • Grid 3: Smagorinsky (1963) deformation-K closure scheme with stability modifications made by Lilly (1962) and Hill (1974).
Cloud microphysics	• Level 4- Two-moment bulk scheme (Meyers et al. 1997).
Convective parameterization	• None.
Radiation	• Two-stream radiation package that interacts with the bulk microphysics (Harrington 1997; Harrington et al. 1999).
Land surface model	• Soil/vegetation parameterization (LEAF2, Walko et al. 2000).
Upper boundary condition	• Rigid lid.
Lateral boundary condition	• Klemp and Wilhelmson (1978) radiative boundary condition.

3.2 Soil Moisture

Soil moisture for grid 3 was inferred from the GCIP[1] precipitation archive by using the Antecedent Precipitation Index (API, Chang and Wetzel 1991). The API on the n^{th} day is given by:

$$API_n = R_n + \kappa(API)_{n-1}, \tag{3.1}$$

where the API value on the n^{th} day depends on the rainfall accumulation on the n^{th} day (R_n), depletion coefficient (κ) and the API value on the $(n-1)^{th}$ day. The depletion coefficient is less than unity and has a time dependence to account for the seasonality:

$$\kappa = 1 - 0.04\left\{sin\left\{2\pi\frac{(t-\tau_1-\tau_2)}{\tau_0}\right\}+1\right\}, \tag{3.2}$$

where t is the time in Julian days, τ_1 is 15 days, τ_2 is 91.25 days, and τ_0 is 365 days. The above expression came from T. J. Lee (a former student of Prof. Roger Pielke at Colorado State University) and the justification of the sinusoidal functional form of κ can be found in Choudhury and Blanchard (1983). To compute the fractional saturation in volumetric soil moisture (w_{frac}), we use the following expression:

$$w_{frac} = \frac{API_n}{API_{max}}, \tag{3.3}$$

where API_{max} is the maximum API value possible taken to be 40 mm.

The GCIP precipitation dataset has a grid spacing of 4 km and covers a large portion of the CONUS. We interpolated the soil moisture to grid 3 by using a bicubic spline interpolation (Vetterling et al. 1992). The minimum volumetric soil moisture was set to be 0.1 $m^3\ m^{-3}$, a typical value in the Oklahoma Mesonet soil moisture data. In addition, we assumed the soil moisture to be constant with depth.

[1]GCIP is the acronym for GEWEX Continental-Scale International Project and GEWEX stands for Global Energy and Water Cycle Experiment. A description of the aforementioned field projects can be accessed at the following website: http://www.joss.ucar.edu.

Note that we did not use the API method to initialize soil moisture on grid 1 because of the limited area of the GCIP precipitation data. Instead, we used the Eta Data Assimilation System (EDAS) soil moisture (40 km grid spacing) archived in the GCIP database to initialize grid 1. In addition, we also used the EDAS soil moisture to initialize grid 2 because we did not want grid 2 soil moisture to have a higher resolution than that of grid 3 in some of the sensitivity experiments where the soil moisture initialization was smoothed. Furthermore, we chose to have the soil moisture of grid 2 to come from the same source as grid 1. We wanted only to vary the soil moisture of the cloud-resolving grid (grid 3) while keeping everything else the same. The EDAS soil moisture (since 03 June 1998) was continuously cycled without soil moisture nudging (e.g., to some climatology). In addition, the EDAS soil moisture was the sole product of model physics and internal Eta Data Assimilation System (EDAS) surface forcing (e.g. precipitation and surface radiation). More information on the EDAS can be obtained at:

http://www.emc.ncep.noaa.gov/mmb/research/FAQ-eta.html#ETA11.

Of note, we used the Rapid Update Cycle (RUC) soil moisture (40 km grid spacing) on grids 1 and 2 and found no significant difference in the results of grid 3. In addition, we have used homogeneous soil moisture initialization on grids 1 and 2 (values obtained by horizontally averaging the soil moisture of grids 1 and 2 originally initialized by EDAS soil moisture) and found no significant impact on grid 3. Thus, we are confident that using different soil moisture datasets in different grids did not have significant impact on the cloud-resolving grid containing the MCS genesis domain.

3.3 Normalized Difference Vegetation Index

We used a semi-monthly composite of the normalized difference vegetation index (NDVI) at 1-km grid spacing, provided by the Earth Resources Observation Systems (EROS) Data

Center, to compute the leaf area index (LAI) for LEAF-2. The NDVI is defined as (Carlson and Ripley 1997):

$$NDVI = \frac{(a_{nir} - a_{vis})}{(a_{nir} + a_{vis})}, \tag{3.4}$$

where a_{nir} and a_{vis} are the surface reflectance averaged over the visible and near infrared parts of the spectrum, respectively. The NDVI varies between -1 and 1. Healthy vegetation has a high albedo in the near infrared region, thus a positive NDVI indicates a state of healthy vegetation. We used a variation of Chang and Wetzel (1991) formula for computing the "green" vegetation fractional area (v_{frac}):

$$v_{frac} = \frac{(NDVI - NDVI_{min})}{(NDVI_{max} - NDVI_{min})}, \tag{3.5}$$

where $NDVI_{min}$ and $NDVI_{max}$ correspond to the minimum and maximum NDVI, respectively. We chose the minimum and maximum NDVI from a ten-year record (1991-2000) for each pixel.

Next, we performed a weighted areal average of the "green" vegetation fraction that corresponded to the area occupied by the RAMS grid element. Using a similar formula as in Sellers et al. (1994), the LAI for the i^{th} patch within the RAMS grid area is:

$$LAI_i = (LAI_{max,i})(v_{frac}), \tag{3.6}$$

where $LAI_{max,i}$ corresponds to the maximum LAI of the particular biome[2] matching patch i. Values of maximum LAI are taken from LEAF-2 and are given in Table 3.2.

Figure 3.1 compares the default LAI from RAMS on 26 July, 1998 and the NDVI-derived LAI corresponding to the latter half of the month of July in 1998. Each pixel in the figure occupies an area of 2.5 km by 2.5 km, and the displayed domain corresponded to the cloud-resolving grid of the first MCS case in Chapter 4. Note that that the default

[2]The vegetation biome class dataset in RAMS has a grid spacing of 30 s.

Table 3.2: Maximum LAI of various biomes in RAMS.

Biome	Max. LAI
crop/mixed farming	6.0
short grass	2.0
evergreen needleleaf tree	6.0
deciduous needleleaf tree	6.0
deciduous broadleaf tree	6.0
evergreen broadleaf tree	6.0
tall grass	3.0
desert	0.0
tundra	3.0
irrigated crop	3.0
semi-desert	4.0
bog or marsh	3.0
evergreen shrub	5.0
deciduous shrub	5.0
mixed woodland	6.0

LAI is rather homogeneous with a value of 6 (a bit too high for the region) throughout most of the domain, while the NDVI-derived LAI, being more heterogeneous, varies from 1 to 5, with an average value of about 3. Thus, using the NDVI data allows for more spatial variability and realism in defining the LAI. Similar results hold for an August 1999 case. Figure 3.2a shows the default LAI from RAMS on 02 August, 1999, and Fig. 3.2b shows the NDVI-derived LAI corresponding to the first half of the month of August in 1999. Again, each pixel in the figure occupies an area of 2.5 km by 2.5 km, and the displayed domain corresponded to the cloud-resolving grid of the second MCS case in Chapter 5. The default LAI was again too high- a value 5-6 in most of the domain, but the NDVI-derived LAI was more realistic (an average LAI of 3.7) and more heterogeneous.

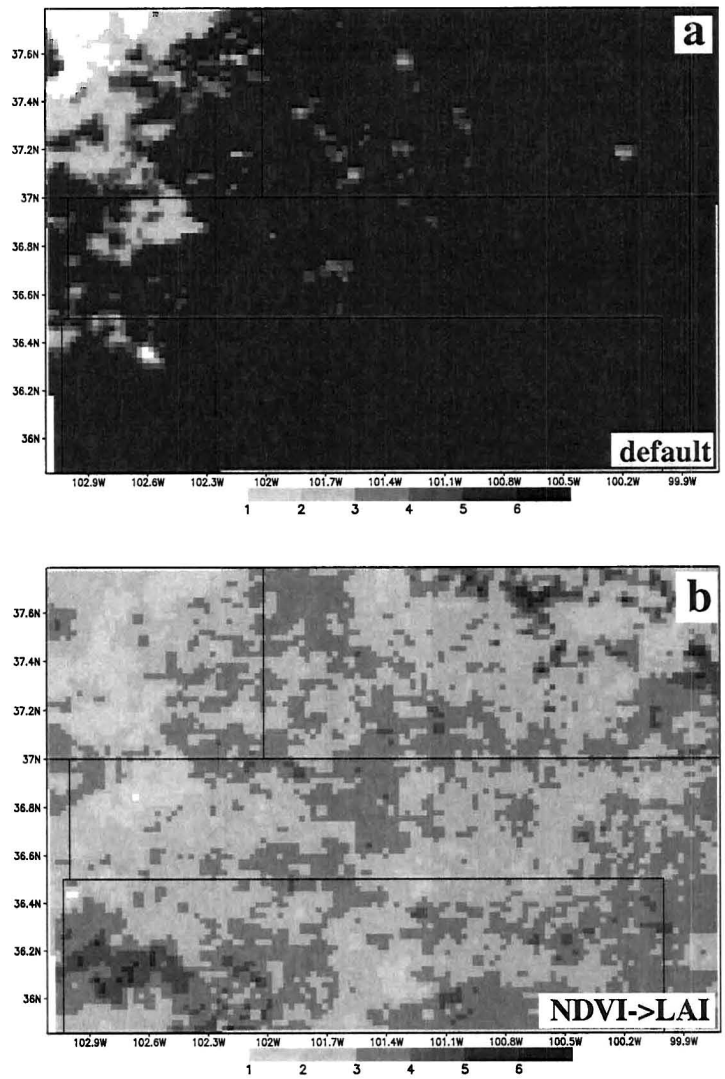

Figure 3.1 a) Default leaf area index in RAMS on 26 July, 1998; b) NDVI-derived leaf area for the latter half of the month of July in 1998.

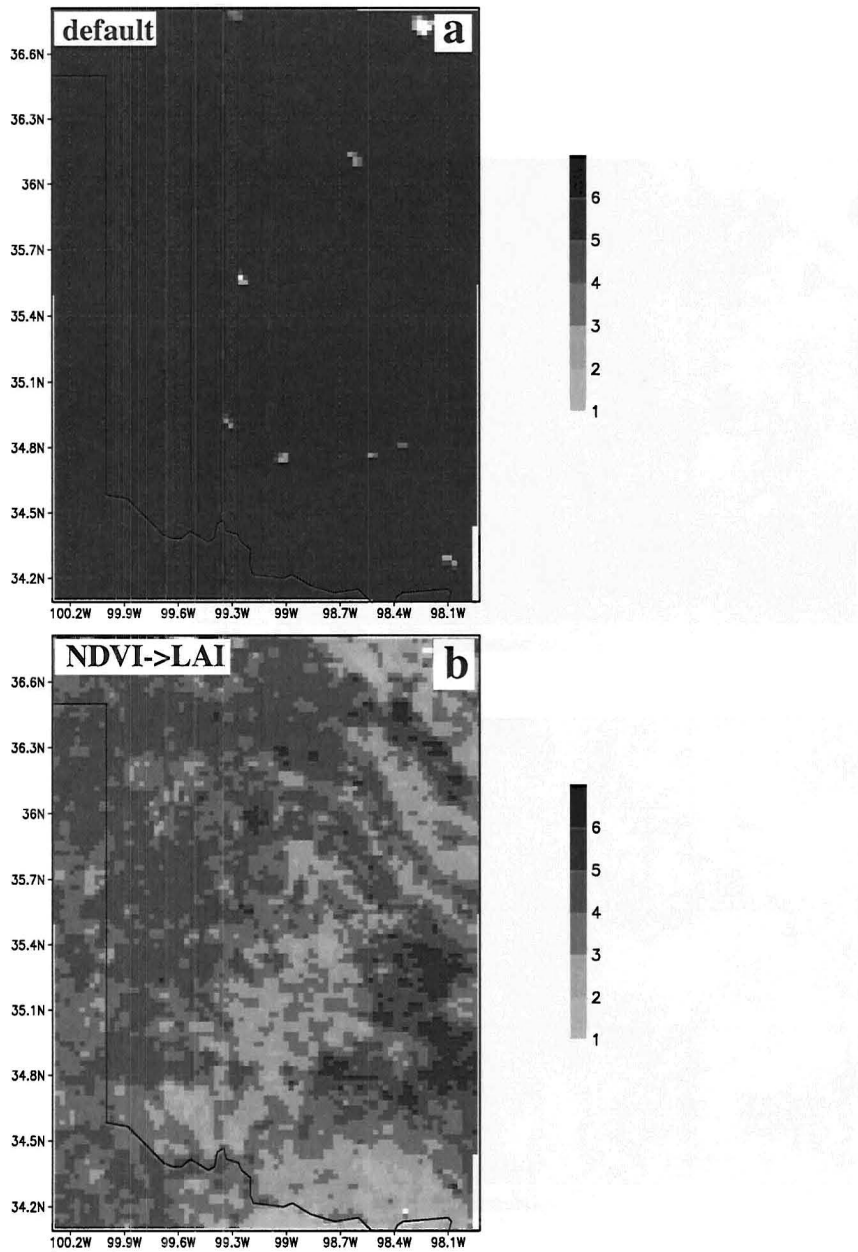

Figure 3.2 a) Default leaf area index in RAMS on 02 August, 1999; b) NDVI-derived leaf area index in RAMS for the first half of the month of August in 1999.

Chapter 4

JULY 26, 1998 MCS CASE

The first case chosen for this study was a quasi-stationary MCS which initiated in the Texas/Oklahoma border near a quasi-stationary front around 2200 UTC 26 July (26/2200 hereafter) and dissipated approximately at 27/0700 UTC 27 July 1998 (27/0700). This MCS formed from two smaller convective systems whose cloud shields merged, and eventually developed into a quasi-circular MCS (although too small to be a MCC). Convection beneath the cloud shield consisted a leading convective line with trailing stratiform precipitation. We named this MCS "Case 980726" where we tested the sensitivity of the simulated MCS to soil moisture initialization.

4.1 Case 980726

Figure 4.1a,b shows the infrared (IR) satellite imagery and radar reflectivity, respectively, at 26/1945. A small area of deep convection has initiated in the western Texas panhandle (A_1) when the outflow of the convection in New Mexico to its west encountered the quasi-stationary front in the Texas/Oklahoma panhandle. A shallow line of clouds (A_2), in a southwest-northeast orientation, developed along a surface trough that spanned across Oklahoma and Texas (shown later).

By 26/2145 (Fig. 4.1c,d), A_1 has developed into an area of deep convection in the western Texas/Oklahoma panhandle region. Meanwhile the convective line of A_2, advancing northward, intensified as it encountered the quasi-stationary front in the Texas panhandle region. By 27/0053 (Fig. 4.1e,f), A_1 and A_2 have merged into a common cloud shield and the MCS has fully developed and covered the Texas/Oklahoma panhandle region and small parts of Colorado, New Mexico and Kansas. The convective organization of the squall line beneath the cloud shield was a leading convective line with trailing stratiform preciptiation.

4.2 Model Setup/Initial Conditions

Figure 4.2 shows the nested grid setup for Case 980726. We used two levels of nesting, with horizontal grid spacing of 50, 12.5 and 2.5 km in grid 1, 2, and 3, respectively, and 36 vertical σ_z-levels in each grid (see Tables 4.1 and 4.2). σ_z is a terrain-following coordinate defined as $\sigma_z = H[(z - z_s)/(H - z_s)]$, where H is the height of the model top, z_s is the terrain height, z is the height of the model grid point above sea-level (Tripoli and Cotton 1982). The grid setup and model physics were very similar those of the current RAMS realtime forecast model in the Cotton research group:

http://rams.atmos.colostate.edu.

Grid 3 (the cloud resolving grid) was centered over the Texas/Oklahoma panhandle region to capture the MCS during its genesis phase. *We stopped the simulation at 15 model hours after the system moved out of grid 3.* We did not use a moving grid to follow the MCS into grid 2 since the moving grid would not retain some of the grid 3 soil moisture. Currently, soil moisture is initialized as horizontally homogeneous in the realtime RAMS forecast model. So, this study will have practical implications in determining to what extent heterogeneous soil moisture is important in simulating (or forecasting) MCSs. We

used the National Centers for Environmental Prediciton (NCEP) global analysis to initialize the model atmospheric fields as well as to provide nudging boundary conditions for grid 1's five outermost grid points. The model was initialized on 1200 UTC, 26 July 1998 (26/1200).

Table 4.1: Horizontal grid setup for Case 980726.

number of grids	3
number of x points	60, 78, 122
number of y points	48, 78, 87
number of σ_z points	36, 36, 36
horizontal grid spacing (km)	50, 12.5, 2.5

Table 4.2: Vertical levels (σ_z) used in the simulations for Case 980726 (in m).

0.0	150.0	300.0	450.0	600.0	750.0
915.0	1096.5	1296.2	1515.8	1757.3	2023.1
2315.4	2636.9	2990.6	3379.7	3807.6	4278.4
4796.2	5365.9	5992.5	6681.7	7439.9	8273.9
9191.3	10191.3	11191.3	12191.3	13191.3	14191.3
15191.3	16191.3	17191.3	18191.3	19191.3	20191.3

Fig. 4.3 shows the model initial conditions. At 26/1200, a surface trough extended from Hudson Bay into North Dakota and South Dakota (Fig. 4.3a). Also, a quasi-stationary front stretched from the Texas/Oklahoma panhandle region, through the Kansas/Oklahoma border, into the southeastern states. South of the quasi-stationary front in the Texas/Oklahoma panhandle, the winds (at the lowest σ_z-level) shifted from northerly to westerly due to the influence of the subtropical high over the Gulf of Mexico. Thus, there was low-level convergence along the quasi-stationary front near the MCS genesis region. A surface trough extended from northwestern Oklahoma into the South Plains of Texas, and a sea-level high was located over central Colorado.

The 850-hPa equivalent potential temperature, θ_e, reveals a wide tongue of high-θ_e air, in an northwest/southeast orientation that stretched from the southeastern states all the way to southern Wyoming, covering most of Colorado and parts of the Texas/Oklahoma panhandle at 26/1200 (Fig. 4.3b). At this level, weak winds from the north also brought in high-θ_e air to the genesis region. However, the influence of the subtropical high over the Gulf of Mexico did not extend into the Texas/Oklahoma panhandle region.

Figure 4.3c shows a weak 400-hPa potential vorticity (PV, see Hoskins et al. 1985) [1] band to the north of the Texas/Oklahoma panhandle that was associated with a dissipating MCS at the model initial time. Winds at this level were weak as well, and there was no upper-level feature upstream of the genesis region at this time. A sounding (Fig. 4.4) closest to the genesis region (Amarillo, Texas, Fig. 4.3a) shows weak winds throughout the entire atmospheric column, and little directional or speed shear in the wind from the surface to 500-hPa. From the surface to 400-hPa, the wind was southwesterly, then switched to southerly between 400-hPa and 300-hPa, and the wind was easterly above 300-hPa. The sounding only had a value of 670 J kg^{-1} in convective available potential energy (CAPE). There was a shallow inversion layer at the surface (about 25-hPa deep). At this time, the atmosphere was relatively dry (moist) from the surface to 700-hPa (from 700-hPa to 475-hPa).

4.2.1 Soil moisture and sensitivity experiments

To alter the resolution of the soil moisture, we applied the Barnes objective analysis (Barnes 1964) to smooth the soil moisture with a response amplitude (A) of 0.5 and a cutoff wavelength (λ_{cut}) of 20 (exp. API20), 40 (exp. API40) and 80 (exp. API80) km for various sensitivity studies. To alter the amplitude of the soil moisture field, we reduced the soil

[1] PV is defined as the dot product between the absolute vorticity vector and the gradient of the potential temperature divided by the density of the fluid.

moisture in exp. API by a factor of 2 (exp. APIHALF). A soil moisture anomaly in the eastern Texas panhandle in exp. API was displaced southwestward to suppress convection (exp. APIMOVES2). An experiment (HOM31) was also performed with homogeneous soil moisture initialization (at 31% saturation) by horizontally averaging the soil moisture in exp. API. Another homogeneous soil moisture experiment, at 50% saturation, was also performed (exp. HOM50). A summary of the experiments is listed in Table 4.3.

Table 4.3: List of numerical experiments.

Exp.	Description
API	- soil moisture in grid 3 derived from API method.
API20	- grid 3 soil moisture in exp. API smoothed by Barnes objective analysis with a response amplitude of 0.5 and a cutoff wavelength of 20 km.
API40	- same as exp. API20 but with a cutoff wavelength of 40 km.
API80	- same as exp. API20 but with a cutoff wavelength of 80 km.
APIHALF	- grid 3 soil moisture in exp. API divided by two.
APIMOVES2	- soil moisture anomaly, S_2, in grid 3 from exp. API displaced southwestward.
HOM31	- homogeneous soil moisture in grid 3 at 31% saturation, a value obtained by horizontally averaging the grid 3 soil moisture in exp. API.
HOM50	- homogeneous soil moisture in grid 3 at 50% saturation.

The initial soil moisture fields for grid 3 for the various sensitivity experiments are displayed in Fig. 4.5. There were two large soil moisture anomalies in grid 3, one in the northwest corner (S_1) and one near the center of the domain (S_2). Because of the proximity of some soil moisture anomalies to one another, we will refer to some of them as a single unit for ease of reference. As λ_{cut} of the Barnes objective analysis was increased, finer scale features were lost in S_1 and S_2 and the horizontal extent of the smaller soil moisture anomalies (S_3 and S_4) decreased as well. In fact, when λ_{cut} reached 80 km, S_3 completely disappeared and very little of S_4 remained. For larger soil moisture anomalies, (i.e., S_1 and S_2), they still retained their identities despite the smoothing. In all the experiments, 11 soil levels were used (Table 4.2.1).

Table 4.4: Soil levels (below ground) used in the simulations (in m).

z_{11}	0.02
z_{10}	0.12
z_9	0.22
z_8	0.32
z_7	0.42
z_6	0.52
z_5	0.62
z_4	0.72
z_3	0.82
z_2	0.92
z_1	1.02

4.3 Model Results

4.3.1 Grid 1

We compare the grid 1 fields with those in NCEP analysis in order to examine how well RAMS reproduced the large-scale flow. First, we look at the fields from NCEP analysis at 27/0000 (Fig. 4.6a). By this time, the western end of the quasi-stationary front has moved southeastward, away from the Texas panhandle/Oklahoma panhandle region. The outflow boundary (identified by the National Weather Service and labeled in Fig. 4.6a) resulting from convection in New Mexico and the MCS in the Texas/Oklahoma panhandle distorted the quasi-stationary front in the Texas/Oklahoma panhandle. There was a region of surface convergence in the Texas/Oklahoma panhandle region due to the deceleration of the wind from the north. Next, we examine the grid 1 results from exp. API (Fig. 4.6b) at 27/0000. Other experiments produced similar results for grid 1 and will not be shown for the sake of economizing space. The sea-level pressure in exp. API compares reasonably well with that of the NCEP analysis, except that the surface low over Oklahoma was more to the west in exp. API and 2 hPa lower.

In the NCEP analysis, the 850-hPa high-θ_e tongue that covered the Texas/Oklahoma

panhandle region has increased by 4 K at this time (Fig. 4.6c). The 850-hPa θ_e in exp. API compared reasonably well with NCEP analysis albeit with a few discrepancies (Fig. 4.6d). The simulated θ_e maxima did not extend as far into Colorado. In exp. API, the 850-hPa southwesterlies over eastern Oklahoma, associated with the subtropical high over the Gulf of Mexico, was a bit stronger than those in the NCEP analysis.

From the NCEP analysis, the 400-hPa PV map still shows the PV band associated with a dissipating MCS from the last 12 h. Also, diabatically generated PV from convection over New Mexico joined with the aforementioned PV band at the western end (Fig. 4.6e). As with 12 h earlier, the winds at 400-hPa were still weak. Exp. API produced a band of PV at 400-hPa as in NCEP analysis but with a much stronger local maximum over the western panhandle (due to diabatic heating) than in NCEP analysis (Fig. 4.6f). Nevertheless, RAMS reproduced the large-scale features fairly well at this time.

4.3.2 Grid 2

A comparison of exp. API grid 2 cloud top temperature (defined as the temperature of the total condensate mixing ratio > 0.1 g kg^{-1} at the highest elevation of the atmospheric column) shows convective activity in the Texas/Oklahoma panhandle at 26/2200 (Fig. 4.7a), but the shape of the cloud top was somewhat different than in the satellite imagery (Fig. 4.1c). In addition, the simulated convective activity was a bit too far north. Furthermore, we observed two distinct convective regions in the eastern and western panhandle that were not simulated in exp. API. However, by 27/0100 in exp. API, a quasi-circular cloud shield (Fig. 4.7b) similar to observations (Fig. 4.1e) developed over the Texas/Oklahoma panhandle region, extending into Kansas, but the observed cloud shield did not extend so far into Kansas. However, RAMS managed to produce a MCS in the area close to the observed MCS with a similar shape at the right time. Therefore, we can have some confidence in

the results produced by RAMS. Other sensitivity experiments (except for exp. HOM50) produced similar results, so again for the sake of brevity, they will not be shown.

4.3.3 Pre-genesis phase: grid 3

Figure 4.8a-f shows that the surface latent heat flux (SLHF) pattern corresponded quite well to the soil moisture anomalies in grid 3 (Fig. 4.5a-f) at 26/1600. Because the smoothing of the soil moisture led to a decrease in amplitude and gradient of the soil moisture, the peak latent heat flux in S_2 decreased with increasing λ_{cut}. Peak SLHF in S_2 was 455, 450, 430, 377 W m^{-2} for exp. API, API20, API40, API80, respectively. Due to the horizontal extent of S_1 and S_2, they were more robust features despite the smoothing. S_3, S_4 and the "horn" of S_2 were unable to retain much of their identities after λ_{cut} reached 40 km or greater. When the soil moisture was reduced by a factor of two, the areal coverage of large SLHF was reduced dramatically in exp. APIHALF. This has to do with the parameterization of transpiration in LEAF-2 which is largely controlled by the stomatal response function (SRF). When the SRF is unity (zero), the stomata is completely open (closed). The SRF is very sensitive to soil moisture, and the transition of SRF from zero to unity occurs over a small range of soil moisture values (Avissar and Pielke 1991; Golaz et al. 2001). Many grid points in exp. APIHALF fell below that transition point (slightly below 50% saturation), thus the low SLHF. As expected in exp. APIMOVES2, the maxima of surface latent heat flux (associated with S_2) has been displaced southwestward (Fig. 4.8f). SLHF from exp. HOM31 (Fig. 4.8g) had values of 100 W m^{-2} or less. The low value of surface latent heat flux in exp. HOM31 was again due to the low value of the soil moisture, falling below that transition point of the SRF. On the other hand, in exp. HOM50, the SLHF was much higher than that of exp. HOM31 (except for a small region in the southwest corner of the domain where low-level cloud shielded solar radiation at the surface; figure not shown), due to the SRF close to unity.

In exps. API, API20, API40, and API80, because the soil moisture anomalies contributed to enhanced moisture fluxes, the Bowen ratio (SSHF divided by SLHF) was generally less than 0.5 over the soil moisture anomalies (Fig. 4.9). In very wet (drier) soil areas, the Bowen ratio was less than 0.25 (greater than 2). The minimum in Bowen ratio in the southwest corner of the domain corresponded to low-level clouds shielding the model solar radiation (mentioned in the previous paragraph). Thus, in general, during clear sky conditions, the drier (wetter) soil tends to partition most of the solar energy into SSHF (SLHF). In exp. APIHALF, the signatures of the soil moisture anomalies were much smaller, thus the Bowen ratio was large in much of the domain. Again, it is not surprising to see that the low Bowen ratio associated with S_2 being displaced southwestward in exp. APIMOVES2. In exp. HOM31, most of the domain had high Bowen ratio due to the low evapotranspiration (except for the southwest corner). As expected, exp. HOM50 had very low values of Bowen ratio due to the low SSHF.

Figure 4.10 shows the dewpoint temperature at the lowest σ_z-level above ground at 26/1800. The influence of the soil moisture anomalies could be clearly seen, especially S_2 in the experiments with heterogeneous SMI, except for exp. APIHALF. In the heterogeneous SMI experiments (except exp. APIHALF), S_2 raised the dewpoint at this level by almost 2 ^{o}C as compared to exp. HOM31. The effect of S_1 was not as noticeable as S_2 due to the smaller size of S_1 and its proximity to the lateral boundaries, but S_1 did raise the dewpoint by about 1 ^{o}C. Smaller soil moisture anomalies such as S_3 and S_4 had less noticeable effects on the dewpoint at this level and their effects were even smaller when the smoothing of the soil moisture was increased. Exp. HOM50 had the highest dewpoint amongst all the experiments; the local maximum over Kansas was the result of high local SLHF (due to higher LAI).

To quantify the dynamical effect of the soil moisture anomalies at 26/1800, we took

the difference fields of the sea-level pressure, the horizontal wind vector and the vertical velocity at the lowest σ_z-level, using exp. HOM31 as a baseline (Fig. 4.11). *First, we discuss the results of exps. API, API20, API40, and API80.* The cooling effect of the soil moisture anomaly S_2 created a mesohigh on the order of 0.5 hPa at sea-level as well as a divergent flow perturbation (on the order of 4 m s^{-1}) at the lowest σ_z-level. Also, there was enhanced vertical motion (on the order of several centimeters per second) around the periphery of the soil moisture anomalies that resulted from convergence of the divergent wind perturbation with the flow from outside of the soil moisture anomalies. It is interesting to note that the divergent flow perturbation maximum (associated with S_2) increased slightly from 3.6 to 4.1 (4.4) m s^{-1} when the soil moisture was smoothed to 20 (40) km. This was due to the internal circulations generated by the fine-scale soil moisture features opposing the mesoscale circulation induced by the larger-scale soil moisture in S_2 as a whole. However, when the smoothing reached a cutoff wavelength of 80 km, the divergent flow perturbation maximum decreased to 4.1 m s^{-1}. Although the fine scales features have been eliminated at this point, the large-scale structure of the soil moisture has been smoothed too much, hence the PIMS has weakened. With regard to S_1, the associated mesohigh (on the order of 0.25 hPa) and the divergent flow perturbation were somewhat weaker and smaller in coverage than those of S_2, but the smoothing of the soil moisture expanded the coverage of the mesohigh associated with S_1. The effect of S_3 was weak, due to its small size and shielding from low-level cloud (not shown). S_3 almost disappeared when the smoothing reached a cutoff wavelength of 40 km. Although the mesohigh generated by S_4 was less than 0.25 hPa, it generated small regions of anomalous vertical motion (on the order of 2-4 cm s^{-1}). However, the influence of S_4 diminished (disappeared) when the smoothing reached a cutoff wavelength of 40 (80) km.

In exp. APIHALF (Fig. 4.11e), because of the reduced SLHF (in terms of area and magnitude), the mesohigh generated by S_2 was less than 0.25 hPa, and the divergent wind

perturbation associated with S_2 was less than 2 m s^{-1}. In addition, there was little enhanced vertical motion around the periphery of S_2. The effects of other soil moisture anomalies in exp. APIHALF were harder to discern. As expected, when S_2 was displaced in exp. APIMOVES2, the anomalous mesohigh associated with S_2 shifted southwestward. Because of the higher values of SLHF (thus a cooler surface) in exp. HOM50, the sea-level pressure was higher in exp. HOM50 throughout most of its domain when compared to exp. HOM31 (Fig. 4.11f,g).

To determine the depth of the mesohigh generated by S_2, we took a cross section of the horizontal temperature deviation through S_2 at 26/1800 (Fig. 4.12). To obtain the temperature deviation, we subtracted the temperature field from the average temperature at each constant height level. Since the experiments with heterogeneous SMI had similar results, we will only show results from exps. API and API80. The depth of the cold pool associated with the mesohigh generated by S_2 was about 1.5 km and the maximum temperature contrast with its surroundings was about 3.5 K. The edges of this cold pool served as a focusing mechanism for convection to develop because of the enhanced convergence along the periphery of S_2 (shown later).

4.3.4 Genesis phase: grid 3

We examine the convective activity in the cloud-resolving grid using the instantaneous precipitation rate. *With the exception of exps. APIMOVES2 and HOM50*, all the experiments showed very similar results at 26/1915 (Fig. 4.13). There were two weak precipitation areas (C_1 and C_2) in the western Oklahoma panhandle. C_1 and C_2 originally formed in the western Texas panhandle area at 26/1500 as very weak precipitation areas ($\sim$ 1 mm h^{-1}) and slowly moved northward. There was also an area of strong convection, C_3, in the middle of the Texas panhandle that also formed in response to a build up of CAPE and low-level

convergence along the quasi-stationary front. Compared to the satellite imagery at 26/1945 (Fig. 4.1a), the model placed the precipitation a bit too far north and east of the Texas panhandle at this time, but the timing of the model convection was reasonably accurate. C_2 was rather weak and would dissipate shortly after this time. Results in exp. HOM31 (Fig. 4.13g) were also similar to those experiments with heterogeneous SMI (except for exp. APIMOVES2). However, C_2 in exp. HOM31 was much smaller in coverage as compared to the experiments with heterogeneous SMI due to the absence of the PIMS contributed by S_2 in enhancing C_2. In exp. APIMOVES2, the cooling effect of S_2 suppressed the initiation of C_3 at this time. In a similar manner, convection was suppressed in exp. HOM50 at this time (Fig. 4.13h). Since the results in most of the experiments were very similiar, large-scale forcing must be primarily responsible for initiating convection. Next, we examine how the soil moisture heterogeneities affected the evolution of convection.

At 26/2145, convection was becoming more organized for most of the experiments. *First, we discuss the results in exps. API, API20, API40, and API80 which were qualitatively similar* (Fig. 4.14a-d). C_1 precipitated more heavily with the smoothing of the SMI due to the enhanced PIMS associated with S_1. C_3 and C_4 tended to develop along the periphery of S_2 because of the enhanced convergence there associated with the cold pool of S_2 (Fig. 4.14a-d). C_4 was generated 1-h earlier due to the remnant of the weak outflow boundary from C_2 (Fig. 4.13) interacting with the PIMS generated by the soil moisture anomaly S_2. The outflow of C_4 generated C_7 ahead of it except in exp. API40 in which C_7 emerged 30 min later. C_6 was created when the PIMSs generated by the northern and southern ends of S_4 collided. The outflow from C_3 also assisted in the initiation of C_6. As S_4 was smoothed, leading to a reduction of its associated PIMS, C_6 was also reduced in intensity.

Next, we discuss the results for the other experiments at 26/2145 (Fig. 4.14e-h). In exp. APIHALF, the cold pool associated with S_2 was weaker (therfore less convergence

along the periphery of S_2). Thus, C_3 and C_4 did not preferentially develop along the periphery of S_2 as in exps. API, API20, API40, and API80, but tracked more towards the interior of the Oklahoma panhandle region. C_6 did not form because the PIMS associated with S_4 was negligible. The results of exp. APIMOVES2 were qualitatively simiar to those of exp. API but C_3 did not appear. Although the new location of S_2 suppressed the development of C_3, C_4 was generated at the periphery of S_2 at 26/1945 (one hour earlier than in exp. API, not shown). C_6 in exp. APIMOVES2 was also weaker than that of exp. API due to the absence of the outflow boundary associated with C_3 interacting with the PIMS of S_4. In exp. HOM31, due to the lack of the cold pool generated by S_2, C_3 tended to track across the Oklahoma panhandle. C_6 was expectedly absent in exp. HOM31 due to the lack of soil moisture anomaly S_4. Convection was finally initiated in exp. HOM50 at this time, including the appearance of a multi-cellular system in the middle of the Texas/Oklahoma border. The delay in convection in exp. HOM50 was due to a cooler surface associated with a higher SLHF.

The domain-averaged shear in the lowest 6-km and the CAPE at 26/1800 in exp. API were 13.4 m s^{-1} and 1240 J kg^{-1}, respectively, an environment indicative of nonsevere squall line (Bluestein 1992). So, by 26/2300, in all the experiments (except exp. HOM50), the outflow boundaries of various cells have merged to produce a convective line with a southeast/northwest orientation, just north of the Oklahoma panhandle (Fig. 4.15). The convective lines in exps. API, API20, API40 and API80 were very similar to each other. In exp. APIHALF, because of the weaker cold pool generated by S_2, the convective cells did not preferentially develop along the periphery of S_2 but they tracked more towards the interior of the Oklahoma panhandle. So the convective line advanced farther into the eastern edge of the domain in exp. APIHALF. The convective line in exp. APIMOVES2 was a bit shorter compared to other experiments due to the absence of C_3 (Figs. 4.13,

4.14). Qualitatively, the convective line in exp. HOM31 was similar to other experiments. However, exp. HOM50 failed to develop a convective line, and convection was not well organized in exp. HOM50.

Figure 4.16a shows the sea-level pressure of exp. API at 26/2300. A presquall mesolow was ahead of the convective line and two regions of squall mesohigh were located behind the presquall mesolow. A wake low has not yet developed as the MCS has not yet reached maturity. A cross-section taken perpendicular to the convective line (through one of the convective cells, Fig. 4.16c) reveals conditions of potential instability in the lowest 3 km ahead and in the lowest 2 km behind the convective line. The MCS horizontal motion (estimated from the average of various cells to be 6.2 and 5.0 m s^{-1} in the x- and y-direction, respectively) has been subtracted from the horizontal winds in the cross section. The MCS-relative rear inflow had a maximum speed of 7 m s^{-1} and was confined between 3-5 km above sea-level (ASL). The low-θ_e tongue (340-K contour) behind the convective line sloped downward from the rear to near the leading updraft at 5 km ASL. The MCS-relative front-to-rear flow transported high-θ_e air at low-levels, ahead of the convective line, into the updraft where latent heating can occur, allowing the system to intensify. There was significant vertical wind shear ahead of the convective line (20 m s^{-1} in the lowest 2 km), favorable for sustained convective development as the wind shear interacted with the cold pool of the system (Weisman et al. 1988).

Although qualitatively similar to the results in exp. API, the sea-level pressure for exp. HOM31 at the same time shows a somewhat different pattern (Fig. 4.16b). There was a presquall meso-trough (not a closed low as in exp. API). Behind the meso-trough, there were two centers of squall mesohighs, similar to exp. API. To the rear of the squall mesohighs, there was a closed sea-level low, but it was a transient feature and not a persistent wake low. A cross section taken perpendicular to the convective line Fig. 4.16d) shows a

layer of potential instability in the lowest 3 km (2 km) ahead of (behind) the convective line, similar to exp. API. The MCS horizontal motion was estimated to be 6.1 and 6.6 m s^{-1} in the x- and y-direction, respectively and this velocity has been subtracted from the horizontal wind in the vertical cross section. The MCS-relative rear inflow was confined mainly in the 3-6 km layer ASL, with a maximum speed of 20 m s^{-1}, much higher than in exp. API. As in exp. API , the low-θ_e tongue behind the convective line sloped downward from the rear to the convective line descended to as low as 3 km ASL (versus 5 km ASL for exp. API). The vertical wind shear ahead of the convective line was somewhat lower than in exp. API (15 m s^{-1} in the lowest 2 km), thus there was a weaker interaction of the vertical wind shear with the cold pool. As a result, the high-θ_e air was not transported as high in the updraft. The 356-K contour in exp. API (HOM31) reached 9 (3) km ASL. The maximum vertical motion in exp. HOM31 was weaker than that of exp. API (9 vs. 16 m s^{-1}).

In the time series of grid 3 domain-averaged SLHF, the highest (lowest) SLHF was from exp. HOM50 (APIHALF) (Fig. 4.17a). This is not surprising since the SRF was almost unity (zero) for most of the domain in exp. HOM50 (APIHALF), allowing the most (the least) transpiration. All the other experiments fell somewhere between the two extremes. Exp. HOM31 had slightly lower SLHF than exps. API, API20, API40, API80 and APIMOVES2 between 26/1600 to 26/2100. In the SSHF time series (Fig. 4.17b), the results were completely opposite to the SLHF time series due to the influence of soil moisture in partitioning the SSHF and SLHF. The highest (lowest) sensible heat flux was from exp. APIHALF (HOM50), and the rest of the experiments again fell somewhere in between. Although exp. HOM50 had a colder surface temperature ($\approx$ 4 K, shown later) than exp. APIHALF due to a lower SSHF, it had a higher CAPE than any other experiment due to a compensation in increase in low-level humidity (Fig. 4.17c). On the other

hand, although exp. APIHALF had a warmer surface temperature than exp. HOM50, the lower SLHF (hence lower low-level humidity) resulted in a much lower value of CAPE. The other experiments fell somewhere in between the two extremes, but were more closer to exp. APIHALF. Examining a time series of a point in grid 1 very close to S_2 (Fig. 4.18), not surprisingly, the drier soil had the highest (lowest) temperature at the lowest σ_z-level, i.e., exps. APIHALF, APIMOVES2, HOM31 (exp. HOM50). The rest of the experiments fell somewhere between the two extremes, and the range of the extreme was about 4 K. The results here support Pielke (2001)'s contention that higher SLHF compensates for the lowering of the surface temperature in increasing the CAPE.

In the grid 3 domain-averaged precipitation rate time series (Fig. 4.19a), exp. HOM50 had the lowest precipitation rate amongst all the experiments, although it had the highest CAPE. Due to a higher SSHF in exps. APIHALF and HOM31 (therefore warmer surface temperature), the peak precipitation rate (hence peak convective activity) was reached 30 min sooner than exps. API, API20, API40, API80. Also, in general, exps. APIMOVES2 and HOM31 had lower precipitation rates than exps. API, API20, API40, API80. In terms of the grid 3 domain-averaged accumulated precipitation time series, not surprisingly, exp. HOM50 had the lowest accumulated precipitation due to delay in convection and precipitation being confined to limited areas of the domain. Exp. APIHALF had almost 1 mm higher accumulated precipitation than exps. API, API20, API40, API80, and HOM31 for about 30 min between 26/2300 and 26/2330. Due to the suppressed formation of C_3 in exp. APIMOVES2, the accumulated preciptation in exp. APIMOVES2 was lower than those in exps. API, API20, API40, and API80.

4.4 Discussion

In exp. HOM50 (with relatively wet soil), convection was delayed, a result that agrees with Clark and Arritt (1995) and Gallus and Segal (2000). However, Gallus and Segal (2000) presented conflicting results as to whether wetter soil would lead to higher accumulated precipitation in the entire domain, depending on the convective parameterization used and the time interval of the accumulation. As mentioned earlier, this is one of the disadvantages of using convective parameterization because of the different closures and grid-spacing dependencies in different convective parameterization. In our cloud-resolving simulations, wetter soil (exp. HOM50) produced the least accumulated convective parameterization. It is clear that convection is harder to initiate with wetter soil (Pielke 2001). However, if convection does occur, it is more likely to be severe and produce heavy precipitation (Chen et al. 2001a). Just before significant convection started in exps. HOM50, API, and HOM31, the maximum upward motion in grid 3 at 700-hPa was 4.5, 3, 2.7 m s^{-1}, respectively. Therefore, this result supports Pielke (2001) and Chen et al. (2001a).

We compare the simulated 3-h accumulated precipitation in grid 3 with the precipitation data from the GCIP archive in order to evaluate the overall performance of RAMS. In exp. API, there was little precipitation in the Texas panhandle in grid 3 (contrary to the observed 3-h accumulated precipitation and most of the convective precipitation was too far north into Kansas (Fig. 4.20a,d). The accumulated precipitation from other experiments also did not correspond exactly to observations (exps. APIMOVES2 and HOM31, Fig. 4.20b,c). However, we wish to re-iterate the fact that our main focus is to test the sensitivity of the initial soil moisture on a real-data cloud-resolving MCS simulation. Nevertheless, RAMS reproduced some aspects of the observed MCS, i.e., RAMS simulated a cloud shield of similar size and shape near the right place and time as compared to observations.

The smoothing operation eliminated the finer scale features of the larger soil moisture anomalies (i.e., S_1 and S_2), but their gross features were still retained. However, the removal of the finer scale features in the larger soil moisture anomalies reduced the internal mesoscale circulations that opposed the PIMSs of the soil moisture anomalies as a whole. As a result of the smoothing, the PIMSs induced by *larger* soil moisture anomalies increased up to 20% (when λ_{cut}=40 km). Once the smoothing continued, i.e., to a cut-off wavelength of 80 km, the small scale features were eliminated and the gradient of the *larger* soil moisture anomalies has been smoothed out to the point such that the PIMSs began to decrease. *Smaller* soil moisture anomalies were *unable* to retain their identities in the smoothing process. *Thus, the PIMSs of the smaller (larger) soil moisture anomalies were underestimated or absent (overestimated) in the smoothed SMI. Nevertheless, the PIMSs induced by the larger soil moisture anomalies were weakly dependent on their internal structure*

From the accumulated precipitation field (Fig. 4.20), as well as the precipitation rates (Figs. 4.13-4.15), precipitation tended to occur less over the large soil moisture anomalies (e.g., S_2). In other words, wetter soil contributes to a negative feedback in subsequent convective precipitation over the wetter soil. Upward motion is suppressed over the wet soil moisture anomaly due to a cooler surface temperature, but enhanced around the periphery of the wet soil moisture anomaly. As a result, the convective cell preferentially continues its development around the periphery of the soil moisture anomaly and does not develop over the wet soil moisture. So, the convective cell tracks around the soil moisture anomaly, and this effect is ultimately related to the strength of the cold pool generated by the soil moisture anomaly. A stronger cold pool would lead to a stronger PIMS (or a stronger divergent wind perturbation). This leads to stronger convergence (or upward vertical motion) around the periphery of the soil moisture anomaly. This means that convection would be

suppressed more over the wet soil anomaly and enhanced more around the periphery of the soil moisture anomaly.

For this case, the initiation of convection was driven mainly by the large-scale forcing (i.e., the quasi-stationary front). However, the soil moisture distribution determined where convection was more likely to occur. In addition, heterogeneous soil moisture played a role during the period when the convection was organizing itself. Once convection was initiated, the PIMS interacted with the convective outflow in some cases and generated additional convective activity. S_2 was the largest and the most influential soil moisture anomaly. However, smaller soil moisture anomalies (i.e., S_4) also played a role, albeit a smaller one. For some convective cells, e.g., C_6 (Fig. 4.14), PIMSs from different soil moisture anomalies collided and initiated convection. For instance, S_4 consisted of two soil moisture anomalies about 30 (northern end) and 40 km (southern end) long in close proximity. Thus, the effects of soil moisture anomalies on the order of several tens of kilometers in size may not be entirely negligible. If we take exp. API as the "ground truth", then a patch size of 30-40 km would be needed to accurately simulate (or forecast) the evolution of the MCS. Exp. API80 began to degrade in performance, e.g., C_6 was quite weak at 26/2145 (Fig. 4.14). We shall see in the next chapter if the results here are consistent or not.

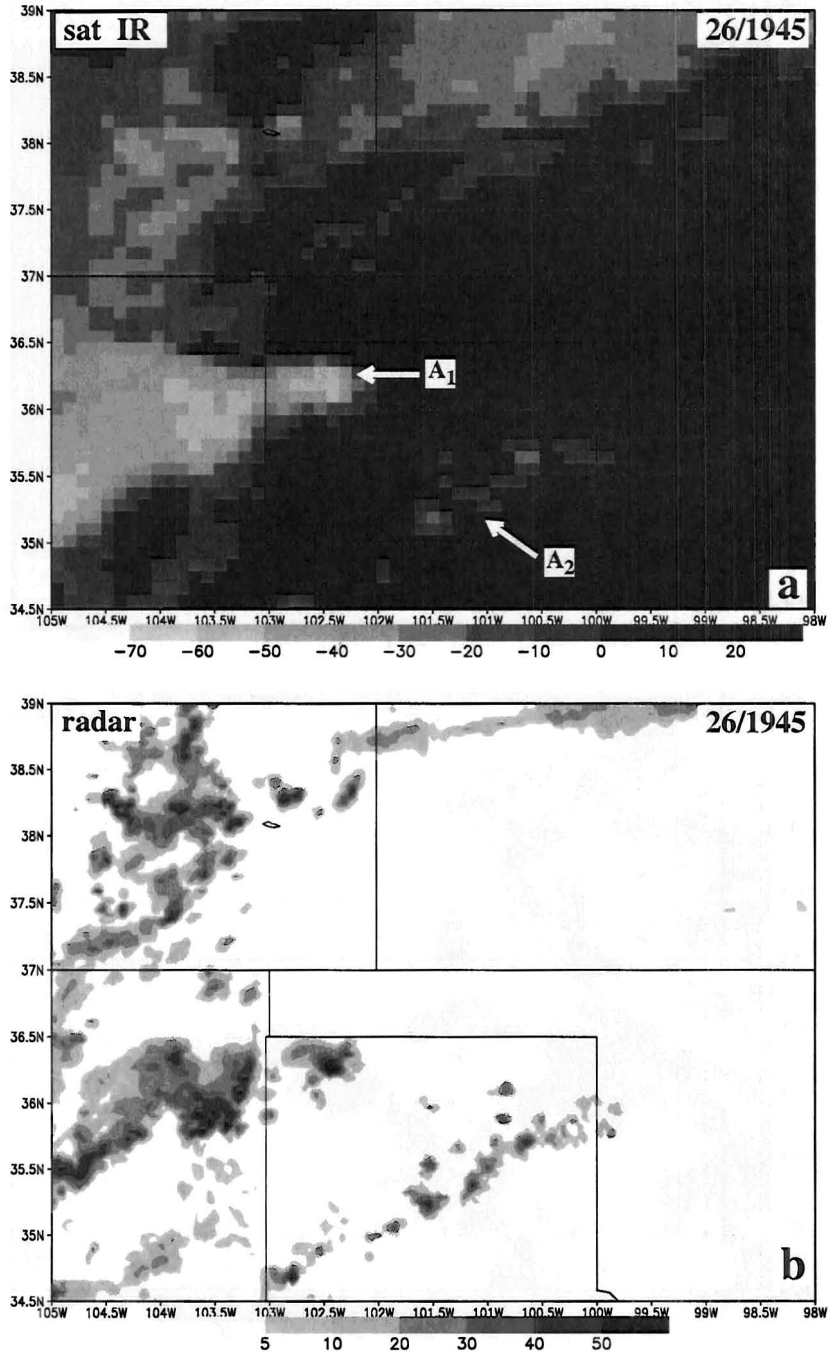

Figure 4.1 Satellite imagery from the NCEP/AWS Infrared Global Geostationary Composite, provided by the Global Hydrology Resource Center: a) 1945 UTC, 26 July 1998; c) 2145 UTC, 26 July 1998; e) 0053 UTC, 27 July 1998. Composite radar reflectivity (dBZ) from the National Weather Service, provided by the Global Hydrology Resource Center: b) 1945 UTC, 26 July 1998; d) 2145 UTC, 26 July 1998; f) 0100 UTC, 27 July 1998.

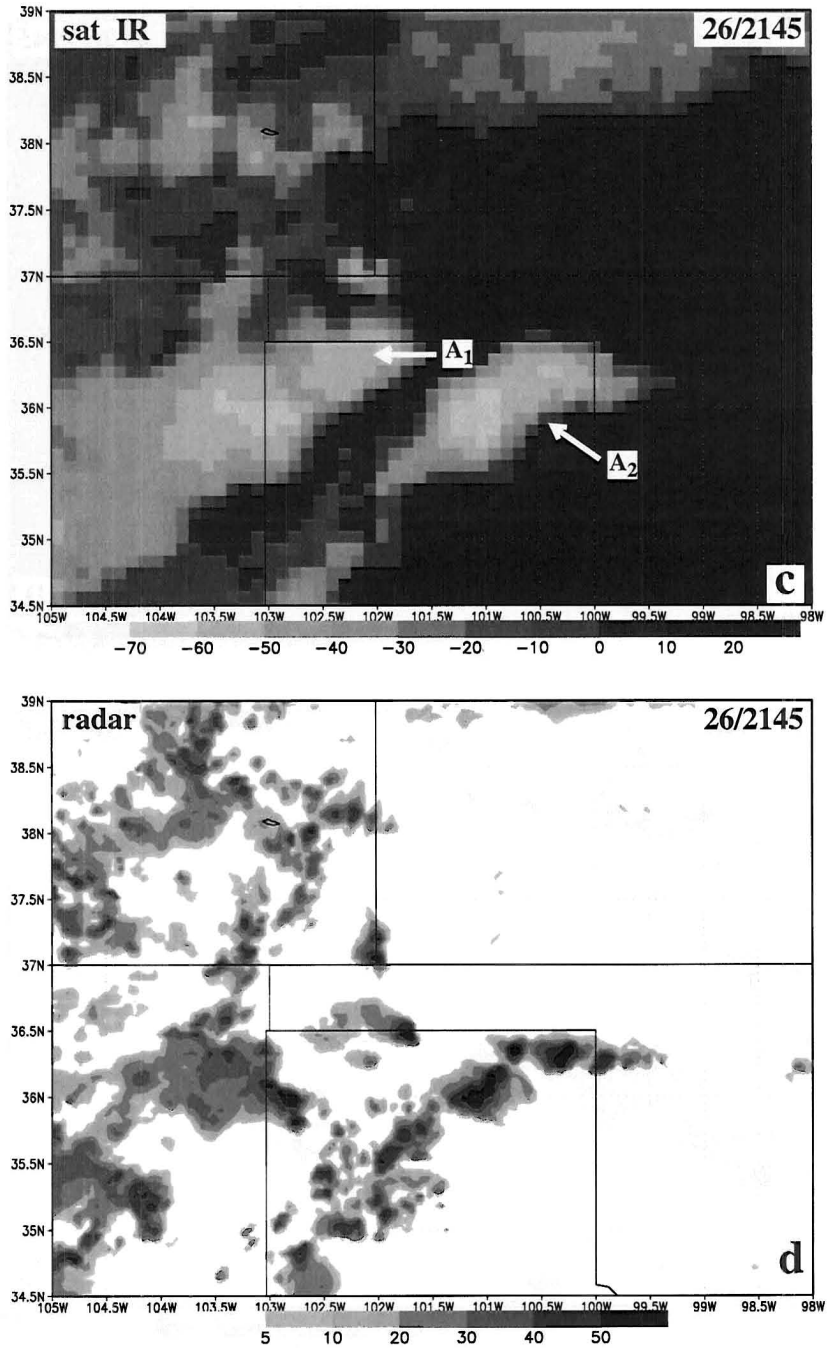

Figure 4.1 Continued.

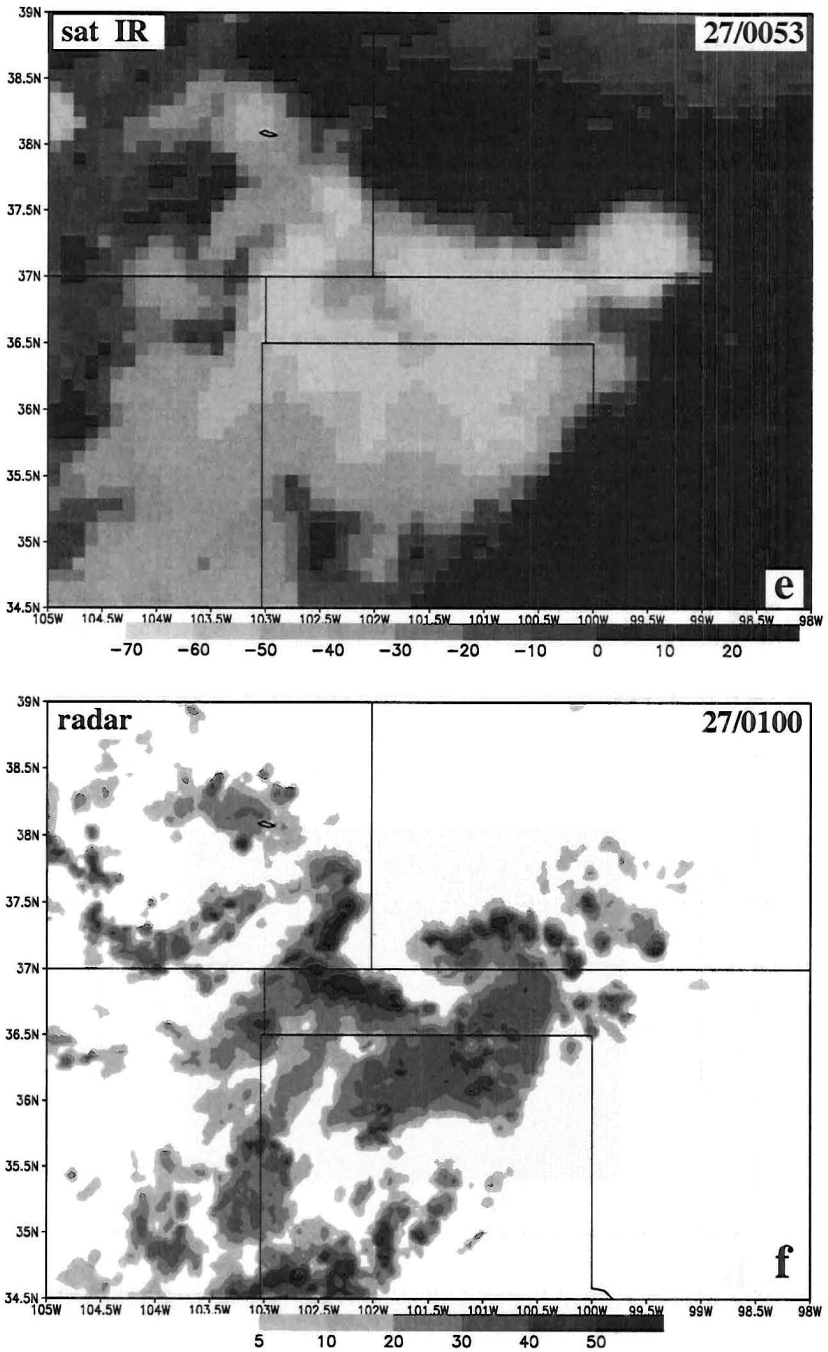

Figure 4.1 Continued.

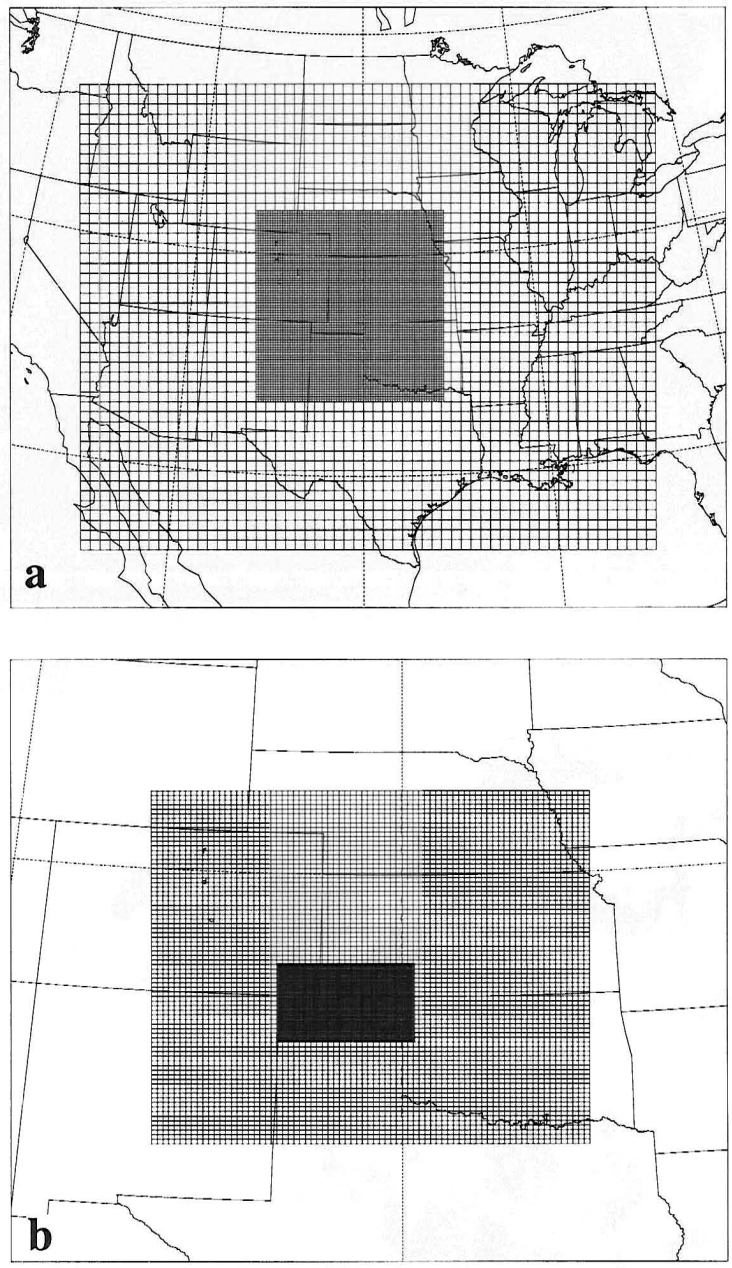

Figure 4.2 a) Nested grid setup for Case 980726 in RAMS with grids 1 and 2; b) nested grid setup in RAMS with grids 2 and 3.

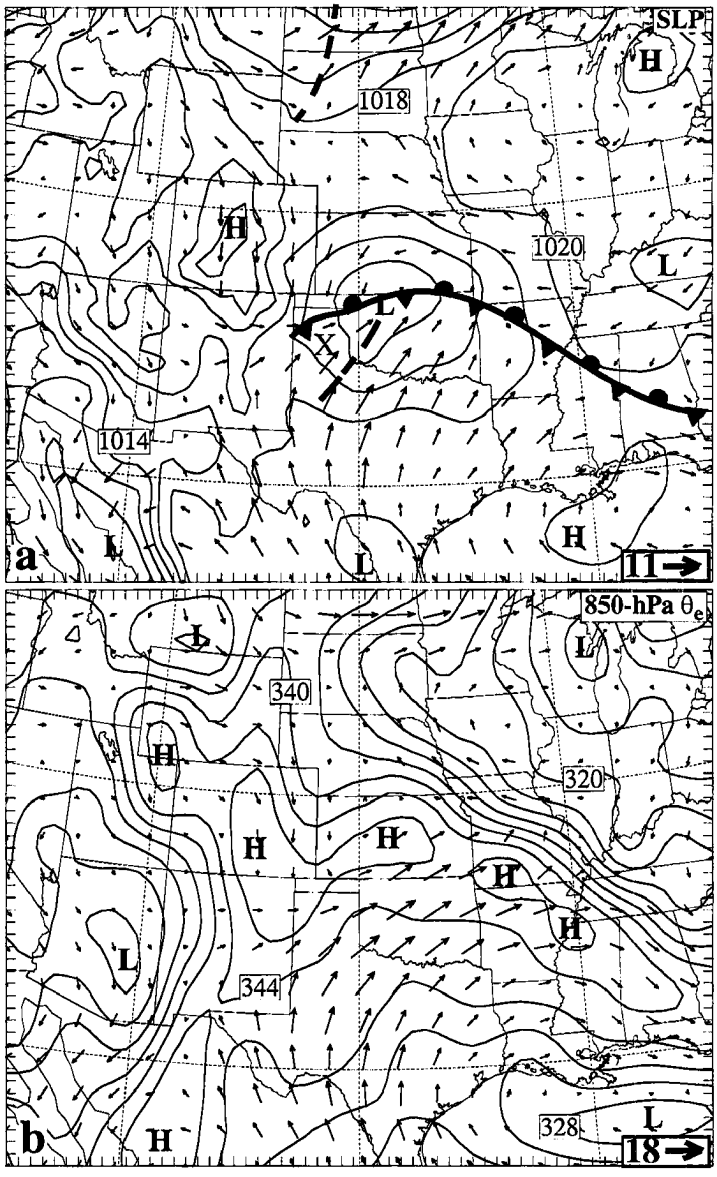

Figure 4.3 From the NCEP global analysis interpolated to RAMS grid 1 in Case 980726 at 26/1200: a) sea-level pressure (contour intervals of 2 hPa) superposed with wind vectors at the lowest σ_z level; b) 850-hPa equivalent potential temperature (contour intervals of 4 K) superposed with 850-hPa wind vectors; c) 400-hPa potential vorticity (with contour intervals of 0.25 PVU) superposed with 400-hPa wind vectors. Insets represent the scale of the wind vectors in m s^{-1}. 'X' in (a) marks the location of Amarillo, Texas.

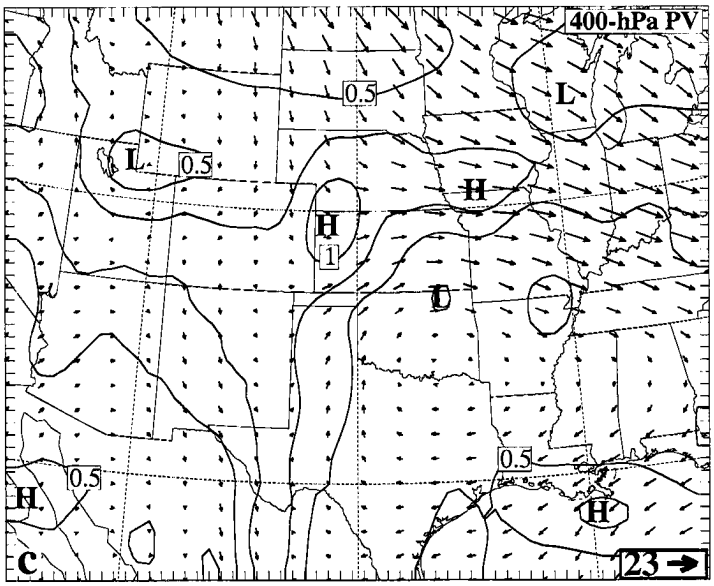

Figure 4.3 Continued.

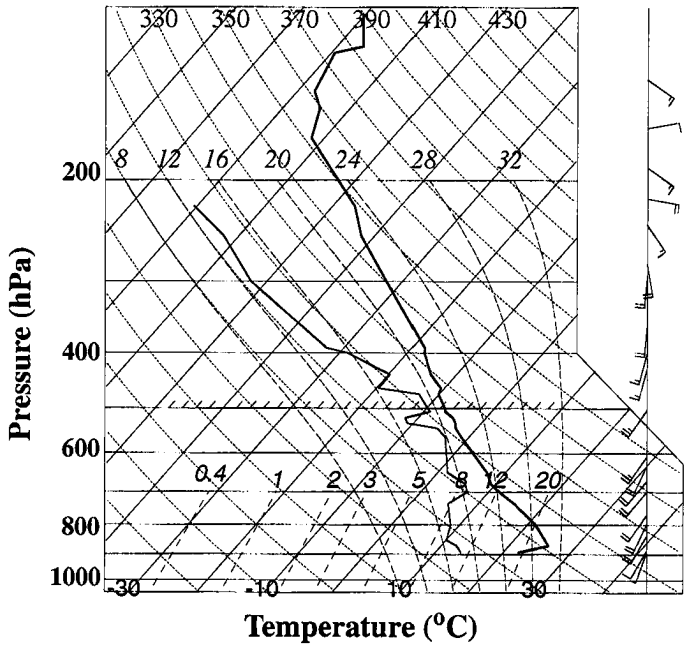

Figure 4.4 Skew T-log p diagram for temperature (°C), dew point temperature (°C), and wind (m s^{-1}) on 1200 UTC 26 July 1998 at Amarillo, Texas ('X' in Fig. 4.3). A full (half) barb is 5 (2.5) m s^{-1}. Data was obtained at NCAR mass storage.

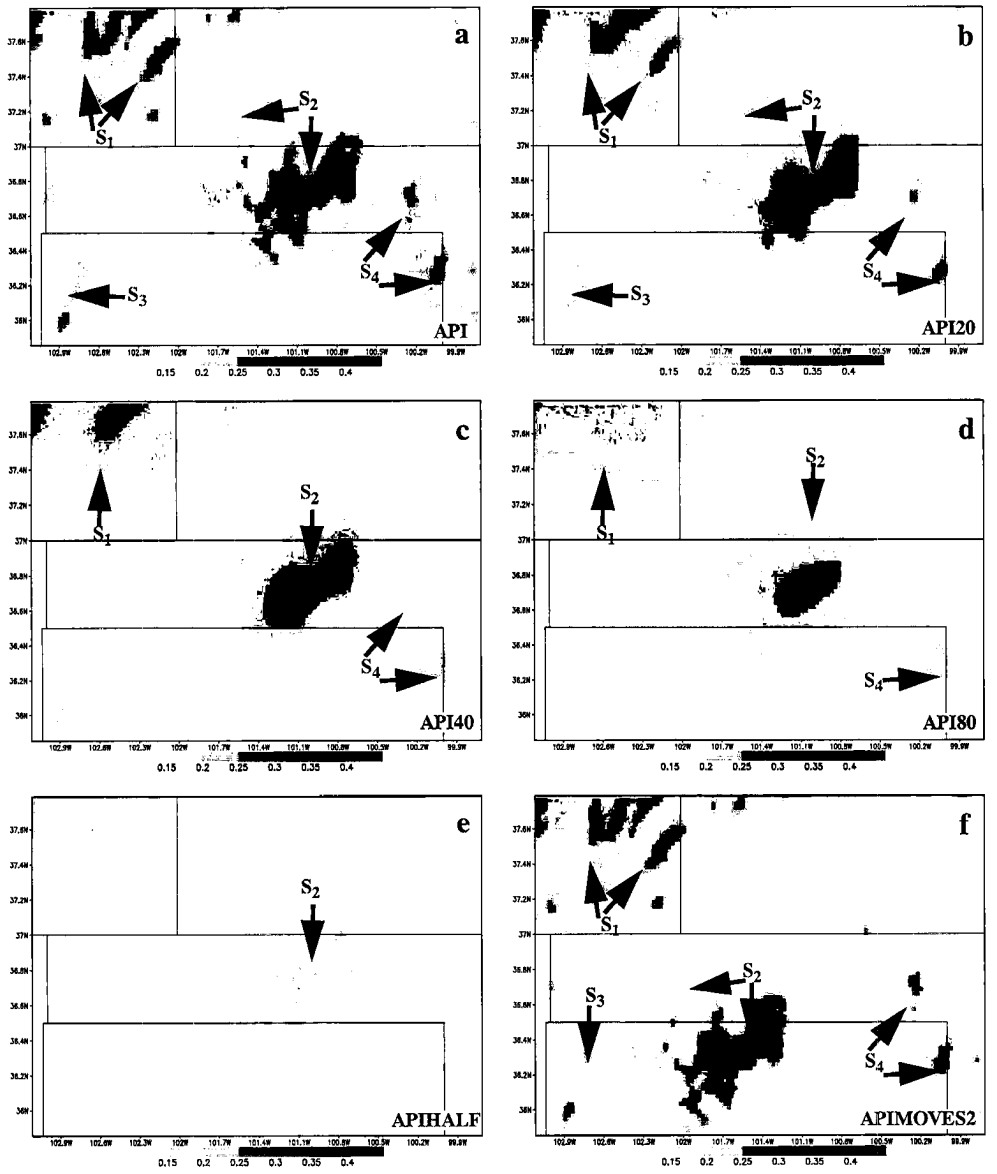

Figure 4.5 Initial volumetric soil moisture ($m^3\ m^{-3}$) in grid 3 for exp. a) API; b) API20; c) API40; d) API80; e) APIHALF; f) APIMOVES2 for Case 980726.

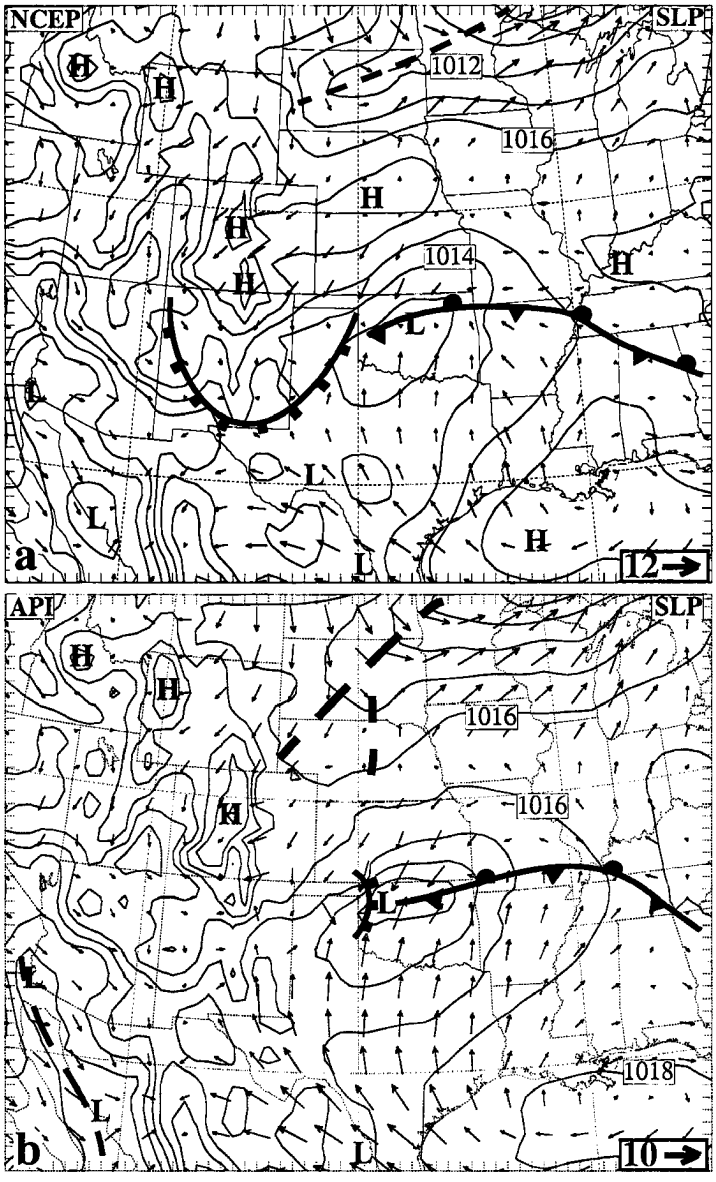

Figure 4.6 a), c), and e) are the same as Fig. 4.3a, b, c, respectively but at 27/ 0000. b), d), and f) are the same as Fig. 4.3a, b, c, respectively, but for exp. API in Case 980726 at 27/0000 in grid 1. The solid curve with square symbols in (a) represents outflow boundaries.

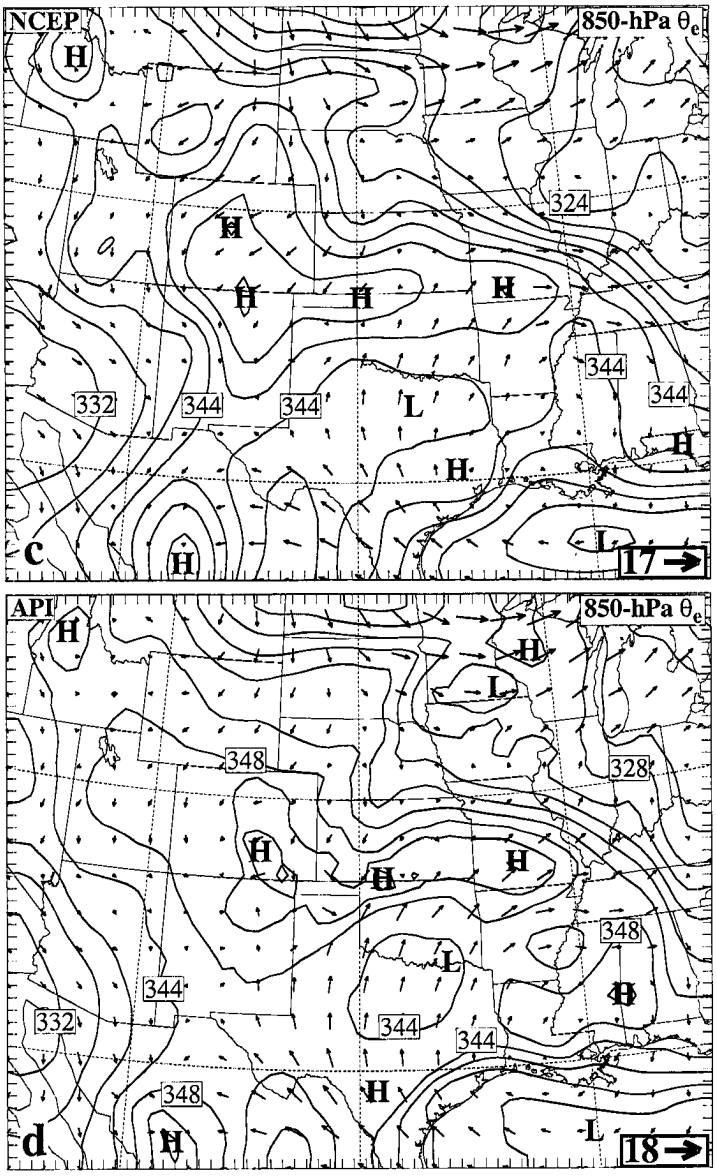

Figure 4.6 Continued.

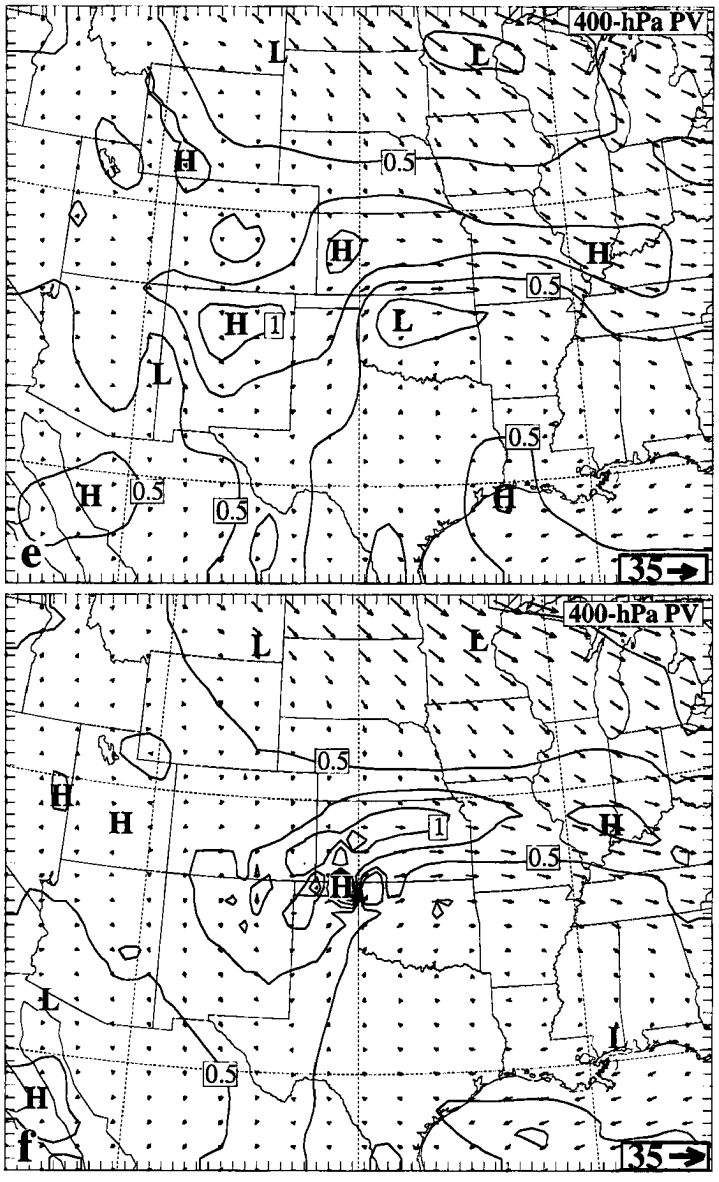

Figure 4.6 Continued.

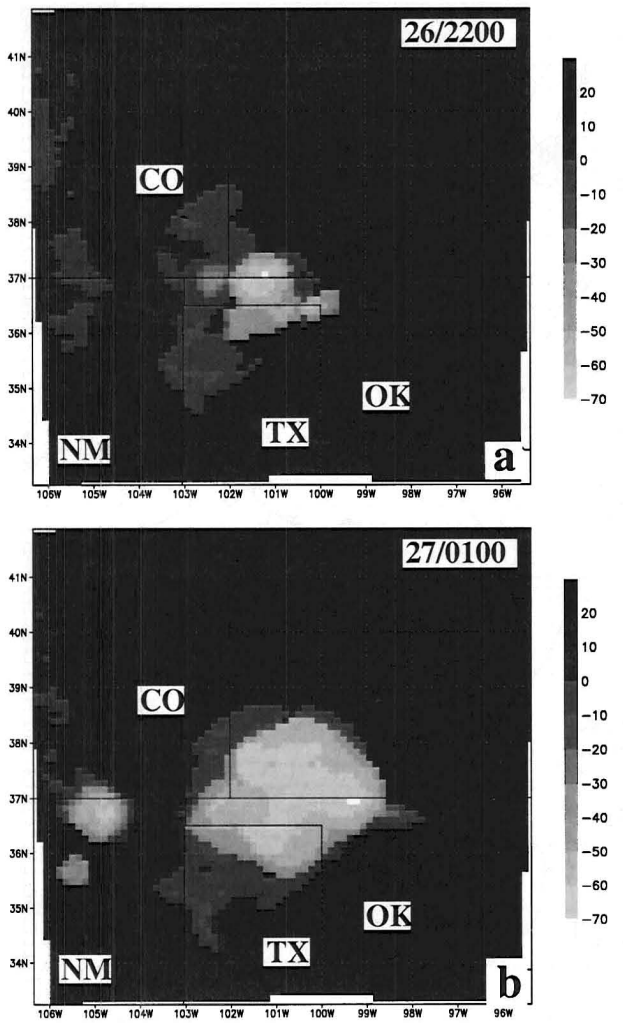

Figure 4.7 Case 980726 cloud top temperature for grid 2 at a) 26/2200; b) 27/0100 for exp. API. CO, NM, TX, and OK stands for Colorado, New Mexico, Texas and Oklahoma, respectively.

Figure 4.8 RAMS grid 3 surface latent heat flux (W m^{-2}) in Case 980726 at 26/ 1600 for exp. a) API; b) API20; c) API40; d) API80; e) APIHALF; f) APIMOVES2; g) HOM31; h) HOM50.

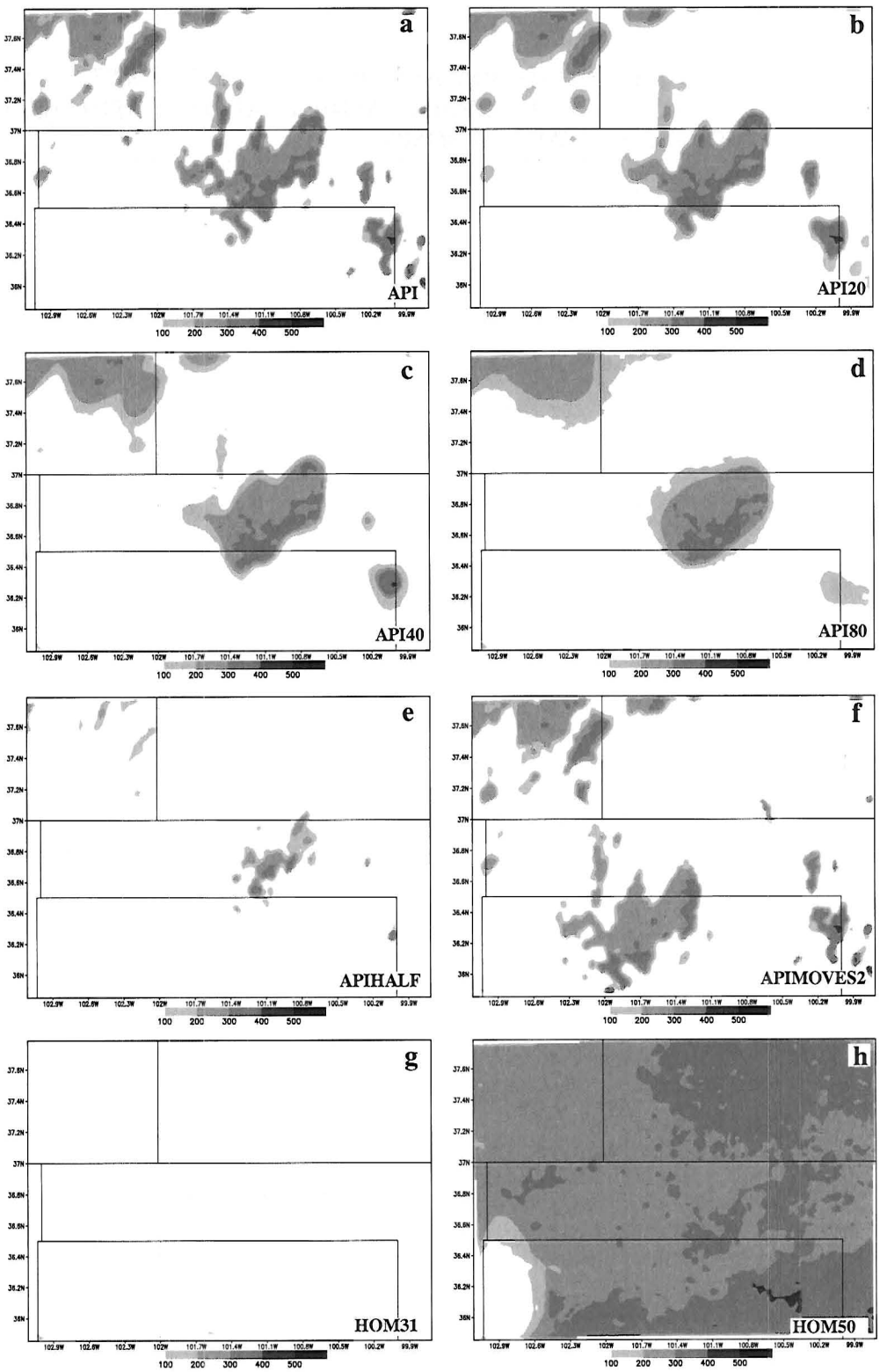
a
API
b
API20
c
API40
d
API80
e
APIHALF
f
APIMOVES2
g
HOM31
h
HOM50
100 200 300 400 500

Figure 4.9 RAMS grid 3 Bowen ratio (SSHF divided by SLHF) in Case 980726 at 26/1600 for exp. a) API; b) API20; c) API40; d) API80; e) APIHALF; f) APIMOVES2; g) HOM31; h) HOM50.

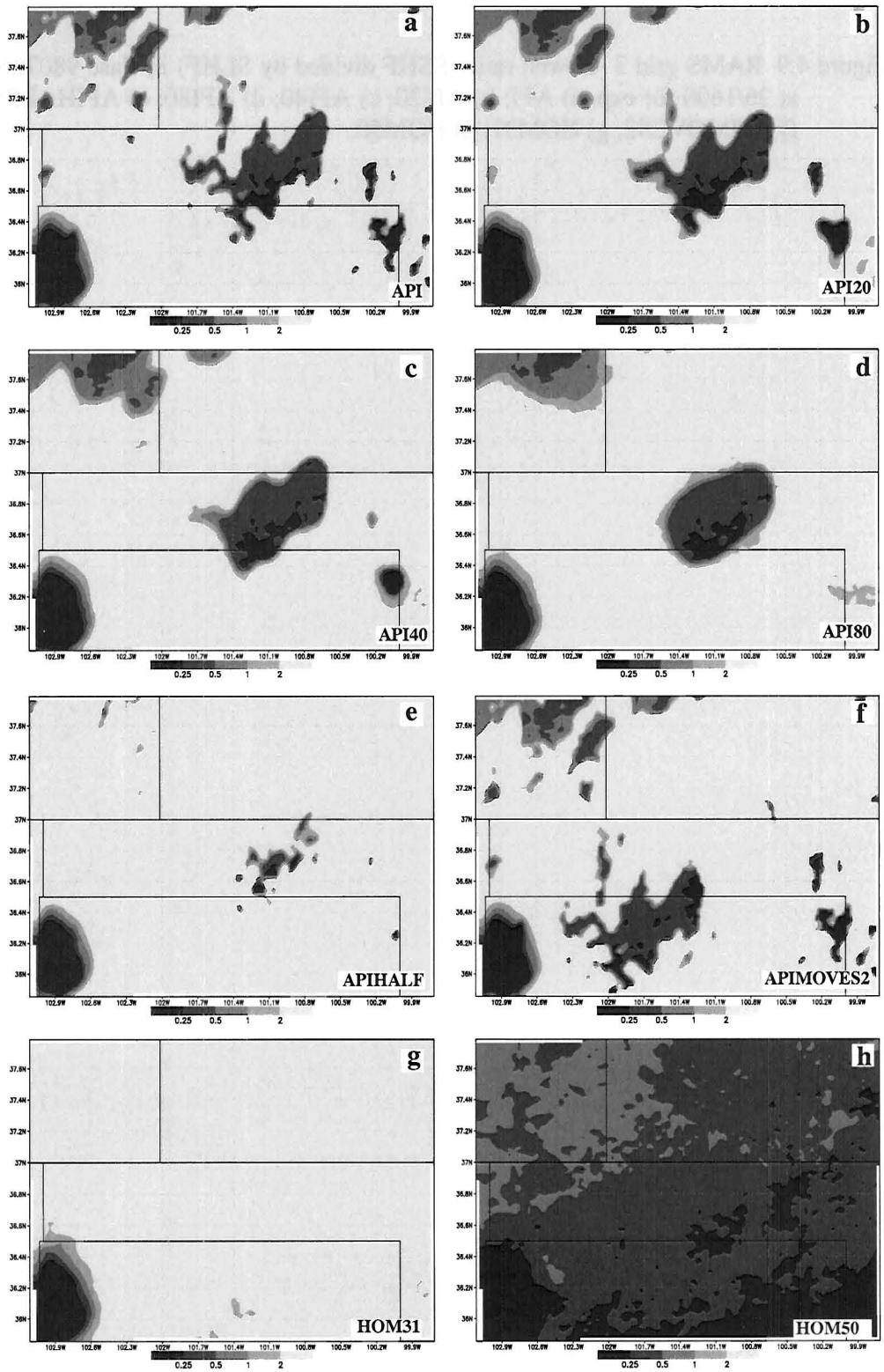
a
API
b
API20
c
API40
d
API80
e
APIHALF
f
APIMOVES2
g
HOM31
h
HOM50

Figure 4.10 RAMS grid 3 dew point temperature at the lowest σ_z level above ground (at contour intervals of 0.5^{o} C) in Case 980726 at 26/1800 for exp. a) API; b) API20; c) API40; d) API80; e) APIHALF; f) APIMOVES2; g) HOM31; h) HOM50.

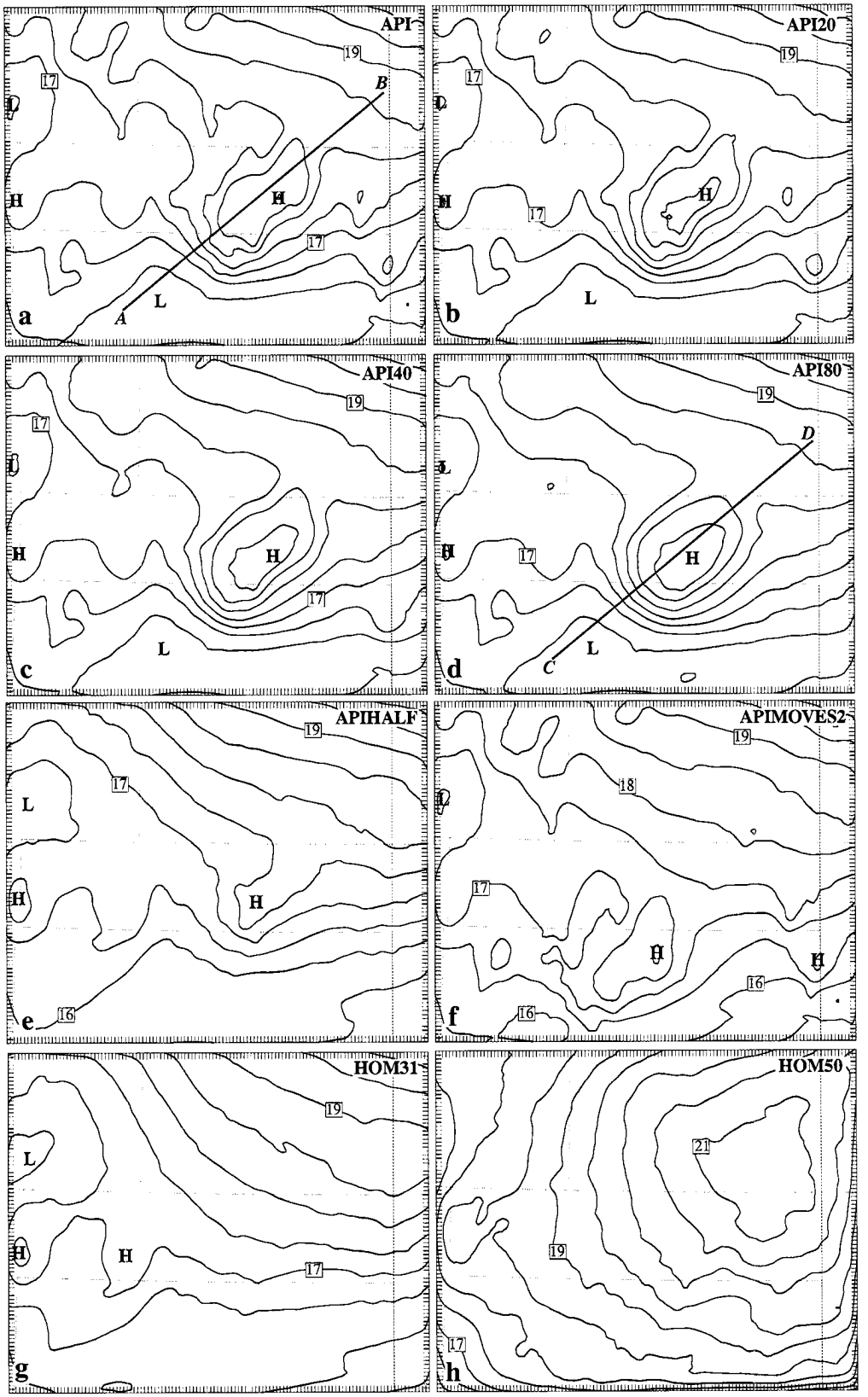
API
19
17
B
L
H
H
17
A
L
a
API20
19
17
L
H
17
L
b
API40
19
17
L
H
H
17
L
c
API80
19
D
L
H
17
H
C
L
d
APIHALF
19
17
L
H
H
16
e
APIMOVES2
19
18
L
17
H
H
16
16
f
HOM31
19
L
H
H
17
g
HOM50
21
19
17
h

Figure 4.11 RAMS grid 3 vertical velocity difference at the lowest σ_z level above ground (thick contours, every 2 cm s^{-1}) and sea-level pressure difference (light contours, every 0.25 hPa) superposed with the difference in horizontal wind vectors at the lowest σ_z level above ground in Case 980726 at 26/1800 for exp. a) API-HOM31; b) API20-HOM31; c) API40-HOM31; d) API80-HOM31; e) APIHALF-HOM31; f) APIMOVES2-HOM31; g) HOM50-HOM31. Solid (dashed) contours represent positive (negative) values, and zero-contour is suppressed. Insets in panels represent the scale of the wind vectors in m s^{-1}.

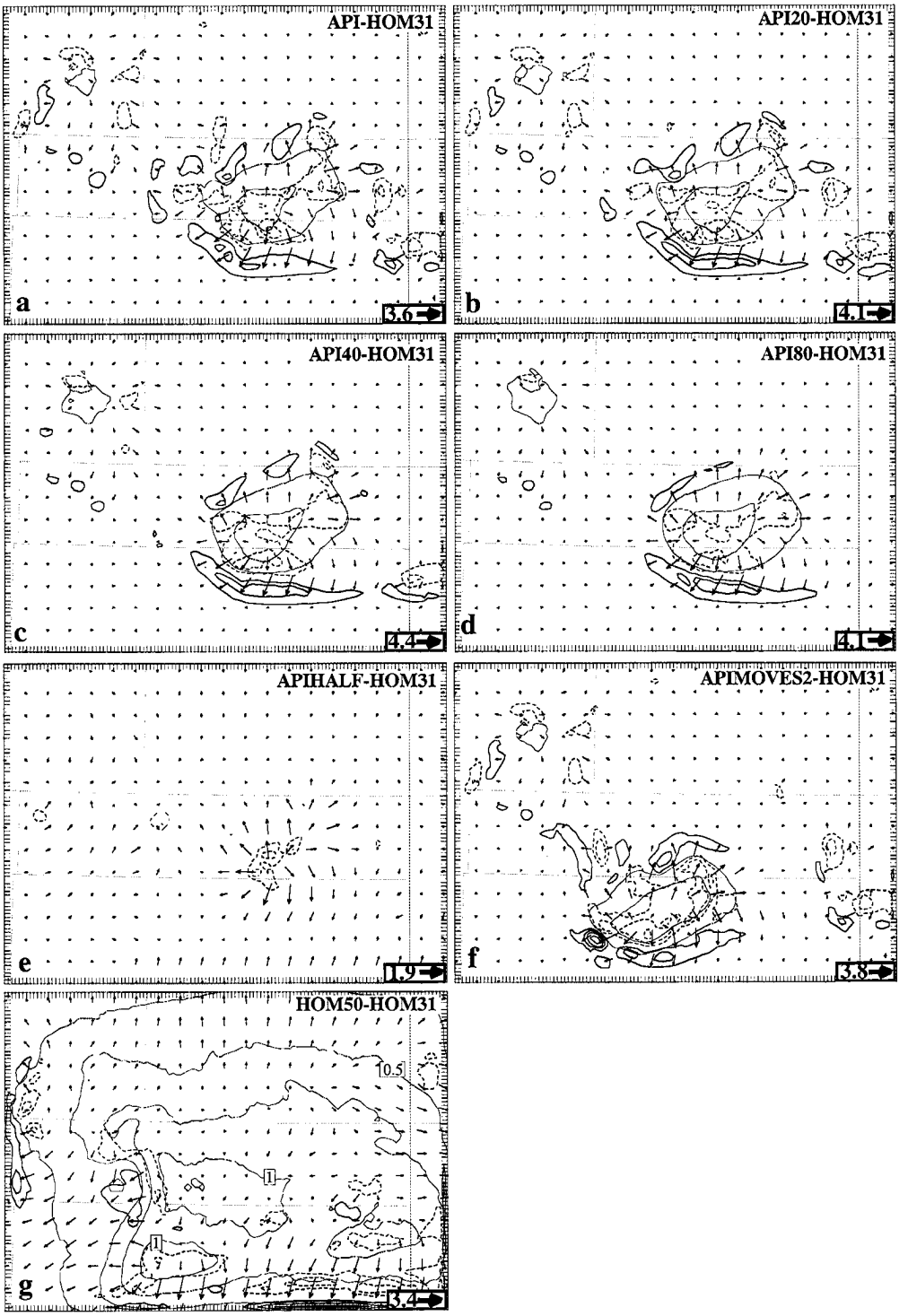
API-HOM31
a
3.6
API20-HOM31
b
4.1
API40-HOM31
c
4.4
API80-HOM31
d
4.1
APIHALF-HOM31
e
1.9
APIMOVES2-HOM31
f
3.8
HOM50-HOM31
10.5
g
3.4

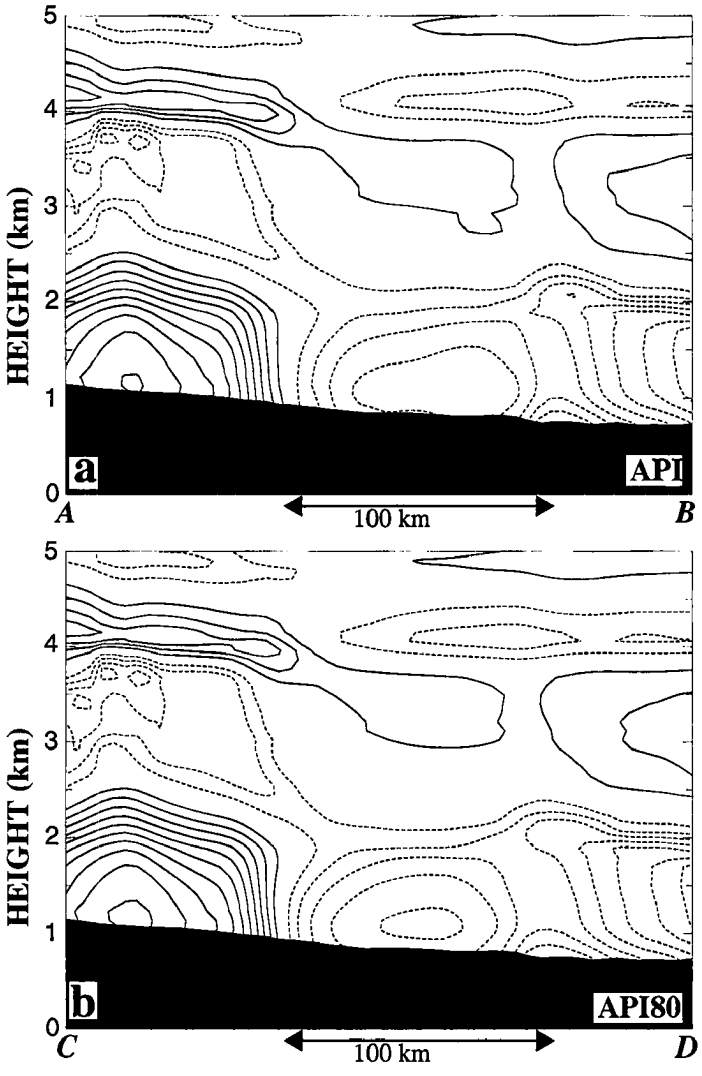

Figure 4.12 a) Vertical cross section of horizontal temperature deviation (at contour intervals of 0.25 K) taken through lines in Fig. 4.10 for exps. a) API; b) API80 in Case 980726 at 26/1800. Zero-contour is suppressed, and solid (dashed) contours represent positive (negative) values.

Figure 4.13 RAMS grid 3 precipitation rate (at contour intervals of 1, 5, 10, 20 , 40, 80 and 120 mm h^{-1}) in Case 980726 at 26/1915 for exp. a) API; b) API20; c) API40; d) API80; e) APIHALF; f) APIMOVES2; g) HOM31; h) HOM50. Dashed contour represents initial volumetric soil moisture at 50% saturation.

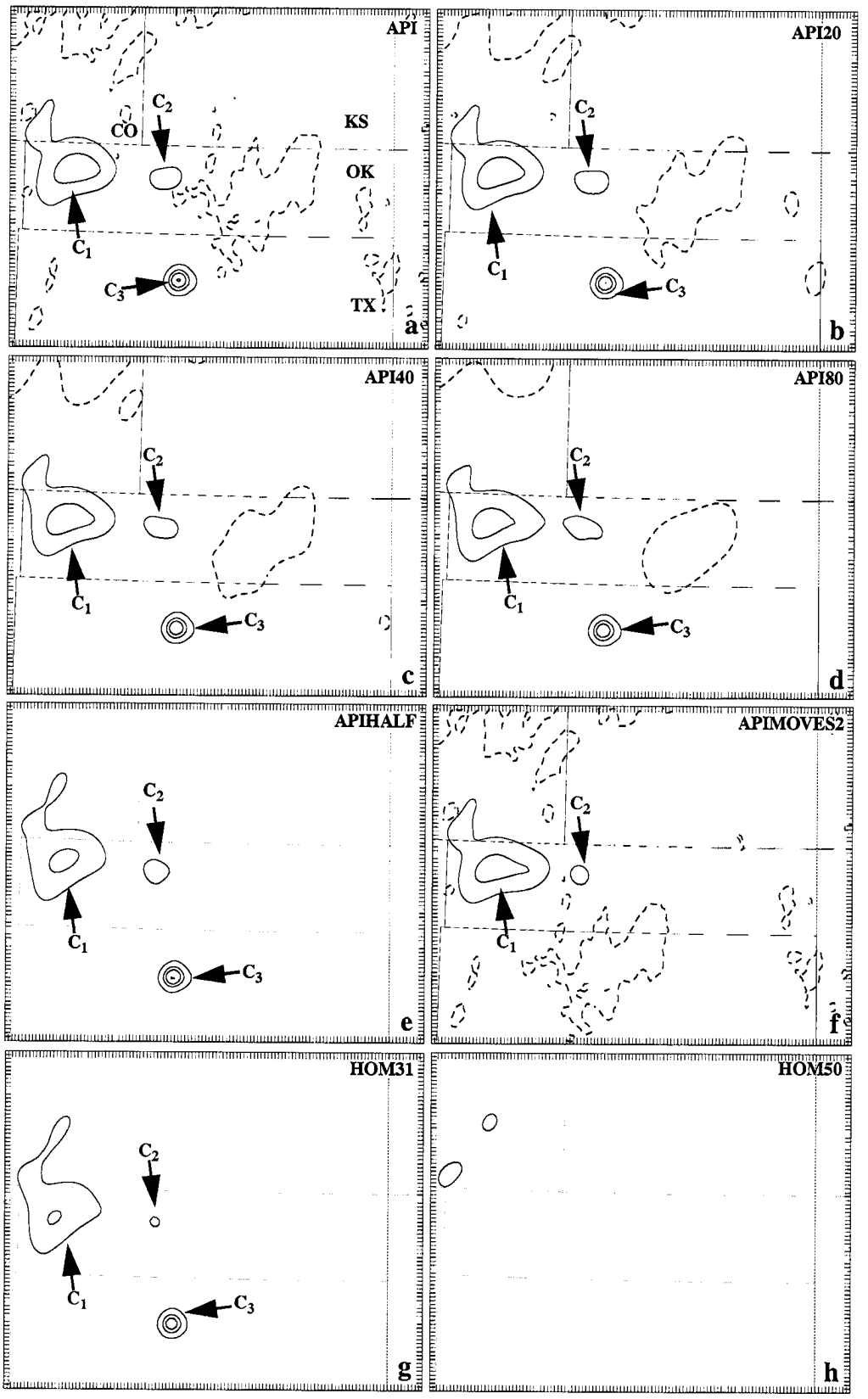
API
CO
KS
OK
TX
C1
C2
C3
a
API20
b
API40
c
API80
d
APIHALF
e
APIMOVES2
f
HOM31
g
HOM50
h

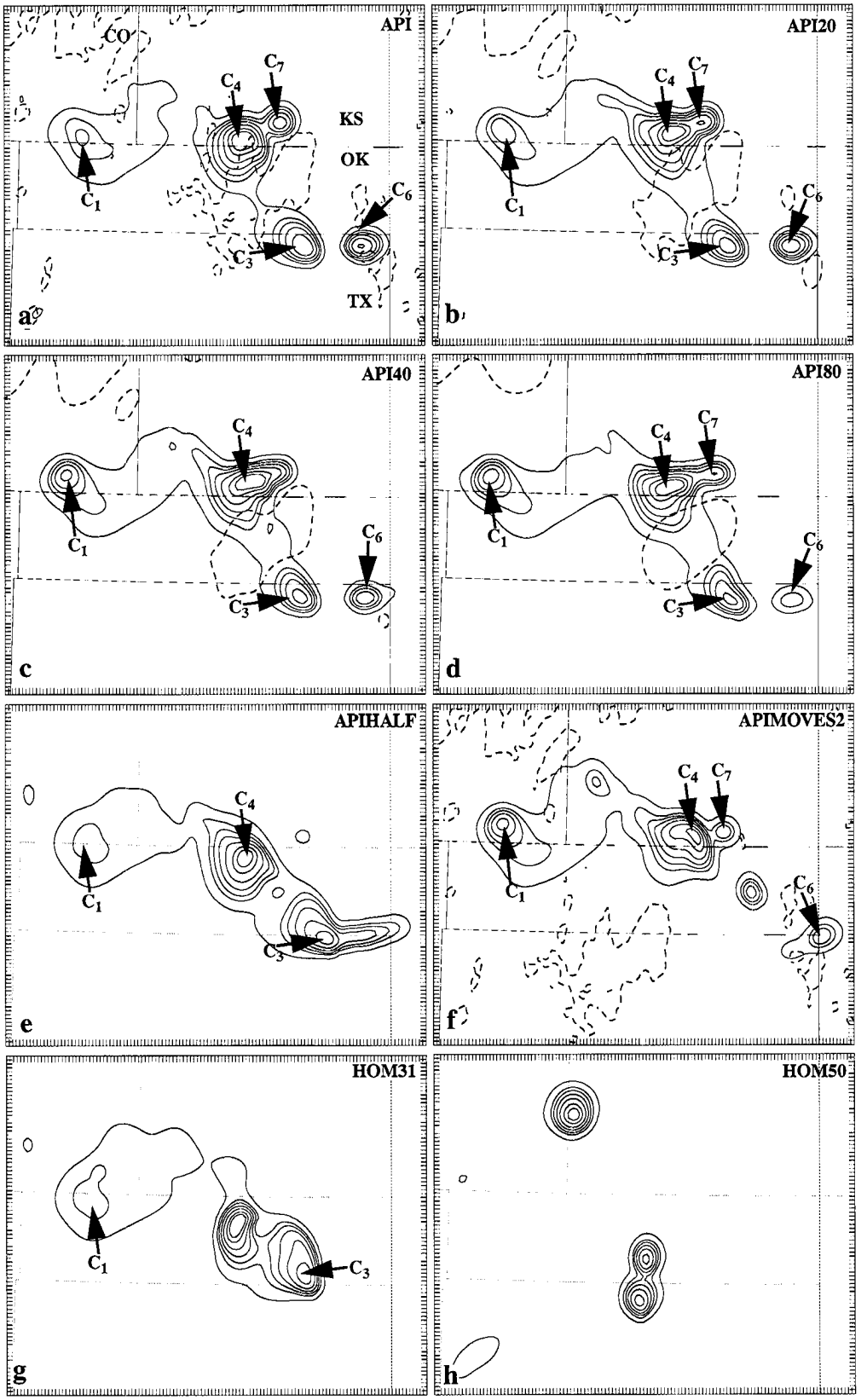

Figure 4.14 As in Fig. 4.13 but for 26/2145.

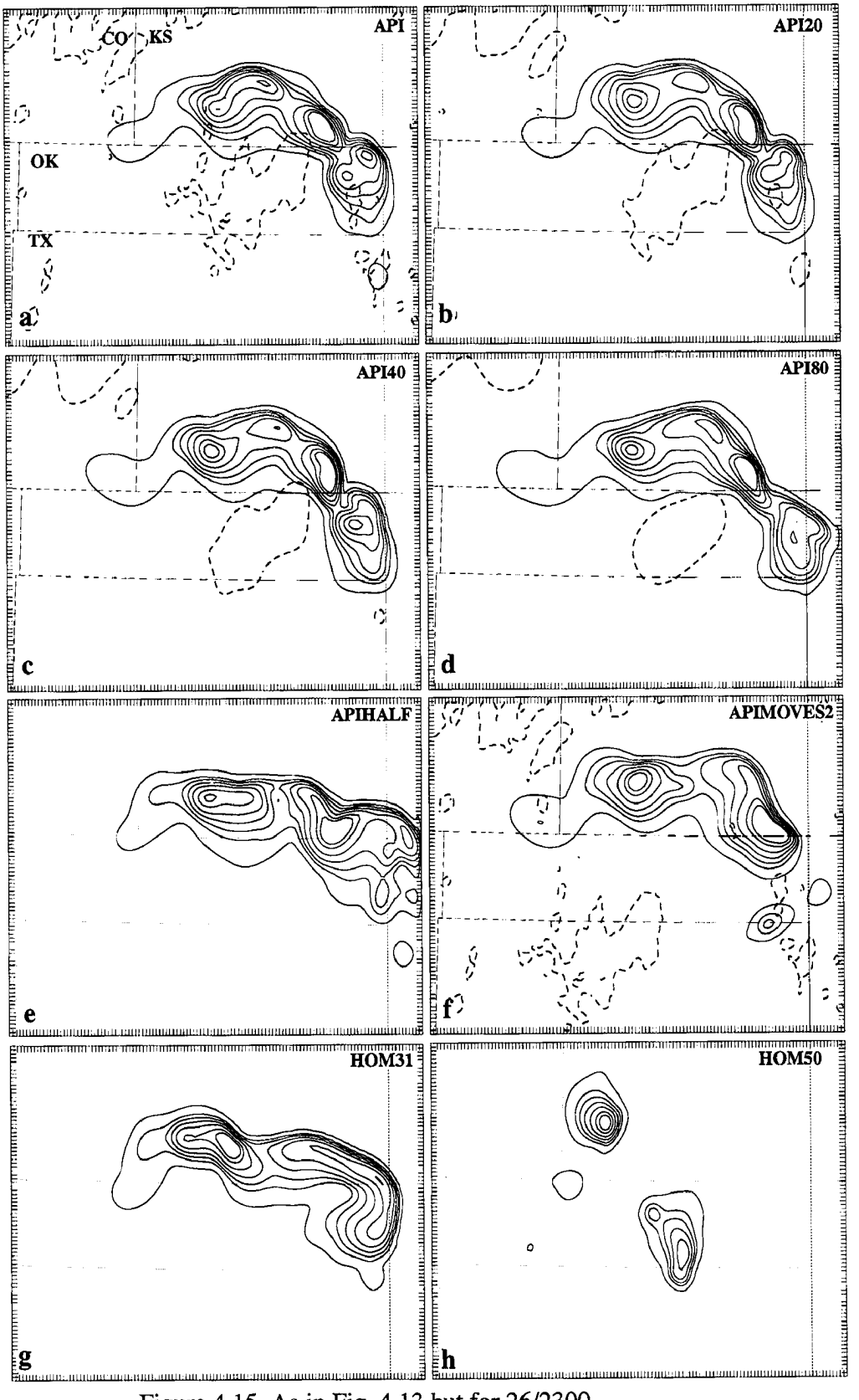

Figure 4.15 As in Fig. 4.13 but for 26/2300.

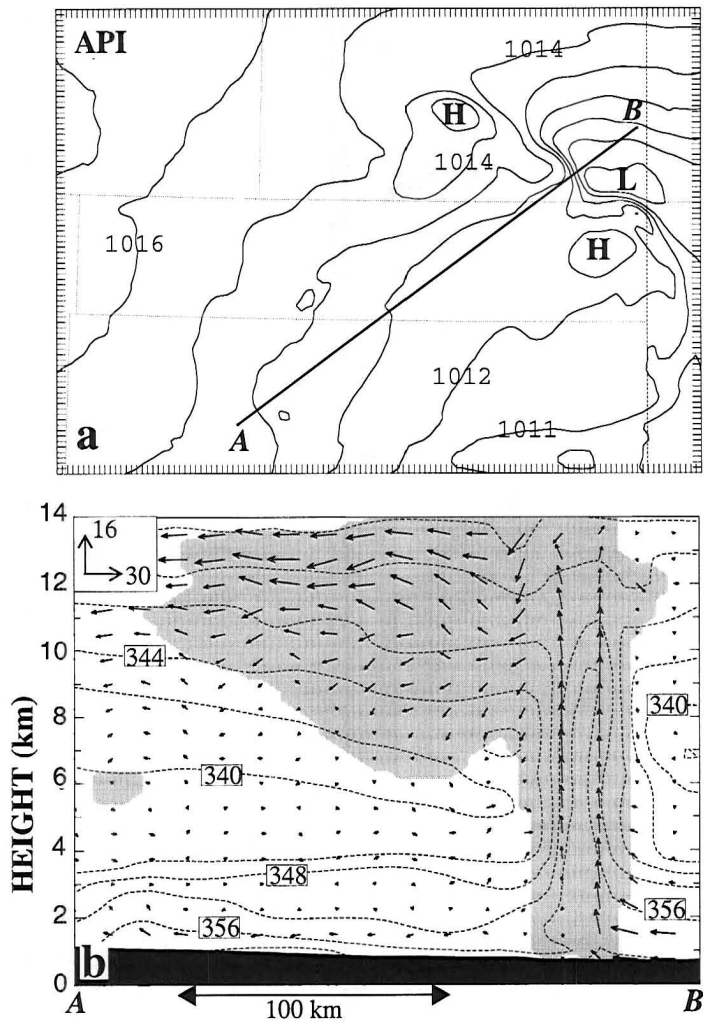

Figure 4.16 a) Sea-level pressure (at contour intervals of 1 hPa) in Case 980726 for exp. API at 26/2300; b) vertical cross section of equivalent potential temperature (dashed contours) at intervals of 4 K, superposed with along-plane MCS-relative wind vectors, along line AB given in (a). Shading denotes total condensate mixing ratio > 0.1 g kg^{-1}. Inset indicates the scale of vertical motion (m s^{-1}) and horizontal wind speed (m s^{-1}). c) same as in (a) but for exp. HOM; d) same as in (b) but for exp. HOM along line CD in (b).

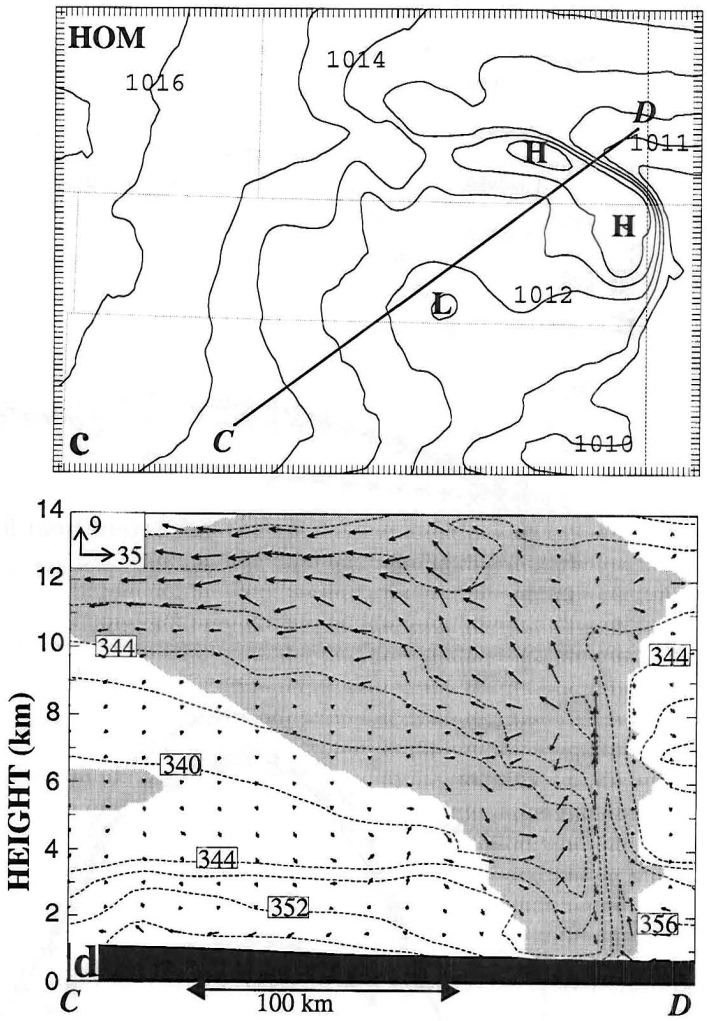

Figure 4.16 Continued.

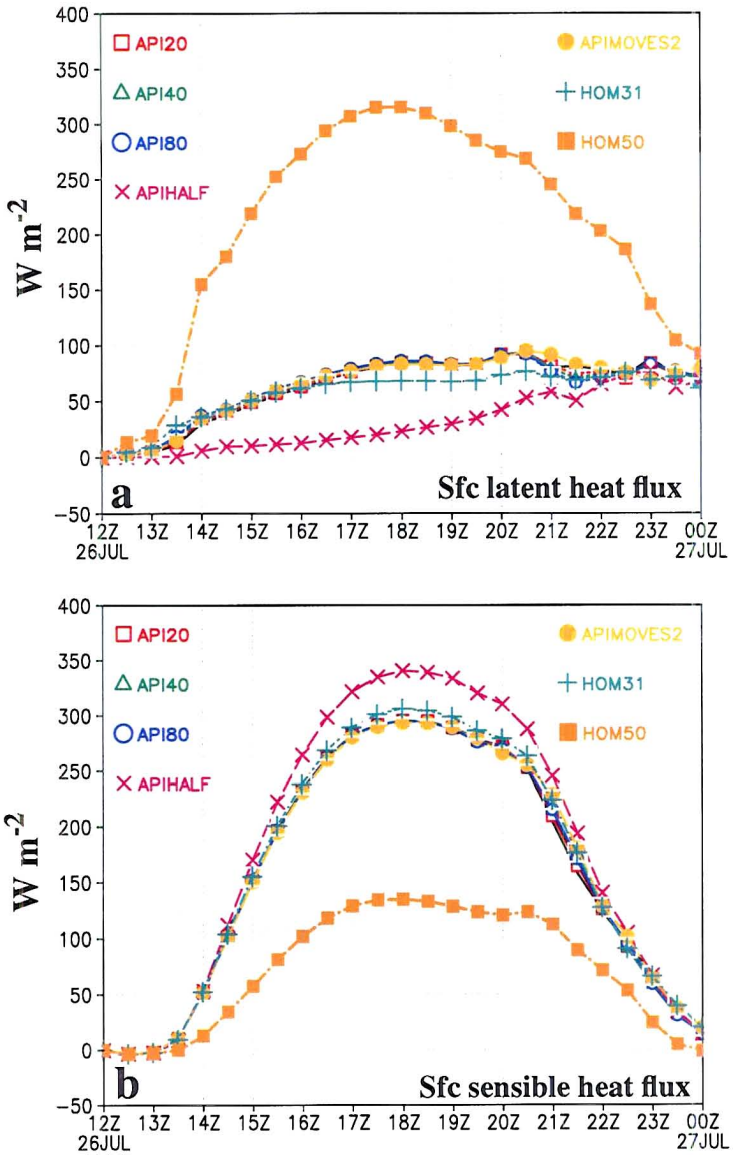

Figure 4.17 Time series of grid 3 domain-averaged a) surface latent heat flux (W m^{-2}); b) surface sensible heat flux (W m^{-2}); c) convective available potential energy (CAPE, J kg^{-1}) in Case 980726. Exp. API is represented by the solid curve. Symbols for the other experiments are indicated in the figure.

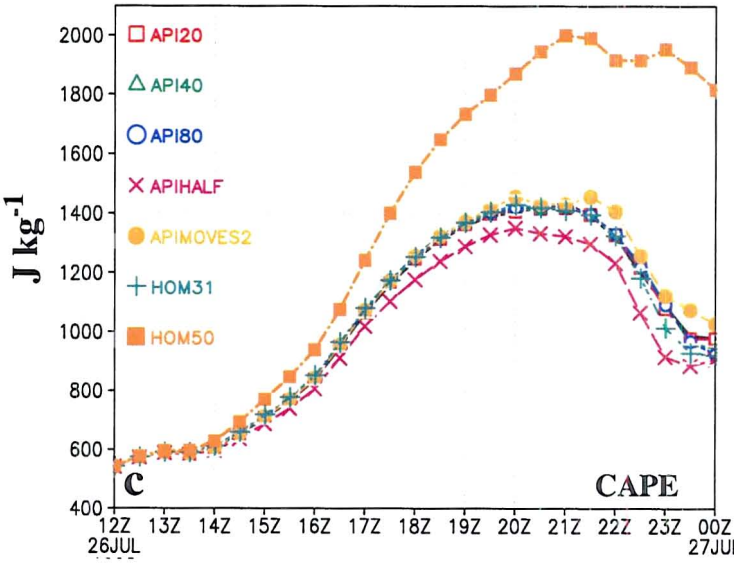

Figure 4.17 Continued.

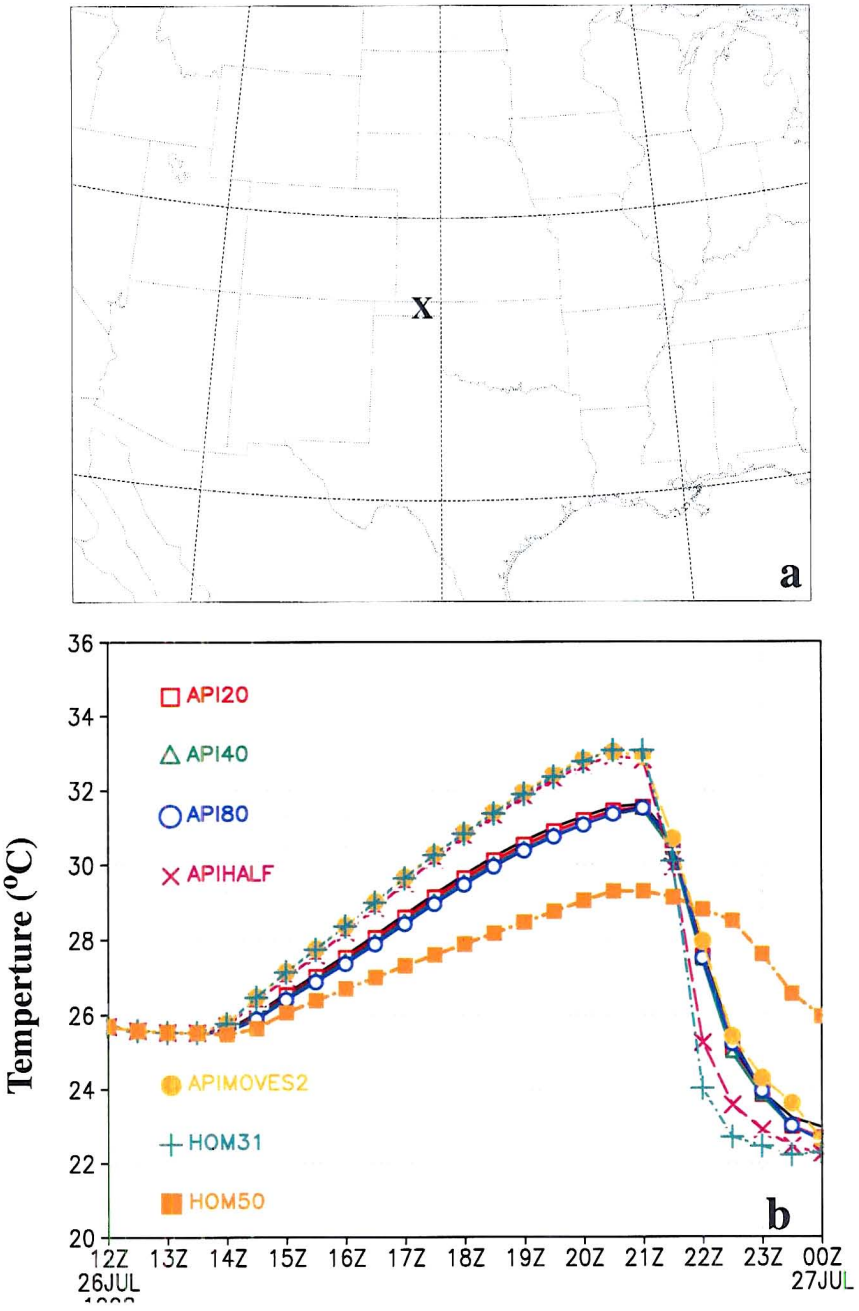

Figure 4.18 a) Grid 1 for Case 980726; b) time series of temperature (°C) at the lowest σ_z-level in grid 1 for the various experiments in Case 980726 over the location marked 'X' in (a). Solid curve in (a) is for exp. API, and the symbols for the other experiments are indicated in the legend.

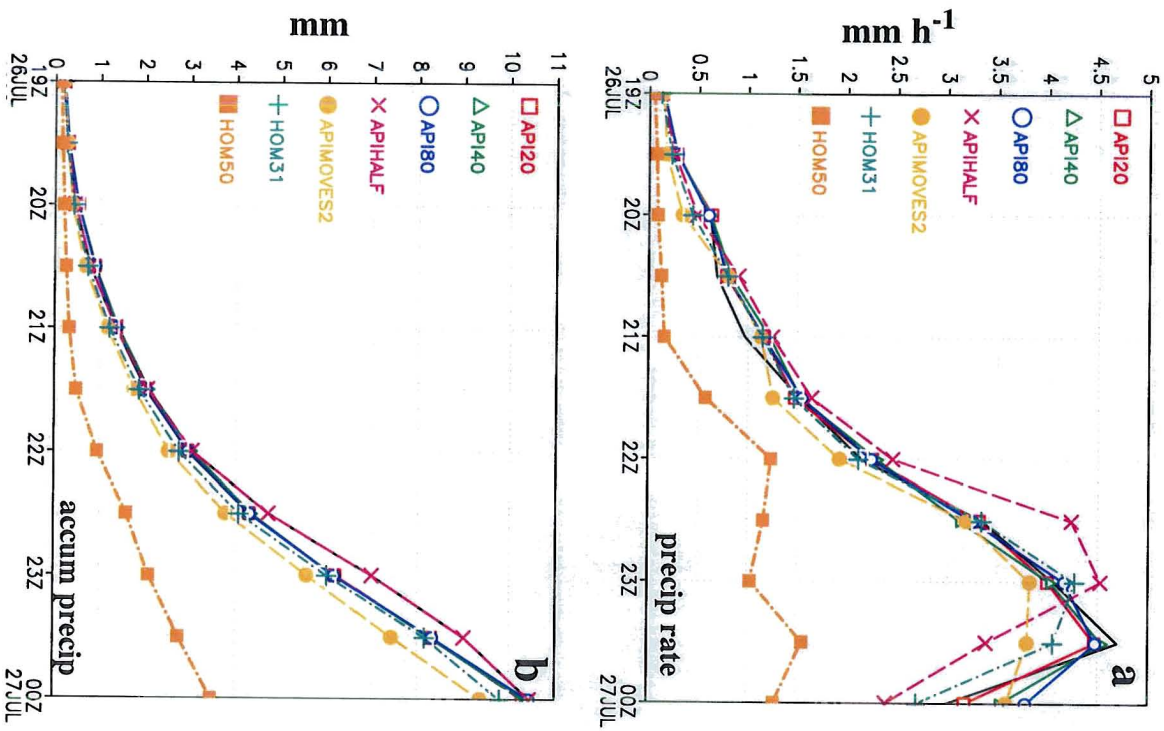

Figure 4.19 Time series of grid 3 domain-averaged a) precipitation rate (mm h^{-1}); b) accumulated precipitation (mm) in Case 980726. Exp. API is represented by the solid curve. Symbols for the other experiments are indicated in the figure.

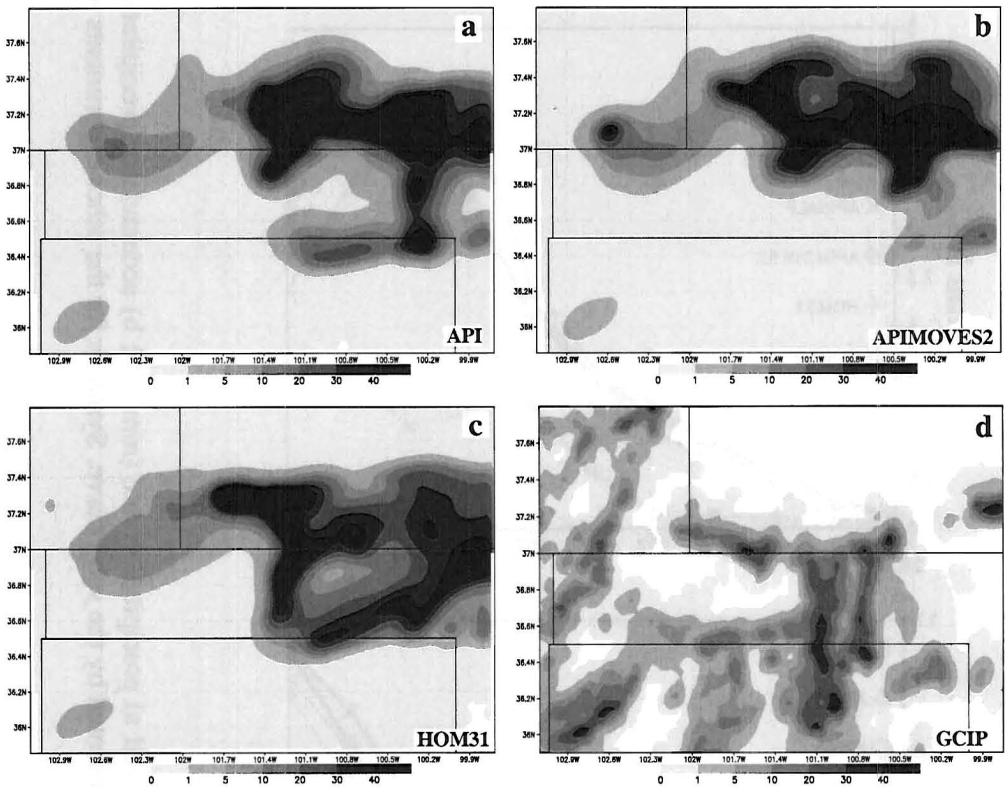

Figure 4.20 3-h accumulated precipitation (mm) in Case 980726 from 26/2100 to 27/0000 for exp. a) exp. API; b) exp. APIMOVES2; c) exp. HOM31; d) 4-km GCIP precipitation database.

Chapter 5

AUGUST 2, 1999 MCS CASE

The second MCS in this study was initially a linear system, but eventually evolved into a small quasi-circular system (although too small to be a MCC) shortly before dissipation. We tried to repeat the same procedure in testing the soil moisture initialization sensitivity for this case to determine if our results can be generalized. Convection was more random-like, rather than a squall line type convection as in Case 980726. This system was also quasi-stationary, thus not requiring moving grids in the numerical simulations. This case occurred between 2045 UTC, 2 August 1999 (02/2045) and 0445 UTC, 3 August 1999 (03/0445). We shall refer to this MCS case as "Case 990802".

5.1 Case 990802

At 02/2045, under the favorable synoptic conditions provided by a quasi-stationary front and a surface trough (shown later), convection developed in an arch shape pattern, in western Oklahoma, eastern Oklahoma/Arkansas border and near the Kansas/Oklahoma border (Fig. 5.1a,b). About an hour and a half later (02/2215), still maintaining an arch shape pattern, convection intensified and covered a larger area (Fig. 5.1c,d). By 02/2345, there were four distinct convective clusters (Fig. 5.1e,f), one in western Oklahoma (B_1), one over the Kansas/Oklahoma border (B_2), one over the Oklahoma/Arkansas/Missouri border (B_3)

and one in eastern Oklahoma (B_4). At this time, convection was more random-like with convective cells embedded in the stratiform regions (low reflectivity areas). By 03/0145, B_1 and B_2 merged into a linear MCS (elliptical shape) covering parts of Oklahoma and Kansas (Fig. 5.1g,h). B_3 moved into Missouri and was dissipating by 03/0145, and B_4 also showed signs of weakening at this time. The merged system of B_1 and B_2 survived several more hours beyond 03/0145. By 03/0345, the MCS reached maturity and evolved into a quasi-circular MCS and dissipated in the next hour. Convection at this time was still random-like. Because of the limited computing resources, we chose not to simulate B_3 and B_4 but concentrated on the dominant systems (B_1 and B_2).

5.2 Model Initial Conditions

5.2.1 Model setup/initial conditions

With two levels of nesting, the grid setup was similar to that of Case 980726 (Fig. 5.2, Table 5.1). In addition, we used the same vertical grid spacings (Table 4.2) and model physics as in Case 980726. RAMS was initialized on 1200 UTC, 2 August 1999 (02/1200) with the Rapid Update Cycle (RUC) analysis. RUC analysis also provided nudging boundary conditions for grid 1's five outermost grid points[1]. Figure 5.3 shows the model initial conditions. At 02/1200, a quasi-stationary front extended from a sea-level low in central Oklahoma, through the Kansas/Oklahoma border, to western Missouri (Fig. 5.3a). From western Missouri, the frontal boundary became a cold front and stretched eastward into the southeastern states. Also, a surface trough stretched from Kansas, through Oklahoma, into Texas. A high pressure system centered near Iowa/Minnesota border extended its influence over most of the CONUS. There was also a subtropical high over the Gulf of

[1]Note that we did not use RUC analysis in Case 980726 because the run initialized with RUC analysis did not produce very good results. Also, the boundary condition file at 12-h was missing in the RUC analysis and had to be substituted from the NCEP analysis.

Mexico whose center lies beyond the domain of the plot, but its influence reached central Oklahoma. At 850-hPa, a tongue of high-θ_e air extended from the Gulf of Mexico to eastern Oklahoma and southwestern Oklahoma, providing favorable conditions for convection to develop (Fig. 5.3b). The 400-hPa PV map is absent of PV anomalies upstream of the genesis region, and the PV maximum centered over Kansas corresponded to a dissipating MCS (Fig. 5.3c). Just like Case 980726, the surface frontal boundary and intrusion of high-θ_e air into the genesis region provided the favorable environment for the development of the MCS in Case 990802.

Table 5.1: Horizontal grid setup for Case 990802.

number of grids	3
number of x points	60, 78, 87
number of y points	48, 78, 122
number of σ_z points	36, 36, 36
horizontal grid spacing (km)	50, 12.5, 2.5

A sounding (Fig. 5.4) taken closest to the location of the genesis of the MCS (at Oklahoma City, south of the quasi-stationary front, Fig. 5.3a) reveals a shallow layer of temperature inversion (less than 25-hPa deep) at the surface. The sounding was relatively dry, and the CAPE was very low at this time, with a value of 170 J kg^{-1}. At the lowest 70-hPa, the wind veered from southeasterly to southwestly with height (with a maximum wind speed of 8 m s^{-1} within this layer), indicating warm advection. Above 900-hPa, the wind, as well as the wind shear were generally weak. Between 900-hPa and 700-hPa, the wind backed from southwesterly to easterly with height. Also, between 700-hPa and 400-hPa, the wind veered from easterly to southwesterly with height. In general, it was an innocuous sounding.

5.2.2 Soil moisture and sensitivity experiments

In the original API-derived soil moisture in grid 3, the values were too small and lacked horizontal heterogeneities (Fig. 5.5). Thus, we used the soil moisture derived from the API method for Case 980726 instead. Our purpose is to test the impact of soil moisture initialization, therefore it might be better to use more extreme set of values. We used the same methodology to alter the soil moisture and thus we kept the same names for the various sensitivity experiments (Table 4.3). Because grid 3's length was greater than its width, we rotated the grid 3 soil moisture in Case 980726 counterclockwise. As in Case 980726, we used the eta soil moisture for grids 1 and 2. Note that we have also used homogeneous SMI in grids 1 and 2 for Case 990802 and again found no significant impact on grid 3. The grid 3 soil moisture initialization for Case 990802 is displayed in Fig. 5.6.

5.3 Model Results

5.3.1 Grid 1

First, we examine how RAMS reproduced the large-scale features in grid 1 in order to gain some confidence in the performance of the model. For the sake of economizing space, we will only show results from exp. API (Fig. 5.7), as other experiments produced qualitatively similar results. At 03/0000, the RAMS sea-level pressure compared reasonably well with that of the RUC analysis, except for a few minor details. The sea-level low over the Texas/Oklahoma border was displaced about 100 km (2 grid points) to the northeast in exp. API. In the RUC analysis, the quasi-stationary front moved northeastward in the last 12-h. Also in the last 12-h, the cold front moved southward but the cold front's movement has retarded at this time and became a quasi-stationary front (Fig. 5.3a, 5.7a,b). RAMS placed the quasi-stationary front a bit too far north over the southeastern states. In addition,

the simulated trough axis over Kansas and Oklahoma did not extend into Texas as in the RUC analysis. At 850-hPa, RAMS captured the high-θ_e tongue, covering the southeastern states, Oklahoma and parts of Kansas. However, the details over the Western states were not well captured (Fig. 5.7c,d). The 400-hPa PV was reasonably well captured, especially the high/low PV couplet over Kansas, and no PV anomaly was upstream of the genesis region at this time. Although the results were acceptable in grid 1, RAMS did not perform as well in reproducing the large scale features in Case 990802 as in Case 980726 (Fig. 5.7e,f). Perhaps it was this reason that the simulated MCS did not perform as well either (shown later).

5.3.2 Grid 2

Figure 5.8 shows the model cloud top temperature for exp. API. Most of the other experiments (except for exp. HOM50 in which convection was delayed) produced similar results, so they are not shown for the sake of economizing space. At 02/2345, the cloud shield in exp. API did not correspond too well with observations, as the simulated systems were a bit too far to the west (Fig. 5.8a). The simulated convective systems corresponded to B_1 and B_2 in Fig. 5.1, but their sizes were different. B_3 and B_4 (Fig. 5.1e,f) were not simulated at all, probably due to the lack of a cloud-resolving grid over the area. Two hours later (03/0145), the two convective systems in western Oklahoma were close in proximity, and their cloud shields almost joined, similar to what occurred in the observations (Fig. 5.1g, 5.8b). However, the simulated systems were too small in size and located too far to the west. This could be due to the incorrect location of the simulated sea-level low over Oklahoma (Fig. 5.7a,b). Although the simulation was not perfect, this additional case might reveal whether the results in Chapter 4 can be generalized.

5.3.3 Pre-genesis phase: grid 3

Figure 5.9 shows the SLHF from the various experiments. As in Case 980726, the SLHF maxima corresponded quite well to the patterns of soil moisture anomalies. The magnitudes of the SLHF (on the order of several hundred Watts per square meter over the moist soil areas) were comparable to those in Case 980726. Unlike in Case 980726, the effect of S_3 on the SLHF was discernible in exps. API, API20, API40 and APIMOVES2. The low Bowen ratio corresponded to regions of low SSHF (Fig. 5.10) over the soil moisture anomalies, except in the northwest corner where low-level clouds shielded the surface from incident solar radiation (not shown). Areas of higher Bowen ratio corresponded to regions of drier soil. As expected, exp. HOM50 had low Bowen ratio (high SLHF) throughout most of the domain (Figs. 5.9, 5.10).

In exps. API, API20, API40, and API80, the soil moisture anomalies, S_1 and S_2, raised the dewpoint temperature (at the lowest σ_z-level) by about 2 ^{o}C as compared to exp. HOM31 (Fig. 5.11). However, the effects of S_3 and S_4 were less noticeable. In exp. API-HALF, due to the low values of soil moisture, the SRF was essentially zero for most of the domain in grid 3. Therefore, only S_2 had significant effect in raising the dewpoint temperature (by 1 ^{o}C at the lowest σ_z-level as compared to exp. HOM31). In exp. APIMOVES2, S_2 was displaced to suppress initial convection in grid 3, and the effect of S_2 in elevating dewpoint in its new location (the western boundary) can be readily seen. The high dewpoint in exp. HOM50 in the northern half and southeast portion of the domain was due to high local evapotranspiration.

The difference fields (using exp. HOM31 as a baseline) of sea-level pressure, horizontal wind vectors and vertical motion at the lowest σ_z-level, reveal perturbations of mesohighs and divergent wind field associated with the soil moisture anomalies, as well as

enhanced vertical motion around the periphery of the soil moisture anomalies. The aforementioned effects were especially prominent in in S_1 and S_2 (Fig. 5.12). The effect of S_3 was not noticeable in any of the experiments. As in Case 980726, S_2 had the most impact, followed by S_1. S_4 still had some noticeable effect until the soil moisture was smoothed to a cutoff wavelength of 80 km. In exp. APIHALF, only S_2 had any noticeable effect albeit much weaker. As expected, in exp. APIMOVES2, the mesohigh associated with S_2 was displaced. High local evapotranspiration in the southeast corner of exp. HOM50 created an anomalous mesohigh and enhanced downward motion in that area. In general, the mesohigh, divergent wind and vetical motion perturbations were on the order of 0.5 hPa, several meters per second and several centimeters per second, respectively. As revealed in a vertical cross section, similar to Case 980726, the cold pool generated by S_2 has a temperature contrast of 4 K with its surroundings and a depth of about 1 km (Fig. 5.13).

5.3.4 Genesis phase: grid 3

Convection was initiated shortly before 02/2100 in exp. API as a result of mesoscale pressure perturbations that developed within the sea-level low over Oklahoma, leading to low-level convergence. In addition, there was buildup of CAPE in the area due to surface heating. Multi-cellular cluster, C_1, was initiated near the Texas/western Oklahoma border. Convective cells, C_2 and C_3, formed to the east of C_1 in the periphery of S_2 (Fig. 5.14a). As shown later, the soil moisture anomaly S_2 affected the locations of C_2 and C_3 slightly. C_4 was initiated due to the collision of the PIMSs induced by S_2 and S_4. A weak area of precipitation (C_5) to the north of C_1 was also initiated at this time. Exps. API20 and API40 had qualitatively similar results as those in exp. API (Fig. 5.14a-c). However, C_4 did not appear in exp. API80 at this time due to the weakened PIMS from S_4. In addition, C_1 in exp. API80 was slightly shorter, and C_5 was more intense, due to a stronger PIMS from

S_2, leading to stronger vertical motion, thus more intense precipitation (Fig. 5.14d). It is interesting to note that the results in exp. APIHALF were qualitatively similar to those in exp. API even though the PIMSs in exp. APIHALF were much weaker (Fig. 5.14e). Exp. APIMOVES2 suppressed the initiation of C_1, but initiated two convective cells at its northern and southern extremities of S_2, respectively. The absence of the collison of the PIMSs from S_2 and S_4 resulted in C_4 not emerging at this time in exp. APIMOVES2 (Fig. 5.14f). Again, it appears that large-scale forcing played a major role in initiating convection since exp. HOM31 produced similar results as those in exp. API, except for the absence of C_4. However, the absence of S_2 in exp. HOM31 affected the positions of C_2 and C_3 slightly. Specifically, C_2 and C_3 were located slightly more northward in exp. HOM31 (Fig. 5.14g). Exp. HOM50 produced no convection at this time (Fig. 5.14h).

At 02/2200 in exp. API, C_1 weakened and would dissipate shortly. The cell southeast of C_1 was also short-lived (it would dissipate 45 min later). C_4 intensified in the last hour. A new cell, C_5, formed ahead of C_1 at this time. Another new cell, C_6, also formed in the southern extremities of the domain (Fig. 5.15). Although the results in exps. API20, API40, and API80 were qualitatively similar to those in exp. API, the counterparts of C_1, C_5 and the cell southeast of C_1 in exps. API20 and API80 were embedded within the 1 mm h^{-1} contour (except in exp. API40). C_4 in exp. API80 was more intense, due to the stronger PIMS from S_2 (Fig. 5.15a-d). Exp. APIHALF had qualitatively similar results as in exp. API except that a cell south of C_4 appeared in exp. APIHALF 15 minutes earlier than in exps. API, API20, API40, and API80 (Fig. 5.15a-e). C_6 also formed in exp. APIHALF, but it was located further westward than in exp. API. In exp. APIMOVES2, the results were similar to those in exp. API, except that the new location of S_2 suppressed convection at where it should happen, and displaced convection more to the east, at the periphery of S_2 (Fig. 5.15a,f). The results in exp. HOM31 were similar to those in exp. APIHALF (Fig. 5.15e,g). At this time, convection had still not started yet in exp. HOM50 (Fig. 5.15h).

At 02/2300, new convective cells appeared on the eastern flank of S_2 in exp. API. A multi-cellular complex developed in the southern part of the domain. Also, another multi-cellular complex developed in the northwest corner of the domain as well (Fig. 5.16a). Exps. API20 and API40 produced similar results as exp. API, but the convective cell on the western (northen part) flank of S_2 in exp. API40 was less intense as a result of a weaker PIMS from S_4 (Fig. 5.16a-c). In exp. API80, the convective cell on the western (northen part) flank of S_2 did not appear at all due to a weaker PIMS from S_4 (Fig. 5.16d). In exp. APIHALF, there were some major different results as compared to exp. API (Fig. 5.16a,e). For example, the multi-cellular complex in the northern part of the domain in exp. APIHALF was larger than that of exp. API and consisted of more convective cells. However, the multi-cellular complex in the southern part of the domain was not as well developed in exp. APIHALF. The results in exp. APIMOVES2 were a cross between exp. API (northern part of the domain) and exp. HOM31 (southern part of the domain) (Fig. 5.16a,f,g). Although there was a multi-cellular complex in the southern part of the domain in exp. HOM31, it was quite different than that of exp. API (Fig. 5.16a,g). As for exp. HOM50, convection finally started by this time, but different than the other experiments. In particular, just like exp. HOM50 in Case 9808726, convection was very localized and confined to a small region in the domain.

The wind shear and CAPE in Case 990802 were smaller than those of Case 980726, thus explaining convection being more disorganized in Case 990802. For example, in exp. API for Case 990802, the wind shear for the lowest 6-km and the CAPE at 02/1800 were 6.1 m s^{-1} and 940 J kg^{-1}, respectively, somewhat smaller than the corresponding values of Case 980726's exp. API at the same time (13.4 m s^{-1} and 1240 J kg^{-1}).

The grid 3 domain-averaged surface latent and sensible heat fluxes in Case 990802 were similar to those in Case 9808726 (Fig. 5.17a,b). The highest (lowest) grid 3 domain-averaged SLHF was in exp. HOM50 (APIHALF). Naturally, the highest (lowest) grid 3

domain-averaged SSHF was in exp. APIHALF (HOM50). The rest of the experiments fell somewhere in between. Exp. HOM31 had slightly lower (higher) domain-averaged SLHF (SSHF) than experiments with heterogeneous SMI (except for exp. APIHALF).

In terms of domain-averaged CAPE in grid 3, *the highest was in exp. HOM50* (due to the large evapotranspiration), reaching a maximum value close to 2200 J/kg. *The lowest CAPE was in exp. APIHALF*, reaching a maximum value close to 1200 J/kg. The remainder of the experiments fell between the two extremes, but they were closer to exp. APIHALF (Fig. 5.17c). A time series of the grid 1 temperature at the lowest σ_z-level at a point closest to S_2 shows that before 2100 UTC, 2 August, *exp. HOM50 had the lowest temperature.* On the other hand, experiments with drier soils at that point, i.e., exps. APIHALF, API-MOVES2, HOM31 had the highest temperatures within the same time window, with the rest of the experiments falling somewhere between these two extremes. Similar results hold for Case 980726 (Figs. 4.17c and 4.18).

The lowest grid 3 domain-averaged precipitation rate was in exp. HOM50 due to a delay in the onset of convection and in confined areas of the domain (Fig. 5.19a). Exp. APIMOVES2 reached its maximum precipitation rate later than most experiments but it had a higher maximum precipitation rate than all the other experiments. On the other hand, exps. APIHALF and HOM31 reached their maximum precipitation rates the soonest. Exps. API, API20, API40, and API80 had a similar precipitation rate trend, reaching a peak precipitation rate at the same time as exp. APIMOVES2, but at a lower value. In terms of accumulated precipitation, the lowest was in exp. HOM50 for reasons just explained, and the highest was in exp. HOM31, and the rest of the experiments were between these two ranges, but closer to exp. HOM31 (Fig. 5.19b). In particular, the 12-h precipitation accumulation for the heterogeneous SMI experiments had slightly lower values than exp. HOM31.

5.4 Discussion

To determine how well RAMS performed in terms of accumulated precipitation, we show the accumulated precipitation from exps. API, APIMOVES2, and HOM31 and compare the results with the 4-km precipitation data from the GCIP archive (Fig. 5.20). The position of the precipitation band at the southern part of the domain was captured better by exps. API and APIMOVES2 (i.e., experiments with heterogeneous SMI). Exp. HOM31 had placed that band in the southern part of the domain too far west. The reason is that the soil moisture anomaly S_1 suppressed convection over its area in exps. API and APIMOVES2 and favored convection at its periphery (to the east). However, the observed precipitation in the northeastern part of the domain was not captured well in any of the experiments. As in Case 980726, convection was suppressed over moist soil, but occurred preferentially around the peripheries of the wet soil moisture anomalies. The simulations in Case 990802 did not perform as well as those in Case 980726. In Case 990802, the simulated system was too small in size and too far to the west. At least in Case 980726, RAMS was able to reproduce a cloud shield of similar size, shape and location as compared to observations, even though the precipitation was not well simulated. Nevertheless, we can use this case to see the similarities and differences between Case 980726 and Case 990802.

We saw the same effect in Case 990802 when the soil moisture initialization was smoothed. First, *the PIMSs associated with the smaller soil moisture anomalies weakened or disappeared with smoothing of the SMI.* This can lead to an underestimation of convection initiated by the smaller soil moisture anomalies (e.g., S_4). Second, *the PIMSs associated with the larger soil moisture anomalies strengthened with the smoothing of the SMI* for the reasons mentioned in Chapter 4. The magnitudes in perturbations of sea-level pressure, horizontal wind, and vertical motion associated with the soil moisture anomalies in Case 990802 were similar in magnitude to those in Case 980726. In addition, the SLHF,

Bowen ratio and the elevation in dewpoint for the soil moisture anomalies in Case 990802 were similar also in magnitude to those in Case 980726.

Just as in Case 980726, convection in Case 990802 was suppressed over moist soil areas, and convection tended to occur on the periphery of the soil moisture anomalies. However, convection was more disorganized and short-lived in Case 990802, unlike in Case 980726 where convective cells were organized into a convective line. Much like Case 980726, relocating S_2 in exp. APIMOVES2 for Case 990802 suppressed convection over S_2, but favored convection around S_2's periphery (Fig. 5.14). Since the convective cells in Case 990802 were short-lived, they had less time in interacting with S_2 as in Case 980726. So, we did not see the convective cells tracking around S_2.

Case 990802 followed similar trends in the grid 3 domain-averaged time series in SLHF, SSHF, and CAPE as compared to Case 980726. Experiments with drier soil had lower (higher) SLHF (SSHF) and a higher surface temperature (Figs. 4.17, 4.18, 5.17, 5.18). Even though exp. HOM50 in Case 980726 and Case 990802 had a lower surface temperature over S_2, the higher SLHF contributed more in increasing the CAPE. This again supports Pielke (2001)'s contention that higher SLHF compensates for the lowering of the surface temperature in increasing the CAPE as in exp. HOM50, and not that of Pan et al. (1996). However, as in Case 980726, convection in exp. HOM50 for Case 990802 was delayed and had the least domain-averaged accumulated precipitation. Although wetter soil delayed convection, but the maximum upward motion was larger just before convection started for the wetter soil experiments. In exps. HOM50, API, and HOM31, the maximum upward motion at 700-hPa just before significant convection started was 6, 4.5, and 4 m s^{-1}, respectively. We also found similar trend in Case 980726.

Generally, Case 990802 had a similar pattern of grid 3 domain-averaged precipitation as Case 980726. Maximum precipitation rate occurred sooner over drier soil, while over

very moist soil (i.e., exp. HOM50) convection was delayed and exhibited lower domain-averaged precipitation in terms of instantaneous rate and accumulation, consistent with Case 980726. However, using S_2 to suppress convection as in exp. APIMOVES2, the results were quite different. In Case 980726, the effect of relocating S_2 resulted in reducing the overall precipitation (in terms of rate and accumulation), but in Case 990802, it actually increased the rate of precipitation (domain-average), but not the accumulation. Therefore, although large-scale forcing is of primary importance in providing the favorable environment for convection to develop, the distribution of the soil moisture has tremendous impact in determining the exact location in which convection initiates and develops.

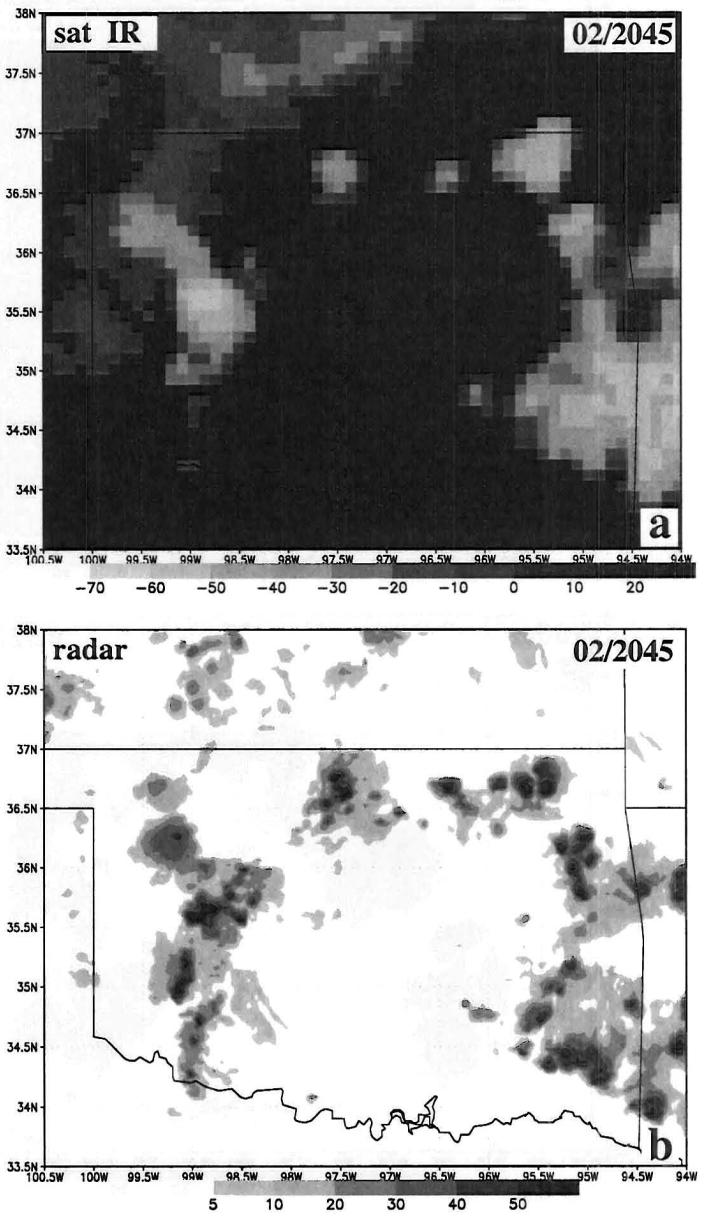

Figure 5.1 Satellite imagery from the NCEP/AWS Infrared Global Geostationary Composite provided by the Global Hydrology Resource Center: a) 2045 UTC, 2 August; c) 2215 UTC, 2 August; e) 2345 UTC, 2 August; g) 0145 UTC, 3 August; i) 0345 UTC, 3 August, 1999. Composite radar reflectivity (dBZ) from the National Weather Service, provided by the Global Hydrology Resource Center: b) 2045 UTC, 2 August; d) 2215 UTC, 2 August; f) 2345 UTC, 2 August; h) 0145 UTC, 3 August; j) 0345 UTC, 3 August, 1999.

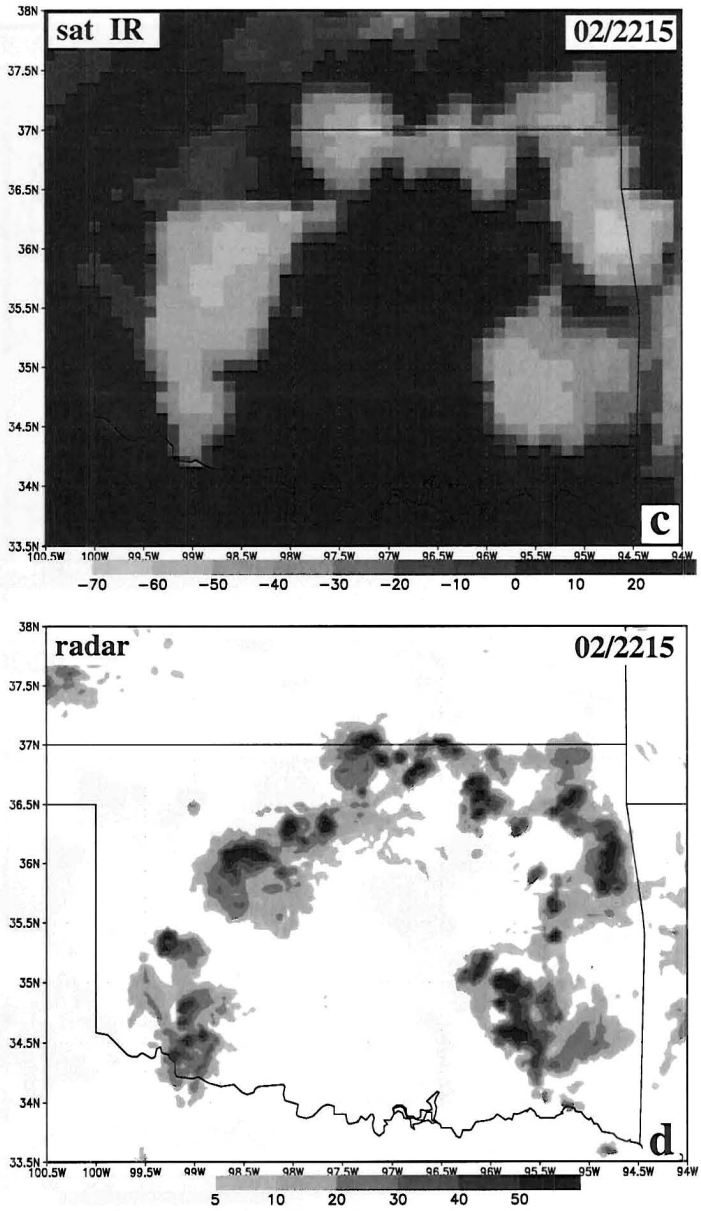

Figure 5.1 Continued.

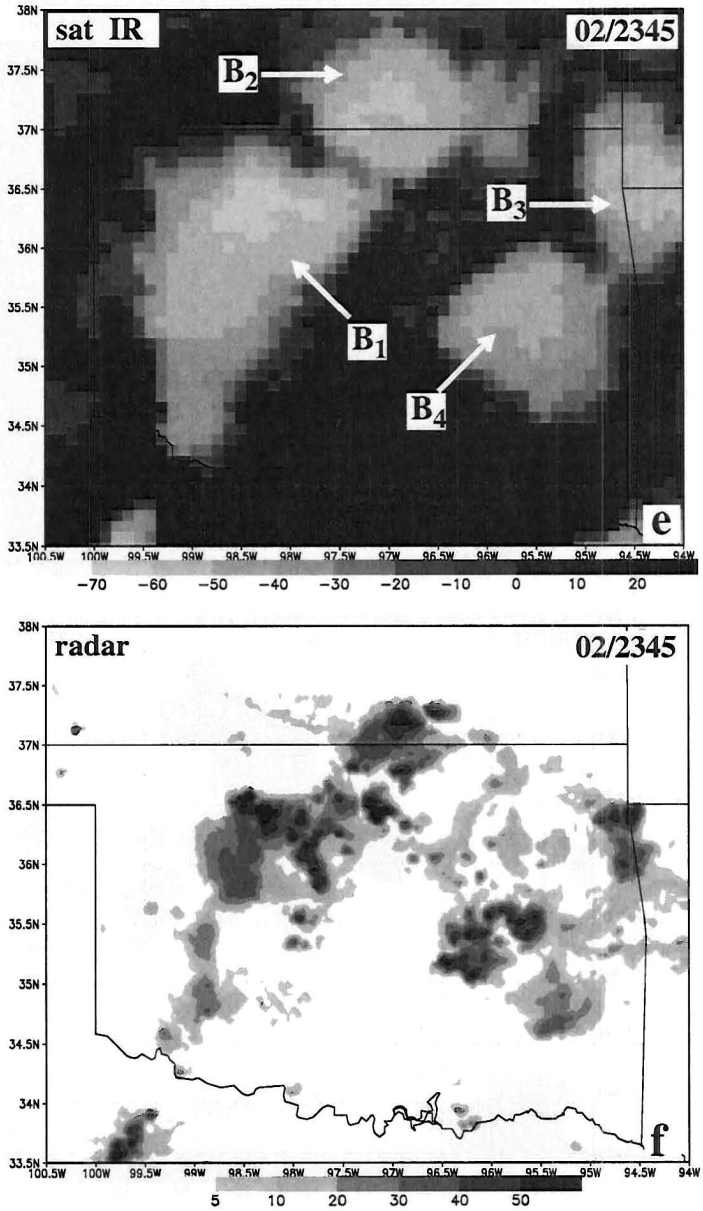

Figure 5.1 Continued.

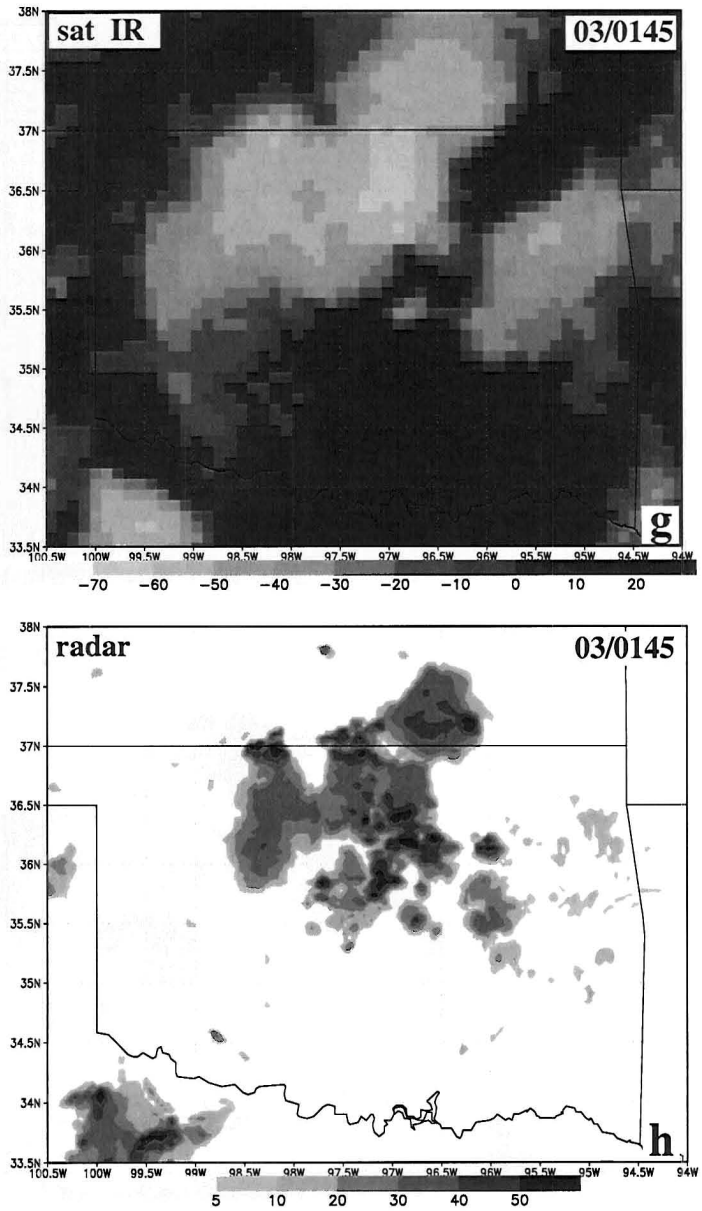

Figure 5.1 Continued.

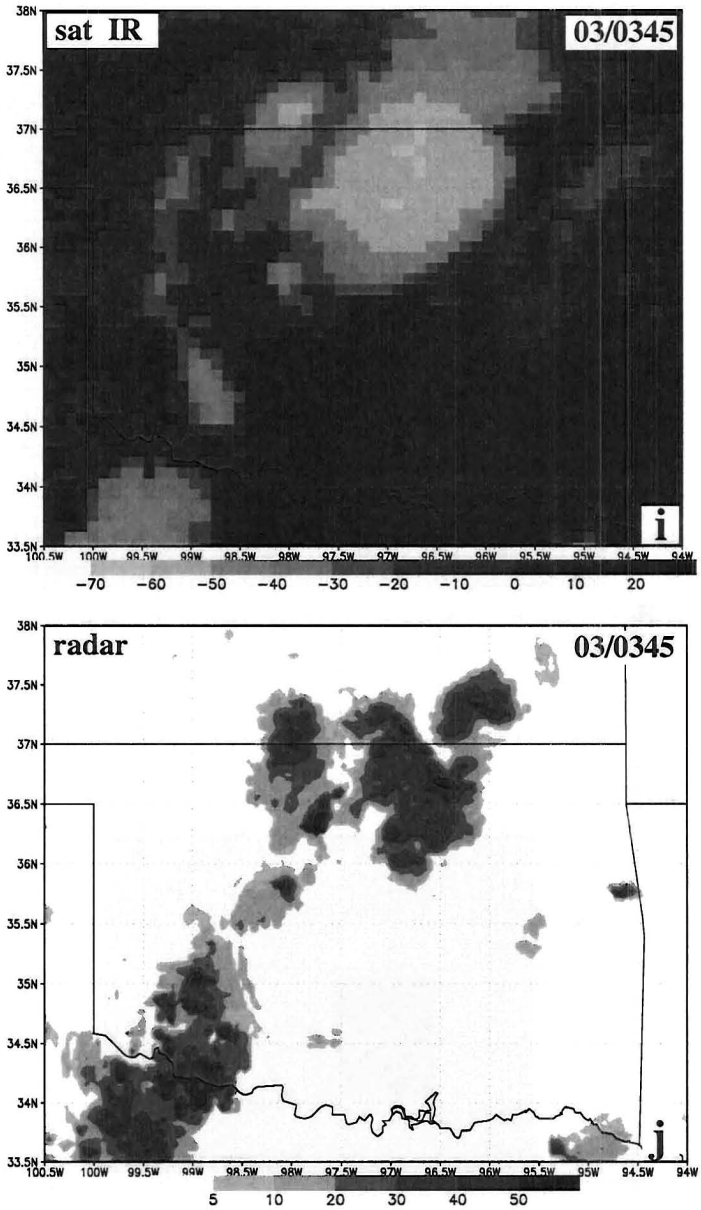

Figure 5.1 Continued.

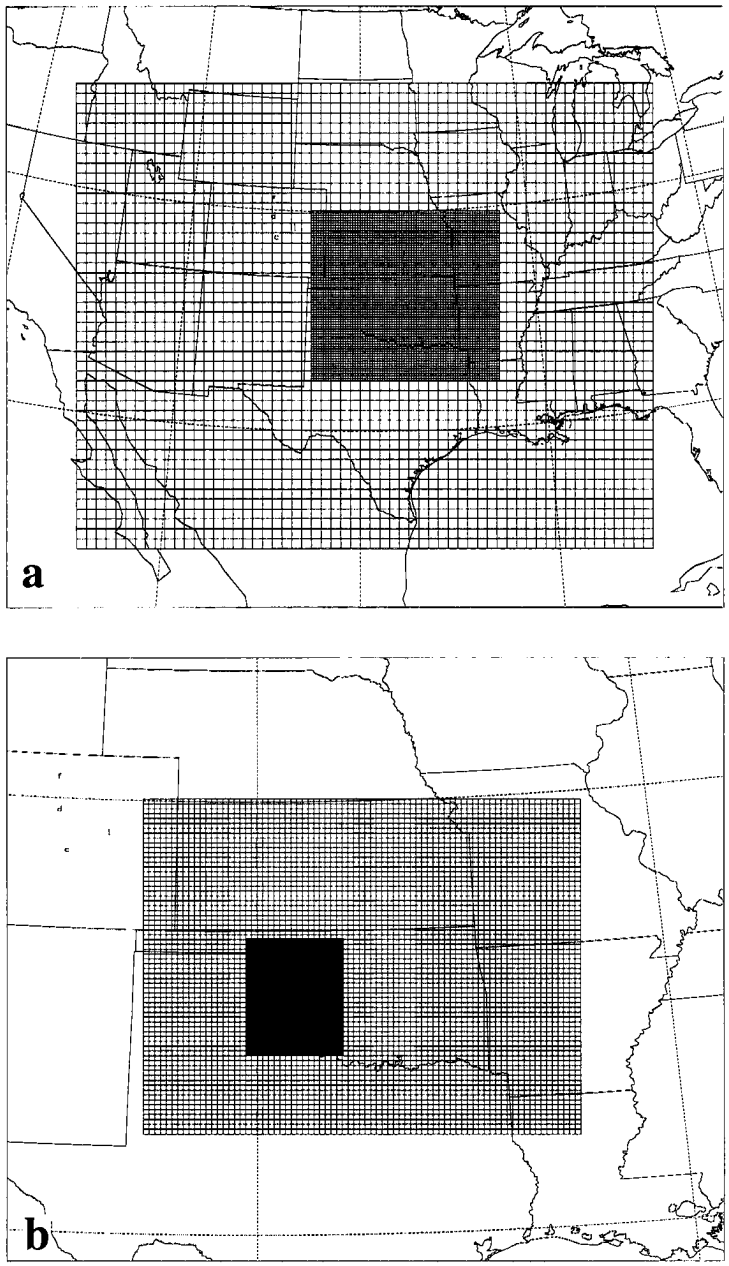

Figure 5.2 a) Nested grid setup for Case 990802 in RAMS with grids 1 and 2; b) nested grid setup in RAMS for Case 990802 with grids 2 and 3.

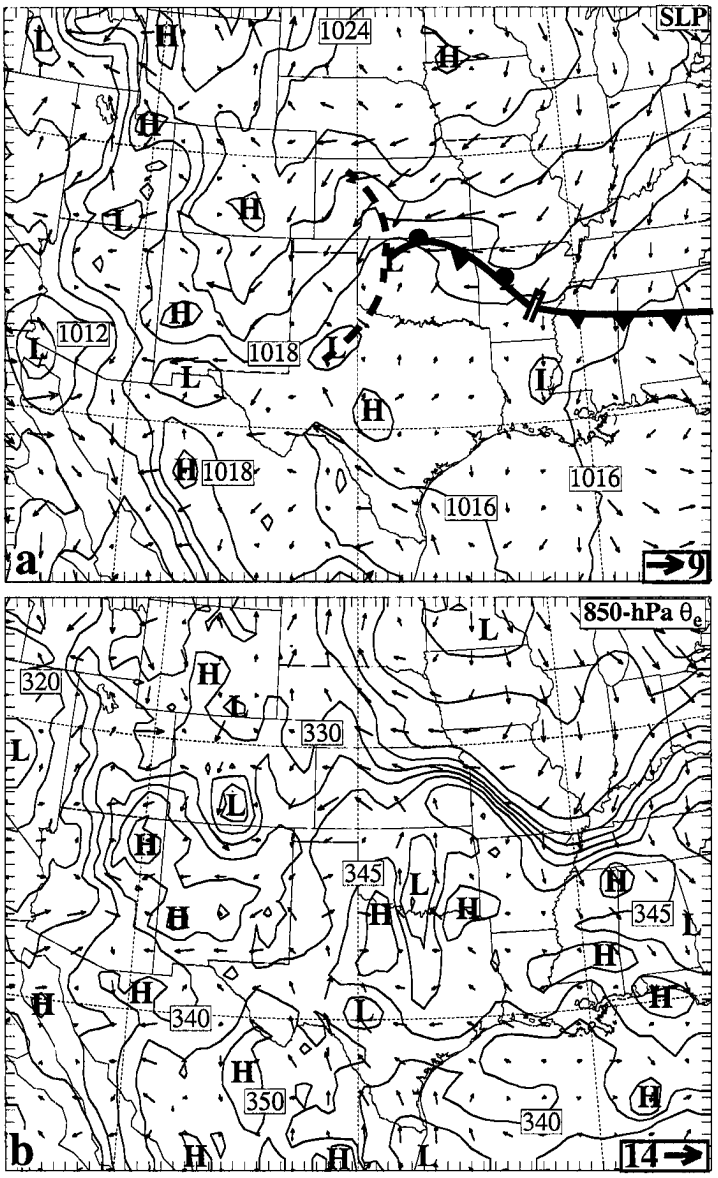

Figure 5.3 From the RUC analysis interpolated to RAMS grid 1 for Case 990802 at 02/1200: a) sea-level pressure (contour intervals of 2 hPa) superposed with wind vectors at the lowest σ_z level; b) 850-hPa equivalent potential temperature (contour intervals of 5 K) superposed with 850-hPa wind vectors; c) 400-hPa potential vorticity (with contour intervals of 0.25 PVU) superposed with 400-hPa wind vectors. Insets represent the scale of the wind vectors in m s^{-1}.

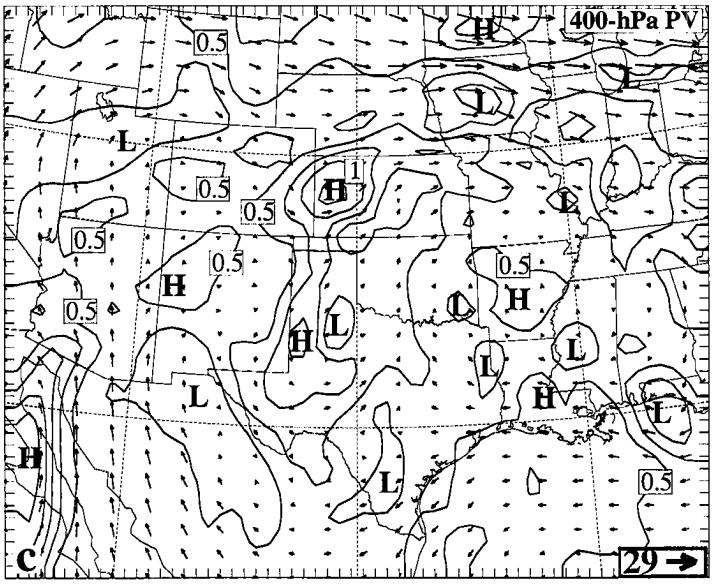

Figure 5.3 Continued.

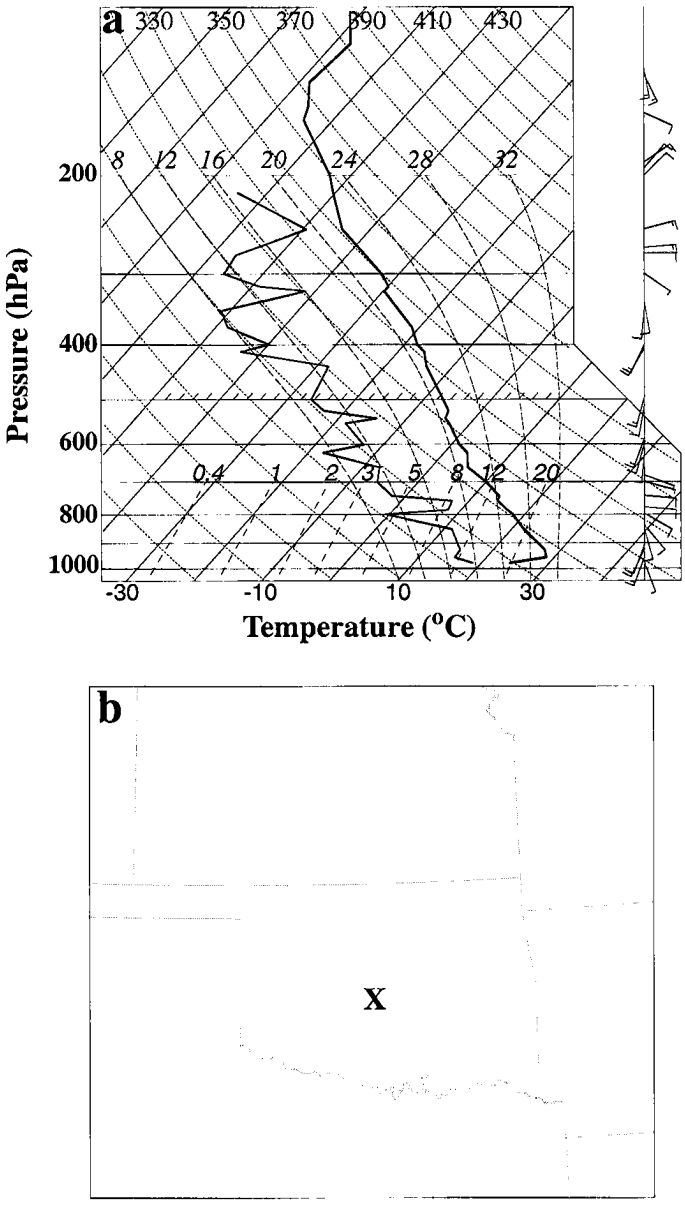

Figure 5.4 a) Skew T-log p diagram for temperature (°C), dew point temperature (°C), and wind (m s^{-1}) at 1200 UTC, 02 August 1999 at Oklahoma City, Oklahoma. A full (half) barb is 5 (2.5) m s^{-1}. Data was obtained at NCAR mass storage. b) Map indicating the location ('X') where sounding in (a) was taken.

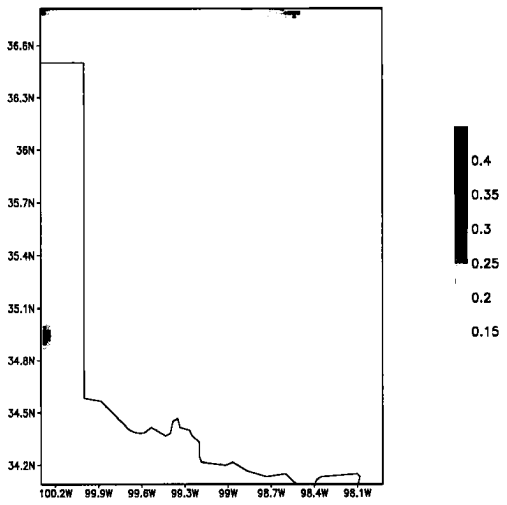

Figure 5.5 Volumetric soil moisture (m^3 m^{-3}) derived from the API method for 1200 UTC, 2 August, 1999. This particular soil moisture was not used due to the small value of soil moisture and lack of heterogeneities.

Figure 5.6 Initial volumetric soil moisture ($m^3\ m^{-3}$) in grid 3 for exp. a) API; b) API20; c) API40; d) API80; e) APIHALF; f) APIMOVES2 for Case 990802. These fields were taken from Case 980726 but rotated counterclockwise.

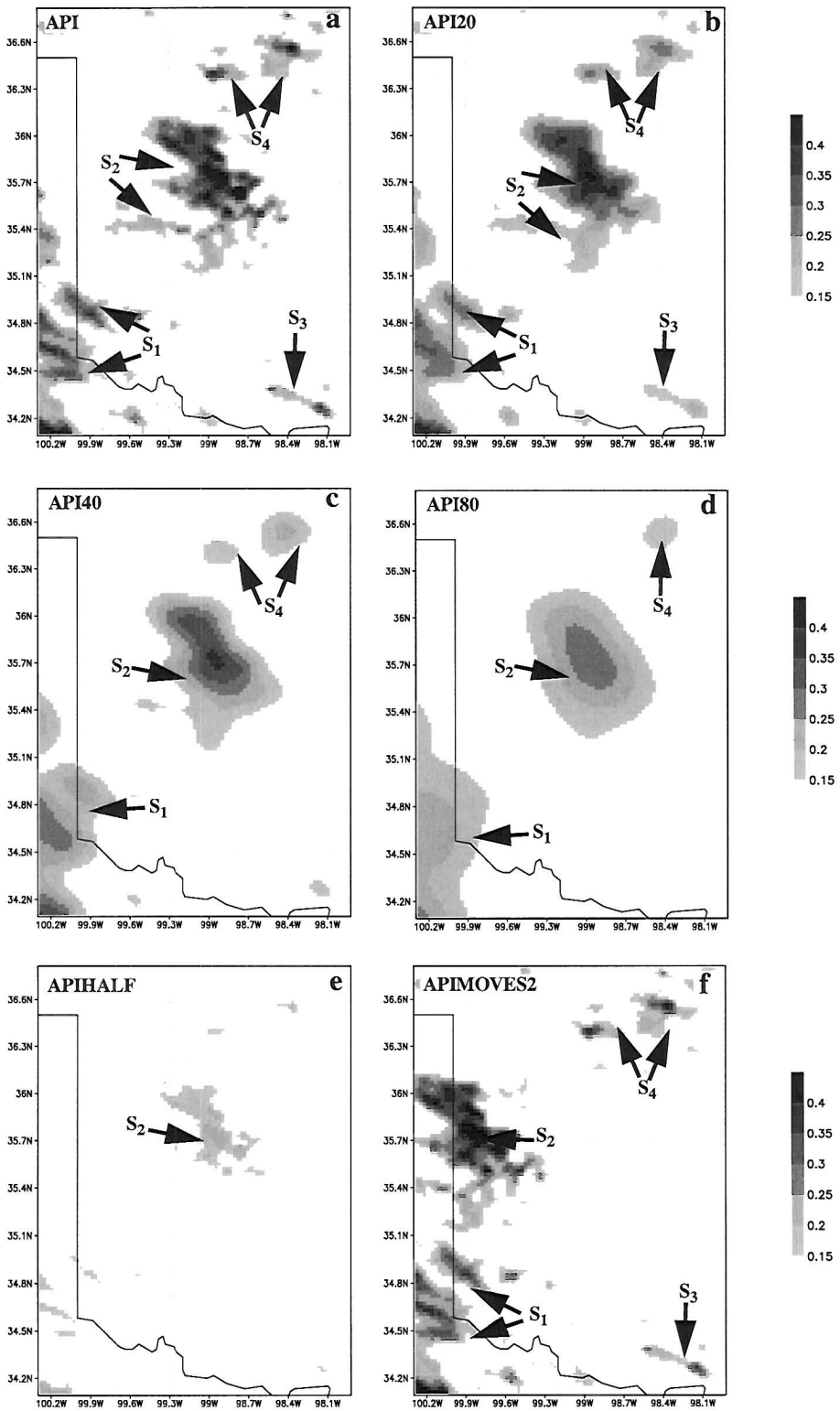
API
a
API20
b
API40
c
API80
d
APIHALF
e
APIMOVES2
f
S1
S2
S3
S4
36.6N
36.3N
36N
35.7N
35.4N
35.1N
34.8N
34.5N
34.2N
100.2W
99.9W
99.6W
99.3W
99W
98.7W
98.4W
98.1W
0.4
0.35
0.3
0.25
0.2
0.15

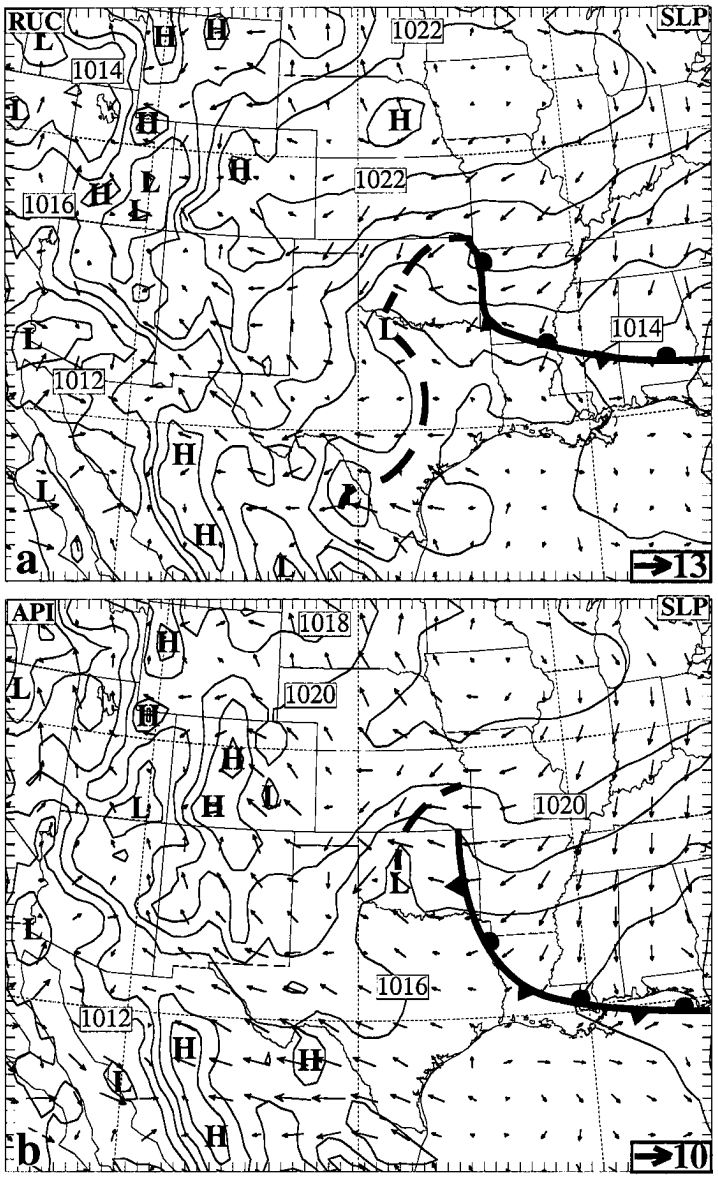

Figure 5.7 a), c), and e) are the same as Fig. 5.3a, b, c, respectively but at 03/0000. b), d), and f) are the same as Fig. 5.3a, b, c, respectively, but for exp. API in Case 990802 at 03/0000 in grid 1.

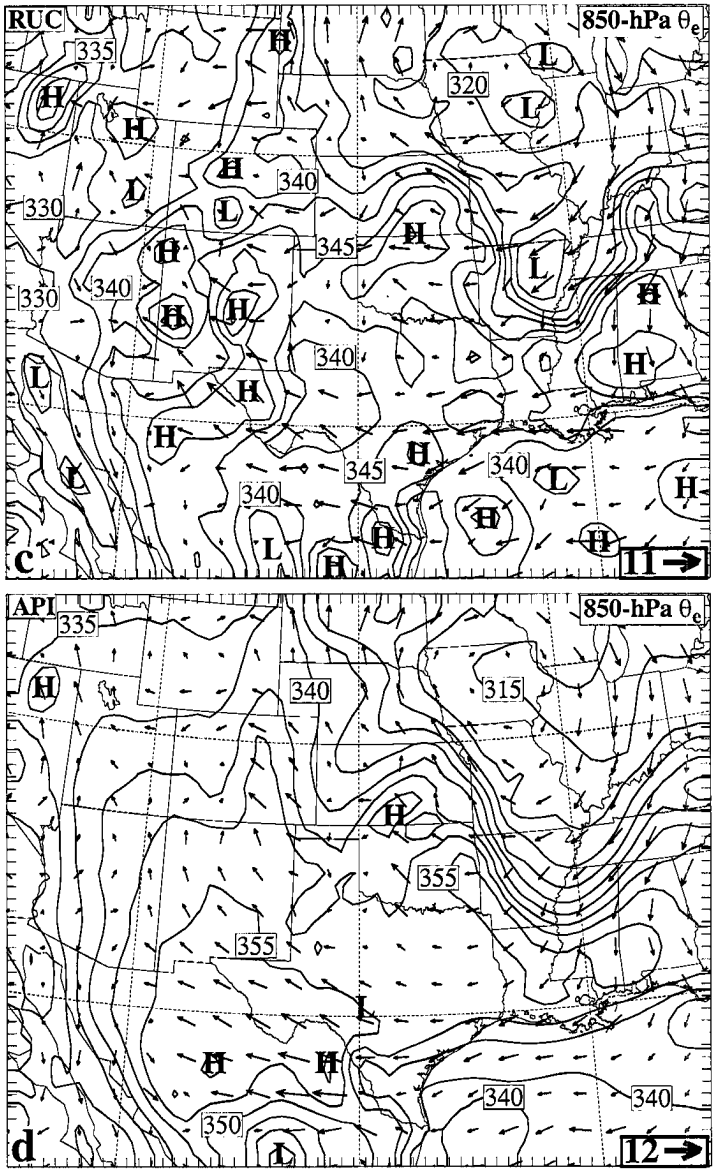

Figure 5.7 Continued.

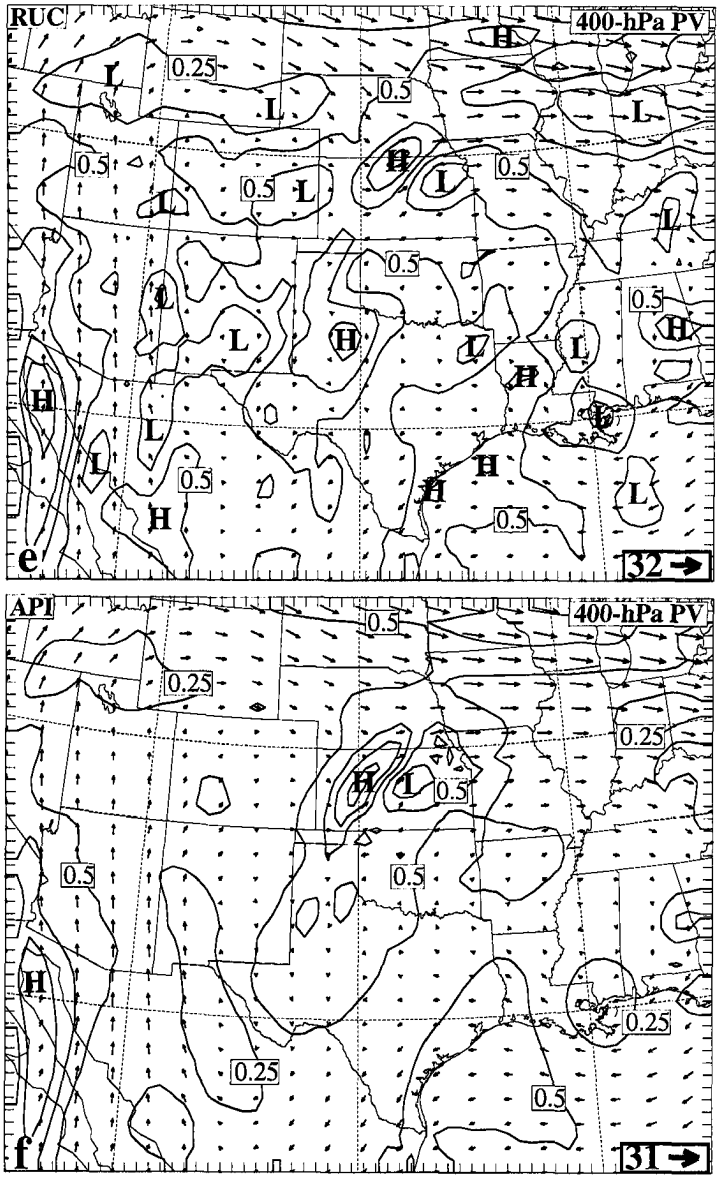

Figure 5.7 Continued.

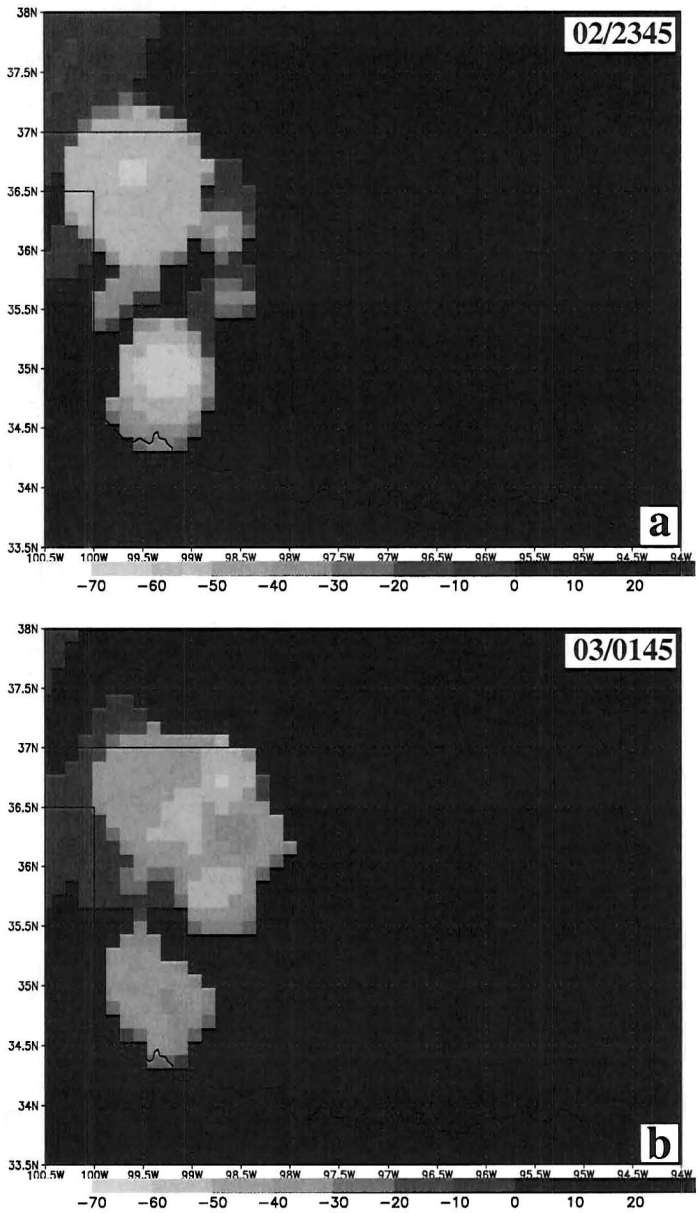

Figure 5.8 Case 990802 cloud top temperature in grid 2 for exp. API at a) 02/2345; b) 03/0145 for exp. API.

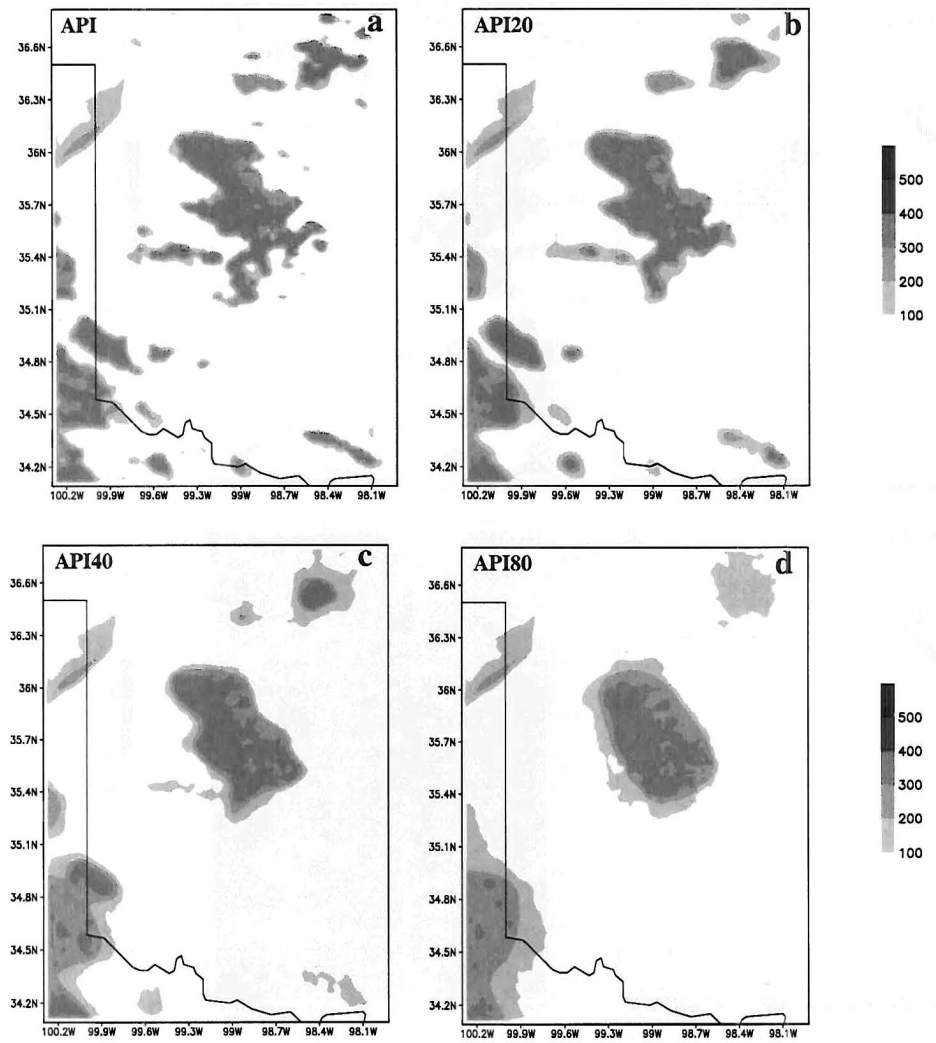

Figure 5.9 RAMS grid 3 surface latent heat flux (W m^{-2}) in Case 990802 at 02/1600 for exp. a) API; b) API20; c) API40; d) API80; e) APIHALF; f) APIMOVES2; g) HOM31; h) HOM50.

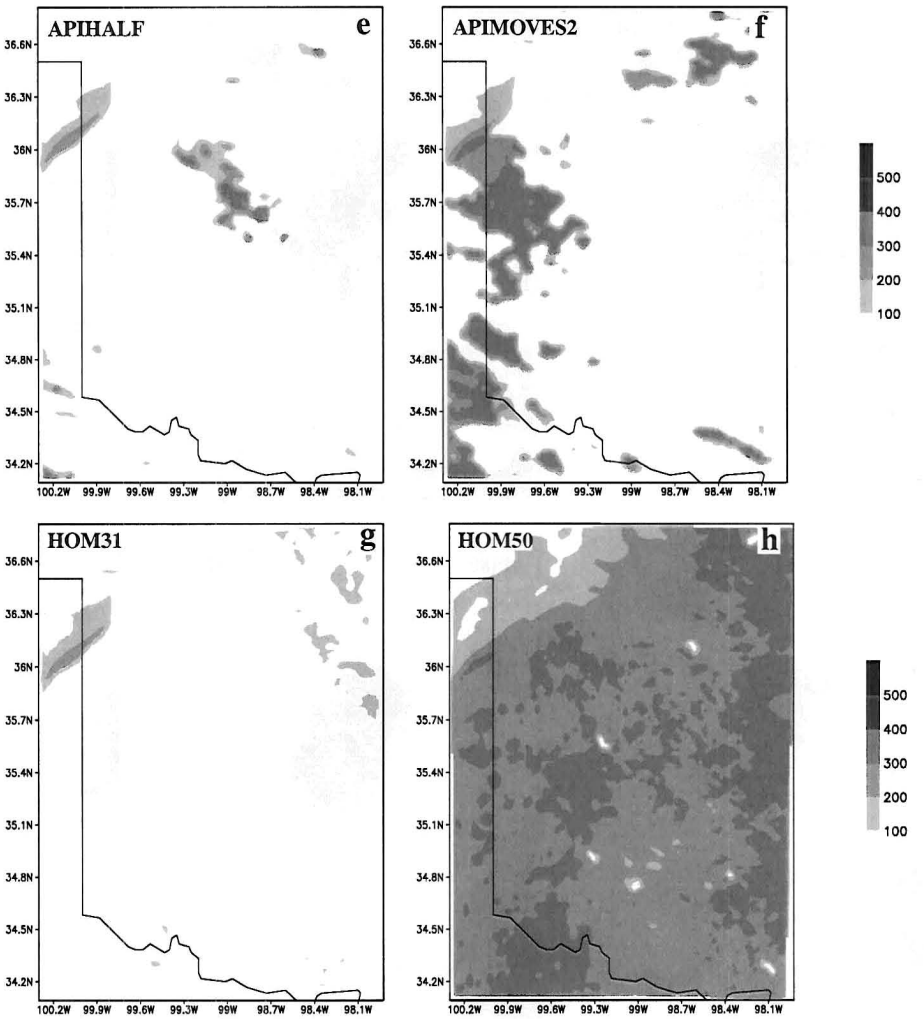

Figure 5.9 Continued.

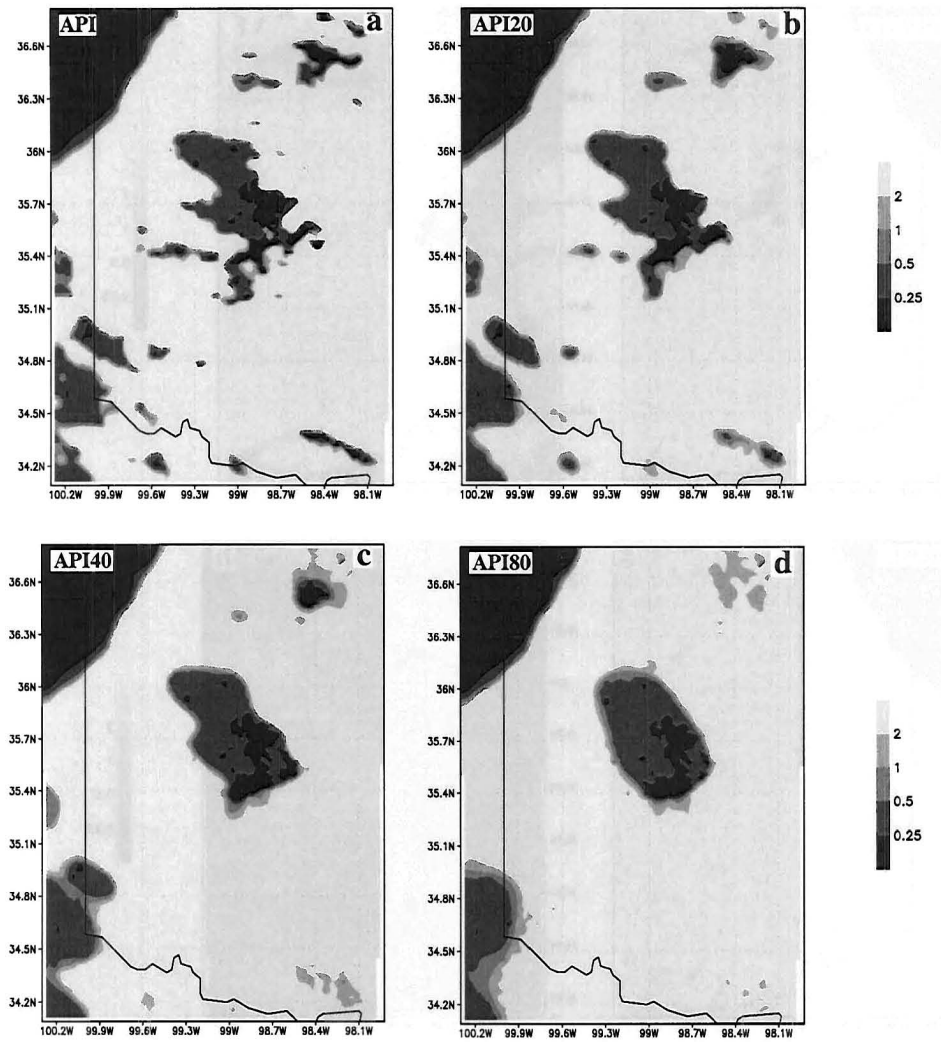

Figure 5.10 RAMS grid 3 Bowen ratio (SSHF divided by SLHF) in Case 990802 at 02/1600 for exp. a) API; b) API20; c) API40; d) API80; e) APIHALF; f) APIMOVES2; g) HOM31; h) HOM50.

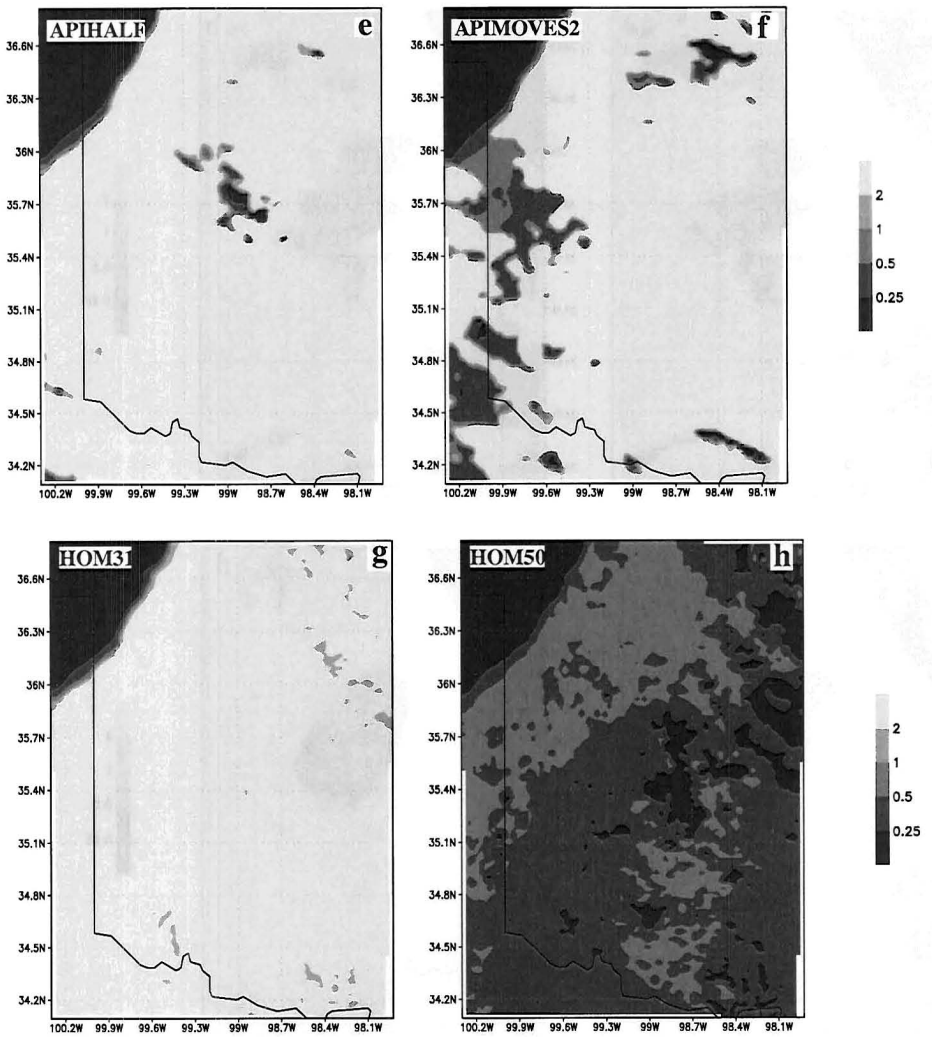

Figure 5.10 Continued.

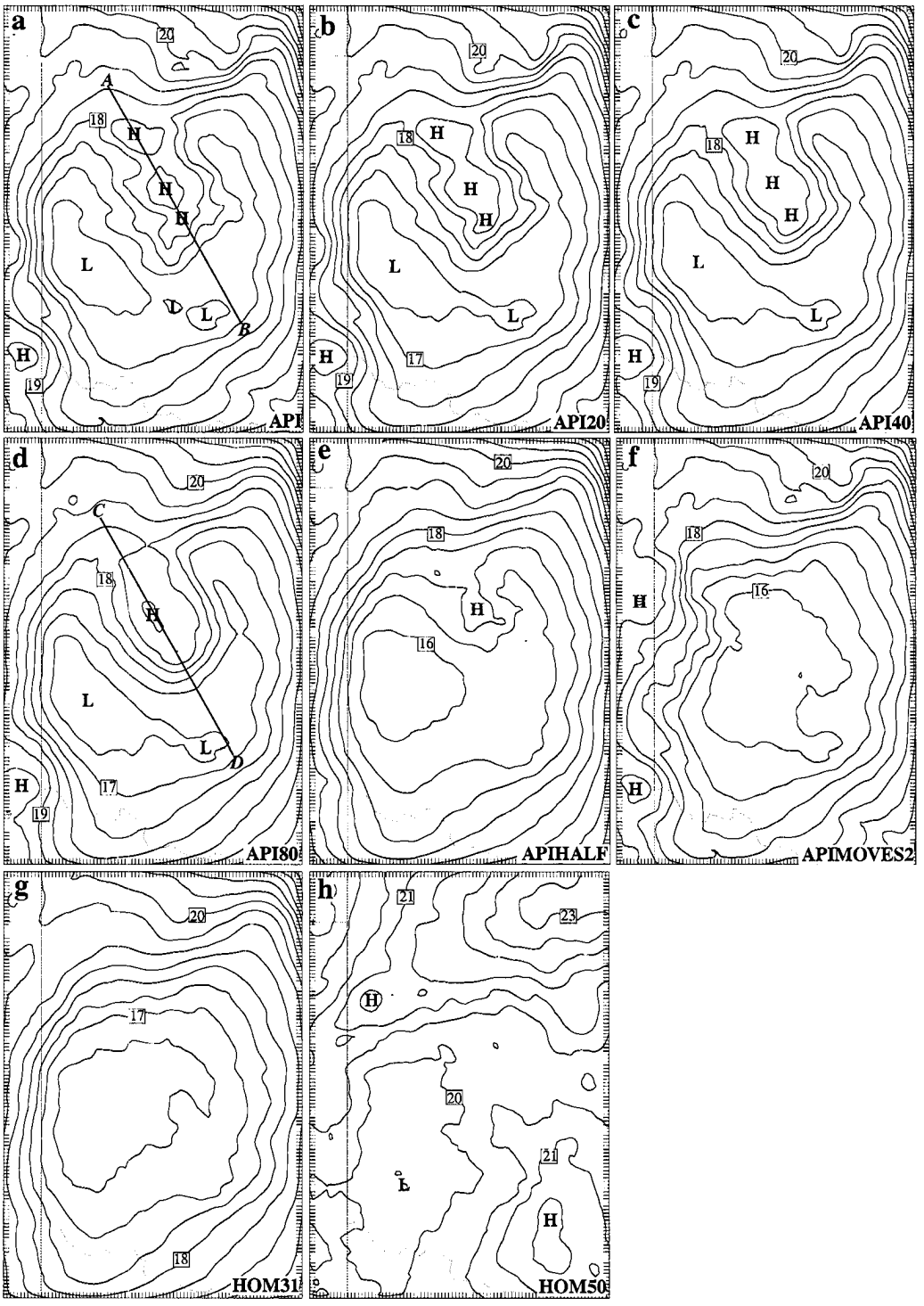

Figure 5.11 RAMS grid 3 dew point temperature at the lowest σ_z level above ground (at contour intervals of 0.5° C) in Case 990802 at 02/1800 for exp. a) API; b) API20; c) API40; d) API80; e) APIHALF; f) APIMOVES2; g) HOM31; h) HOM50.

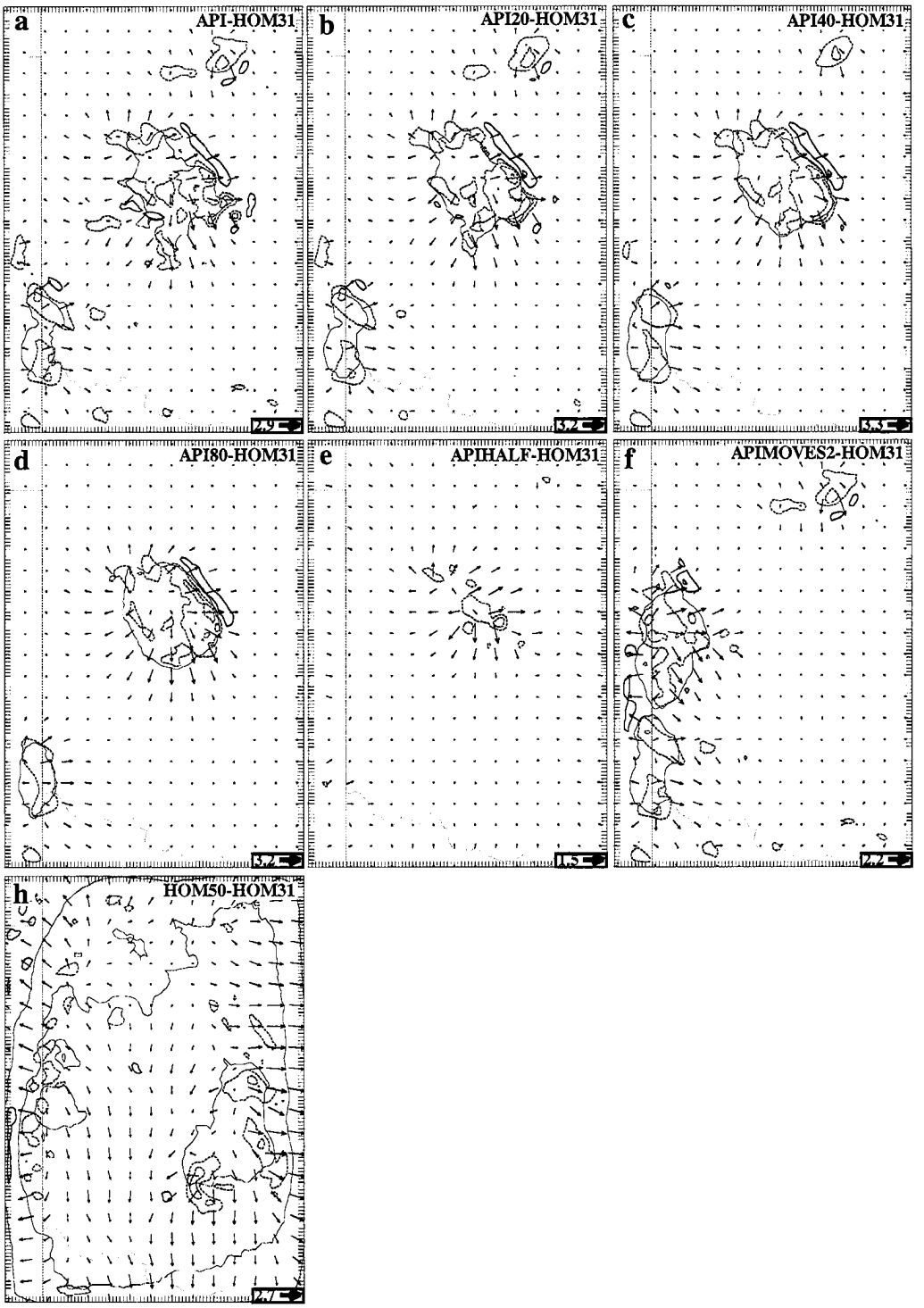

Figure 5.12 Same as Fig. 4.11 but for Case 990802 at 02/1800.

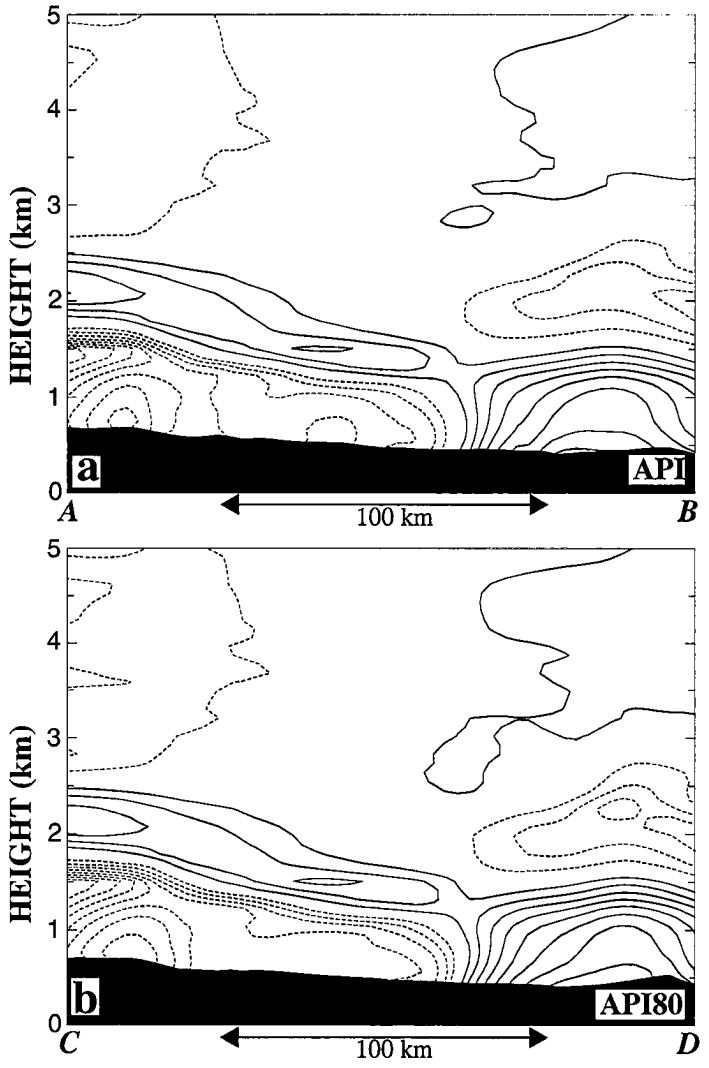

Figure 5.13 a) Vertical cross section of horizontal temperature deviation (at contour intervals of 0.25 K) taken through lines in Fig. 5.11 for expts. a) API; b) API80 at 02/1800 in Case 990802. Zero-contour is suppressed, and solid (dashed) contours represent positive (negative) values.

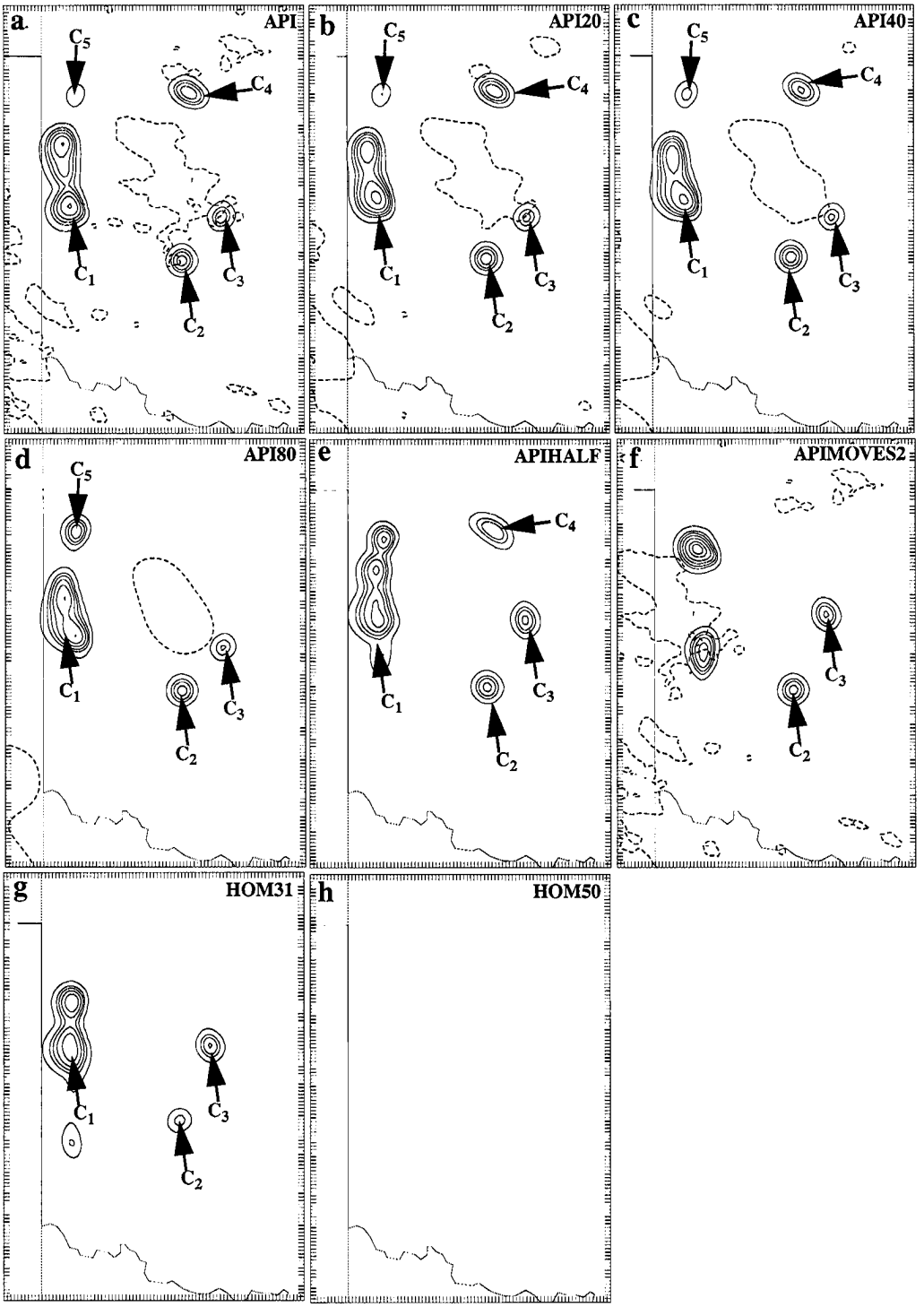

Figure 5.14 RAMS grid 3 precipitation rate (at contour intervals of 1, 5, 10, 20 , 40, 80 and 120 mm h^{-1} at 02/2100 in Case 990802 for exp. a) API; b) API20; c) API40; d) API80; e) APIHALF; f) APIMOVES2; g) HOM31; h) HOM50. Dashed contour represents initial volumetric soil moisture at 50% saturation.

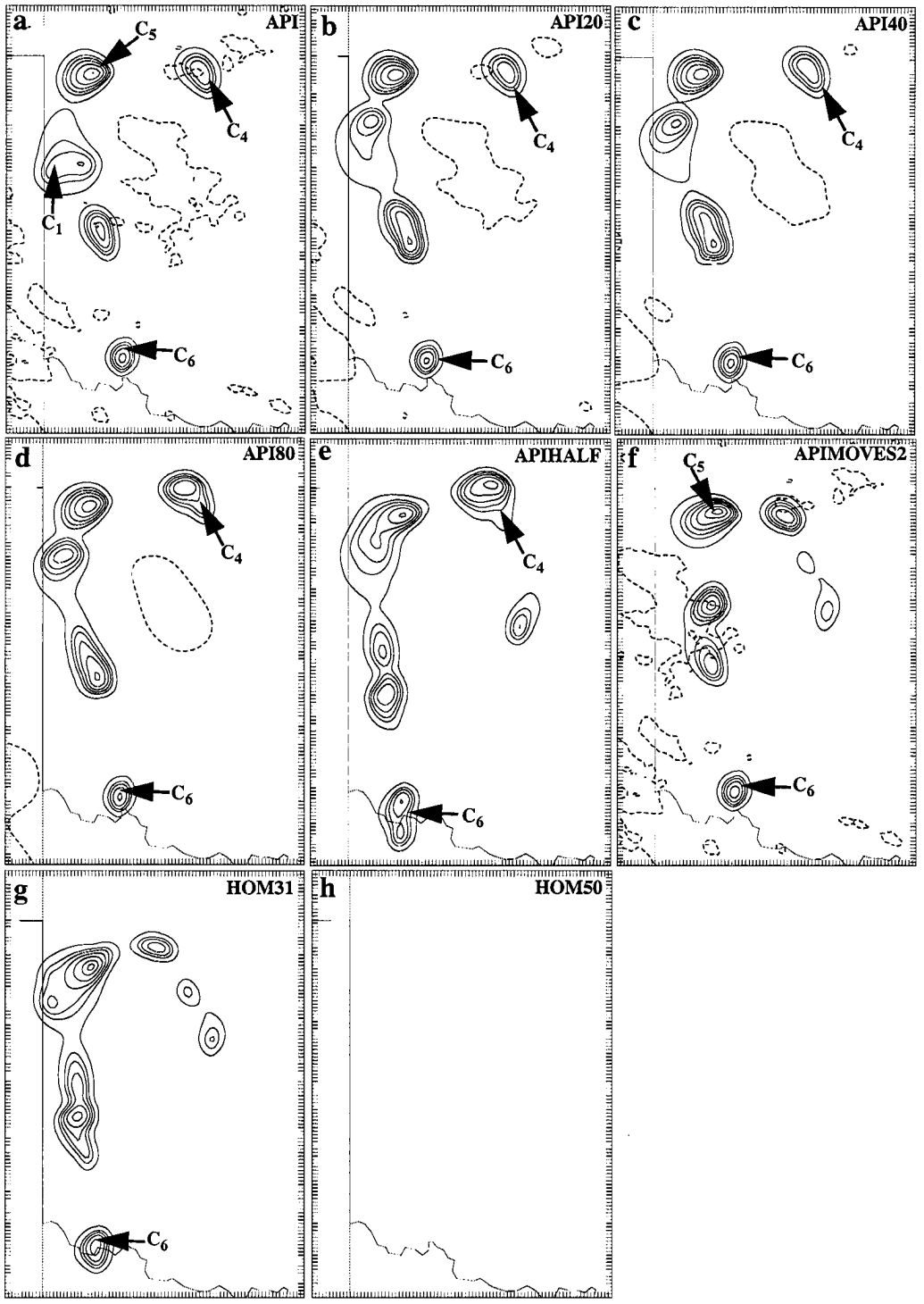

Figure 5.15 Same as Fig. 5.14 but at 02/2200.

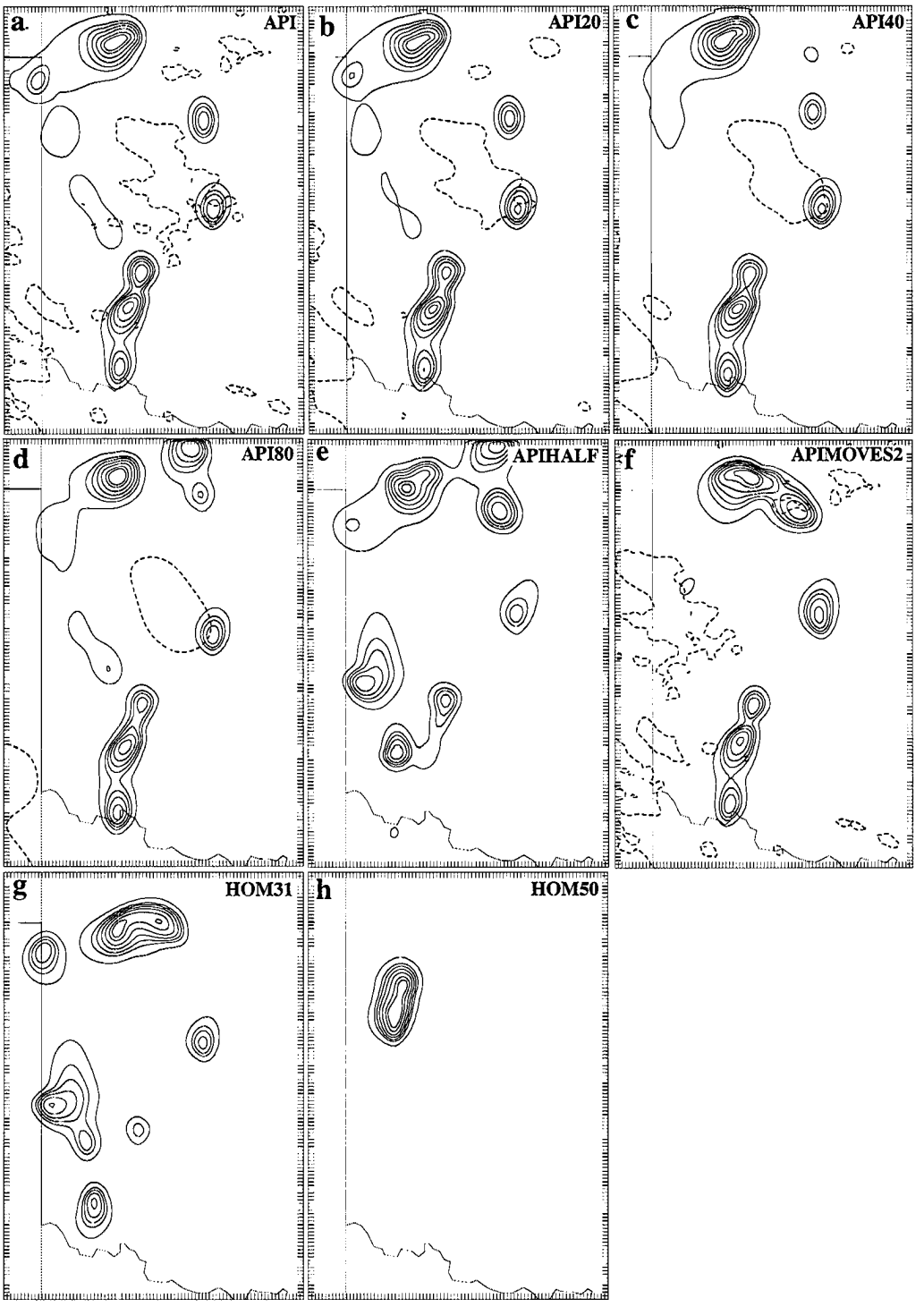

Figure 5.16 Same as Fig. 5.14 but at 02/2300.

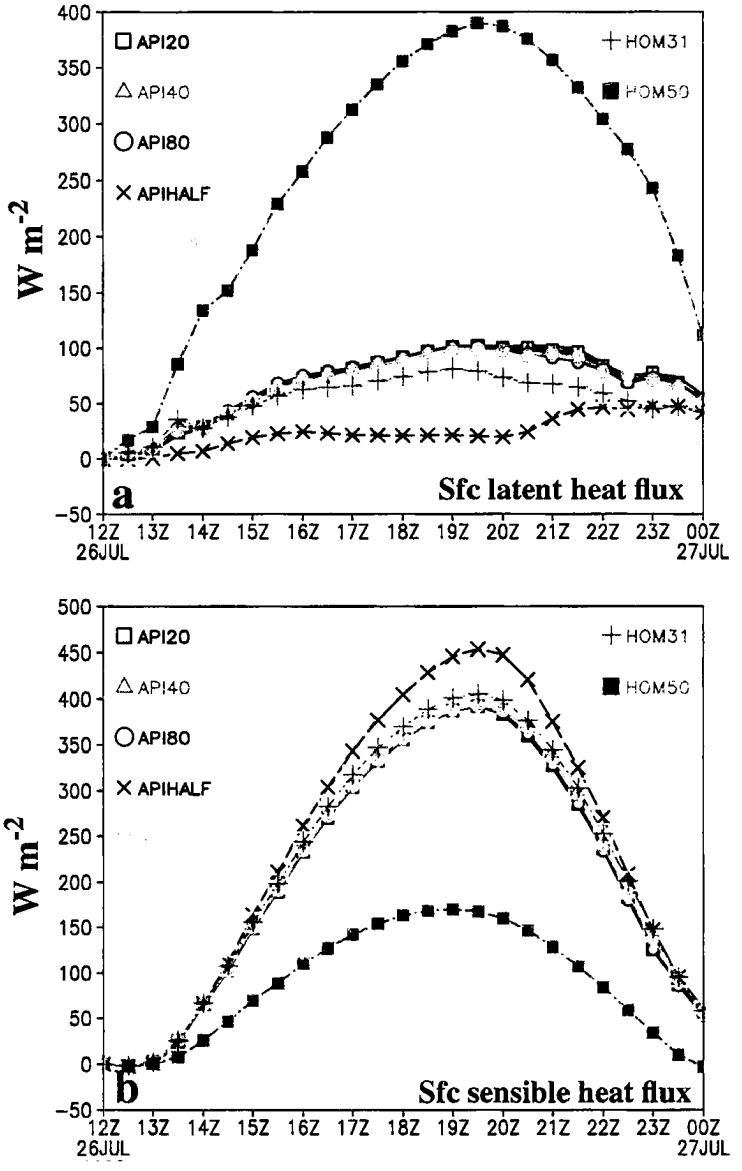

Figure 5.17 Time series of grid 3 domain-averaged a) surface latent heat flux (W m^{-2}); b) surface sensible heat flux (W m^{-2}); c) convective available potential energy (CAPE, J kg^{-1}) in Case 990802. Exp. API is represented by the solid curve. Symbols for the other experiments are indicated in the figure.

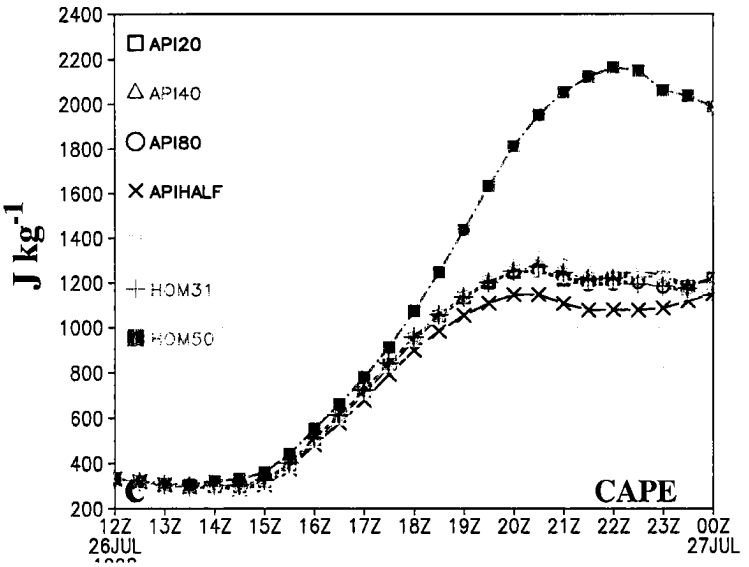

Figure 5.17 Continued.

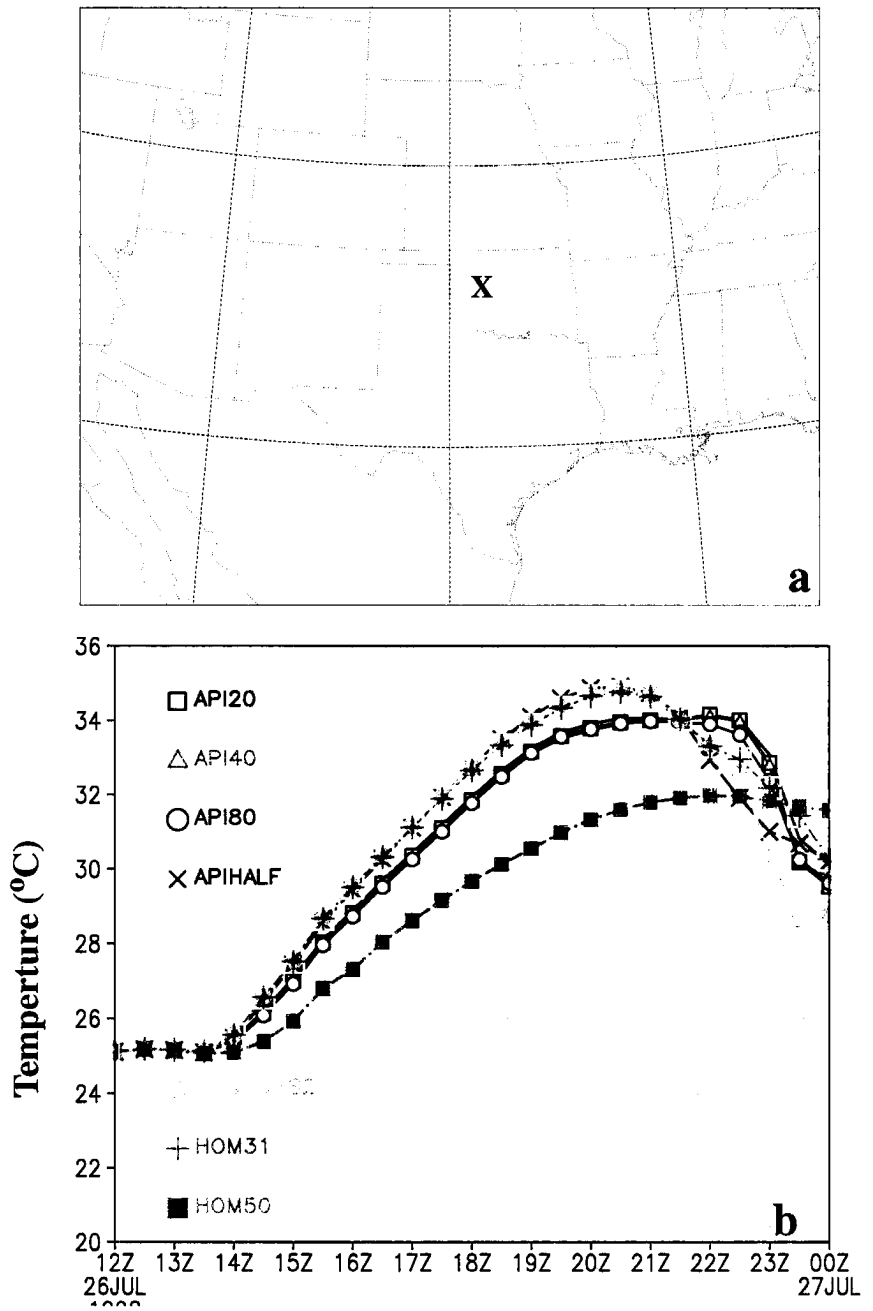

Figure 5.18 a) Grid 1 for Case 990802; b) time series of temperature (°C) at the lowest σ_z-level in grid 1 for the various experiments in Case 990802 over the location marked 'X' in (a). Solid curve in (a) is for exp. API, and the symbols for the other experiments are indicated in the legend.

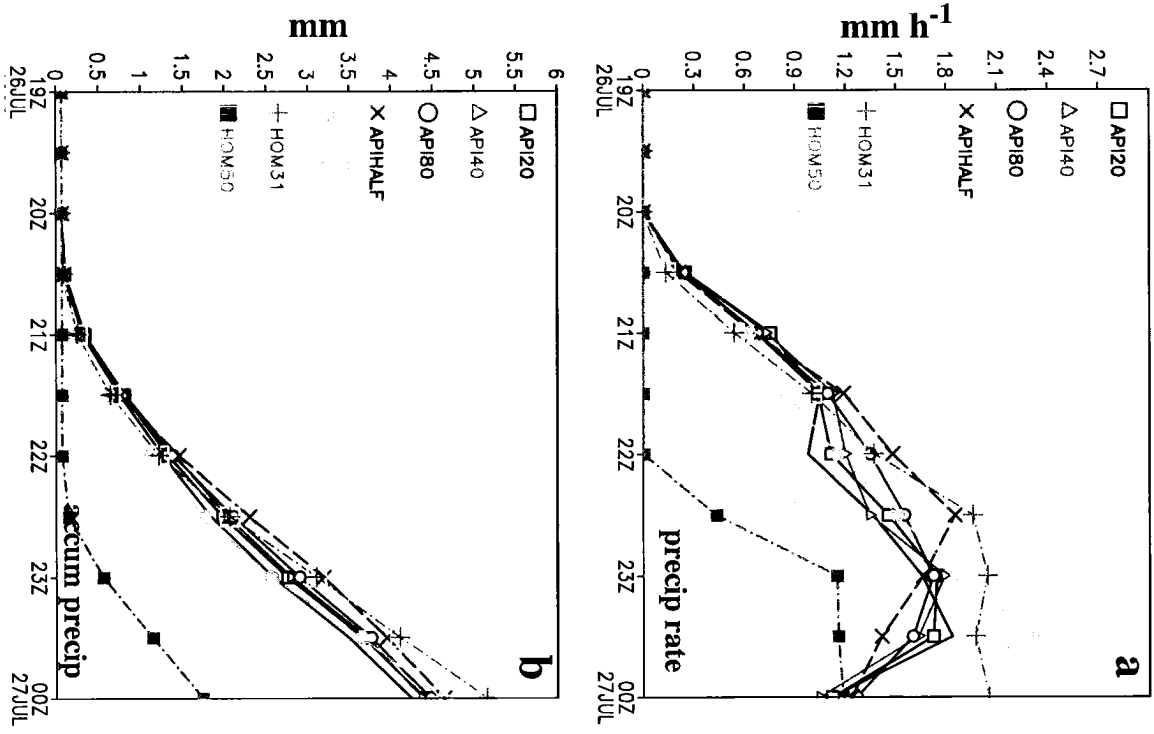

Figure 5.19 Time series of grid 3 domain-averaged a) precipitation rate (mm h^{-1}); b) accumu precipitation (mm) in Case 990802. Exp. API is represented by the solid curve. Sym for the other experiments are indicated in the figure.

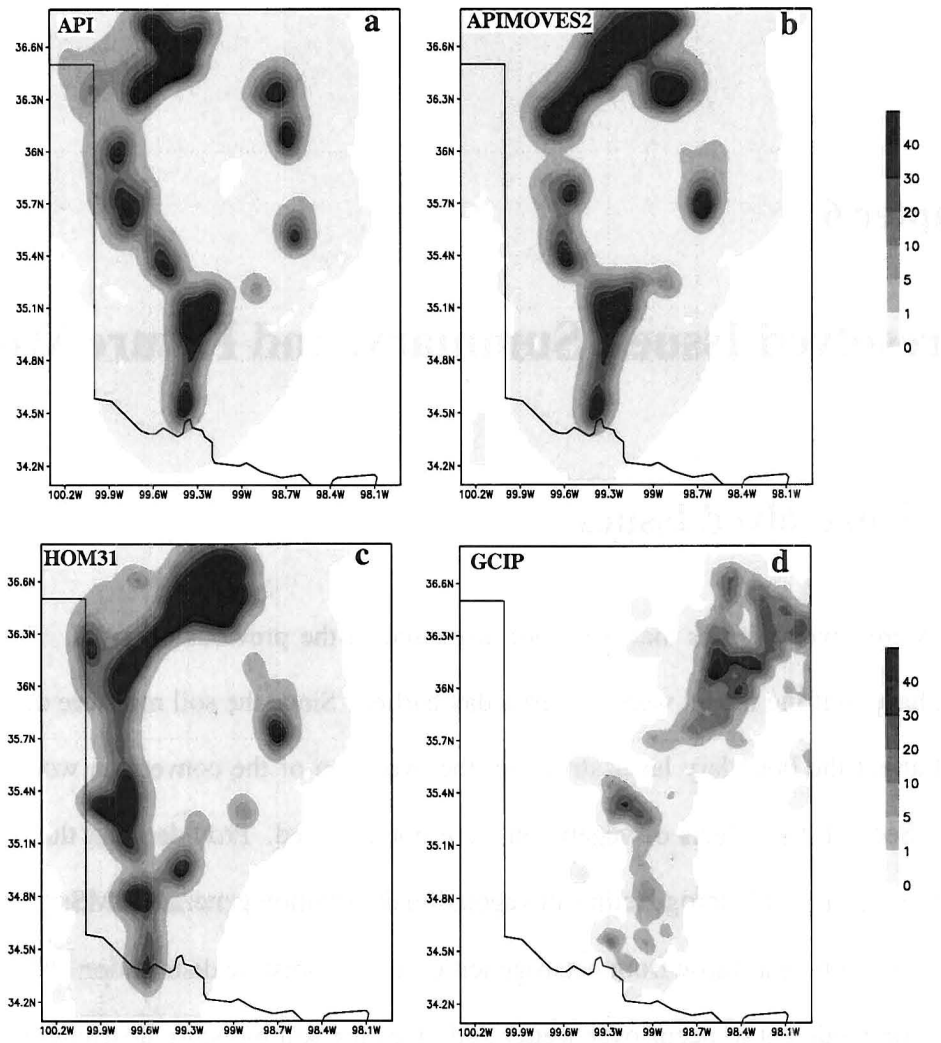

Figure 5.20 3-h accumulated precipitation (mm) from 02/2100 to 03/0000 in Case 990802 for a) exp. API in grid 3; b) exp. APIMOVES2 in grid 3; c) exp. HOM31 in grid 3; b) 4-km GCIP precipitation database.

Chapter 6

Unresolved Issues, Summary, and Future Work

6.1 Unresolved Issues

There were several issues that were not discussed in the previous chapters. First, what would happen if the model were to start a day earlier? Since the soil moisture distribution would affect the boundary layer structure, the evolution of the convection would be different. Second, the effects of vegetation were not explored. Provided that the plants are not stressed, can the heterogeneities in vegetation distribution generate PIMSs to the same order of magnitude as those from heterogeneities in soil moisture distribution? Third, since convection tends not to occur over wetter soil, does the soil moisture distribution become homogenized and the soil moisture gradient become reduced over time?

6.1.1 Starting the model one day earlier

To test the effects of starting the model one day earlier, we chose Case 980726. We initialized the model with NCEP analysis on 1200 UTC, 25 July 1998, and used the same model physics, soil moisture initialization and LAI as in exp. API (Case 980726). We named this experiment as exp. API-24h. Precipitation between 25/1200 and 26/1200 altered the soil moisture distribution, especially in the northwestern part of the domain and west of S_2. Nevertheless, larger soil moisture anomalies (i.e., S_1 and S_2) can still be identified (Fig.

6.1 and 4.5a). At 26/1200, a comparison of the sounding at a point over S_2 between exps. API and API-24h reveals that the surface air temperature in exp. API-24h was almost 4 ^{o}C colder than that in exp. API (21.9 versus 25.7 ^{o}C, Fig. 6.2). This is not surprising since S_2 has an extra 24 h to act in exp. API-24h to cool the surface. In addition, there was a shallow inversion layer at the surface in exp. API-24h which was absent in exp. API.

As a result of the altered soil moisture distribution, the SLHF in exp. API-24h was different from that of exp. API at 26/1600 (Figs. 4.5a, 4.8a, 6.1, and 6.3). So, exp. API-24h had more areas of high SLHF (thus more areas of cooler surface). therefore, convection was less likely to develop. In fact, convection did not develop at the corresponding times as in exp. API (Figs. 4.13a, 4.14a, 4.15a and 6.4). Furthermore, significant convective activity was delayed by 3 h in exp. API-24h. The preferred location of convection was along the periphery of the wet soil moisture wedge in the western part of the domain. Due to the altered soil moisture distribution and atmospheric conditions (as a result of starting the experiment one day earlier), RAMS was unable to reproduce a MCS at the proper location. However, by 27/0100, RAMS did produce a quasi-circular cloud shield, but it was much smaller than the observed system and only covered the western Texas panhandle region (Figs. 4.1e and 6.5). This shows that even on a short time scale of 24 h, the soil moisture distribution can alter the boundary layer structure and subsequent soil moisture distribution (through soil moisture- convection feedback process) such that the solution of a numerical experiment can be substantially different.

6.1.2 Effects of vegetation

We used the NDVI dataset to infer the LAI in order to better represent the vegetation characteristics. Note that the heterogeneities in vegetation were not as dramatic as in soil moisture. There was not a vegetation patch with a LAI of 6 adjacent to a patch of LAI of 1

(Fig. 3.2). To test the effects of heterogeneous vegetation, we conducted an additional experiment (exp. HOM50B) for Case 980726 in which we replaced the LAI in grid 3 with homogeneous values (obtained by averaging grid 3 LAI) in exp. HOM50. In exp. HOM50 (Table 4.3), with the soil moisture at 50% saturation, the SRF is essentially one (i.e., the stomata is completely open). Therefore, plants are not under stress and we can infer the effects of vegetation by using exp. HOM50B as a baseline. At 26/1800, a difference field of sea-level pressure, vertical motion and horizontal wind vector at the lowest σ_z-level reveals only small differences between HOM50 and HOM50B (Fig. 6.6). Although somewhat *quantitatively* different, the precipitation in exp. HOM50B was *qualitatively* similar to that in exp. HOM50 (Figs. 4.13h, 4.14h, 4.15h and 6.7).

Shaw et al. (1997) performed sensitivity studies to determine the effects of heterogeneities in soil moisture and vegetation in a numerical experiment of a Great Plains dryline. In that case, the LAI was not permitted to exceed 3, so the heterogeneities in vegetation in this study were comparable to those of Shaw et al. (1997) (see Fig. 3.2). Shaw et al. (1997) found the soil moisture heterogeneities to be a first order effect, while the vegetation heterogeneities to be a second order effect. So, our results were similar to those of Shaw et al. (1997) since soil moisture played a more important role. However, if we impose more drastic heterogeneities in vegetation, it might be possible to produce similar magnitudes of PIMSs from vegetation heterogeneities as seen from soil moisture heterogeneities.

6.1.3 Soil moisture-moist convection feedback

As in the 2D experiments from Emori (1998), our results indicate that convection tends **not** to occur over wetter soil but preferentially over drier soil, either on the periphery of the larger soil moisture anomalies or between two soil moisture anomalies (due to collision of the PIMSs). This is a negative feedback between moist convection and wet soil anomalies.

For convective events, Emori (1998) argued that i) drier soil areas would be wetter over time and ii) wetter soil areas would be drier over time. According to Emori, the locations of dry/wet soil would oscillate with time, but he did not provide a time scale for this oscillation. Emori's arguments seem reasonable. However, Emori only showed results for 20 days, and those results did not indicate the vacillations between wet and dry soil anomalies, but the persistence of the wet soil moisture anomalies on the time scale of a week or more. We extended exp. API (Table 4.3) in Case 980726 to two days. Due to the computational expenses involved, we stopped the experiment at model day 2. At 24 h, we found that soil moisture gradients (at the near surface layer) to be reduced due to the convective precipitation in the formerly drier soil areas, but larger soil moisture anomalies (i.e., S_1 and S_2) could still be identified (Fig. 6.8a). Not much precipitation occurred between 24 h and 48 h, so by 48 h, some of the formerly wet soil areas (in the near surface layer) have dried out, due to surface soil water percolating to deeper levels (Fig. 6.8b) . Nevertheless, even at 48 h, larger soil moisture anomalies (S_1 and S_2) still retained their signatures.

We would have liked to extend our runs to longer time duration and prove or disprove and/or refine Emori's findings, and determine the time scale of the memory of soil moisture anomalies of $\sim$100 km in scale. However, as mentioned earlier, we were limited by our computational resources (one model hour took 4-6 wall clock hours). The numerical experiments in this study were conducted on a single-processor (linux platform). We did not run our experiments in parallel machines (which could speed up the runs significantly) because the nesting "bug" fix was not implemented in the parallel version of RAMS, but only in the sequential version of the code. In the original version of RAMS, when the fine grid values are interpolated back to the coarse grid, the *reference state coarse grid density* is used in the normalization:

$$x_c(t+\Delta t) = \frac{\sum_1^N \bar{\rho}_f^{(i,j)} x_f^{(i,j)}(t+\Delta t)}{N\bar{\rho}_c}, \tag{6.1}$$

where the overbar represents the reference state, the subscripts c and f represent the coarse and fine grids, respectively, and x is an arbitrary scalar, Δt is time step size, and ρ is the air density. To be mathematically consistent, it is clear that the normalization should use the *fine grid density*:

$$x_c(t+\Delta t) = \frac{\sum_1^N \bar{\rho}_f^{(i,j)} x_f^{(i,j)}(t+\Delta t)}{\sum_1^N \bar{\rho}_f{}^{(i,j)}}. \tag{6.2}$$

Because density is a diagnosed quantity from temperature and pressure, the fine grid averaged air density may not necessary be equal to the coarse grid value:

$$\bar{\rho}_c = \frac{\bar{P}_c}{R_d \bar{T}_c} \neq \frac{1}{N}\sum_1^N \frac{\bar{P}_f^{(i,j)}}{R_d \bar{T}_f^{(i,j)}} = \frac{1}{N}\sum_1^N \bar{\rho}_f^{(i,j)}, \tag{6.3}$$

where P is the pressure, R_d is the dry air gas constant, and T is the temperature. In the presence of steep orography, the discrepancy between $\bar{\rho}_c$ and the average of $\bar{\rho}_f{}^{(i,j)}$ could be substantial and the errors could propagate at each time step, leading to unrealistic results. In some cases, the interpolated coarse grid value can exceed those of the fine grid, leading to numerical instability. The above fix alleviates this problem. Scot Rafkin of San Jose State University is credited with the discovery of the "bug". He provided a more complicated "bug" fix, but the simpler fix in the above was found to work the best.

Despite the short duration of model runs, we found that moist convection and wet soil moisture do exhibit a negative feedback as in Emori (1998), especially for the soil moisture anomaly of ~100 km in size (i.e., S_2, Fig. 4.5a). A conceptual feedback diagram is presented in Fig. 6.9. The feedback works as follows. First, convective precipitation falls over

an area, creating a wet soil anomaly. Second, because of the partitioning of the SSHF and SLHF, the wet soil is cooler than its surroundings, inducing PIMSs. Next, a divergent wind anomaly (associated with the PIMSs) flows outward from the wet soil moisture anomaly. As this divergent wind encounters the ambient wind along the wet soil moisture periphery, convergence ensues (if the ambient wind has a component from the opposite direction of the divergent wind anomaly). The convergence leads to upward vertical motion and convection along the periphery of the wet soil anomaly. Convective precipitation then falls along the periphery of the wet soil anomaly, avoiding the interior of the wet soil moisture anomaly. Because of the reduced surface temperature over the wet soil moisture anomaly, the likelihood of convection is reduced. Over time, the drier soil along the wet soil moisture periphery becomes wetter, and the soil moisture distribution is homogenized and the gradients reduced. It is conjectured that if our runs were extended to several weeks, we may not see the oscillations of the positions of wet and dry soil anomalies, since Emori's 2D idealized experiments were devoid of any synoptic-scale forcing. In addition, Emori never explicitly demonstrated this oscillation in his paper. this oscillation in his paper.

6.2 Summary

We have performed sensitivity experiments of soil moisture initialization on the cloud-resolving grid of two simulated MCSs- Case 980726 and Case 990802. The soil moisture of the cloud-resolving grid (grid 3) was derived from the API method using a three-month precipitation dataset at 4-km grid spacing (exp. API). For each set of experiments, we smoothed the initial soil moisture of the cloud-resolving grid with Barnes (1964)'s objective analysis using a response amplitude of 0.5 and a cutoff wavelength of 20 (exp. API20), 40 (exp. API40), and 80 km (exp. API80). In addition, we halved the initial soil moisture in grid 3 from exp. API (exp. APIHALF). A wet soil moisture anomaly (S_2) was displaced

from its initial location to suppress convection (exp. APIMOVES2). Furthermore, we also conducted two experiments with homogeneous soil moisture initialization in the cloud resolving grid at 31% (exp. HOM31) and 50% (exp. HOM50) saturation. Our findings are summarized below:

- Heterogeneities in soil moisture create physiographic-induced mesoscale systems (PIMSs), analogous to sea breeze, through differential heating. Wetter soil was cooler than the surrounding drier soil, thus an anomalous high pressure developed over the wetter soil, and a divergent flow emanated from the wetter soil. As the divergent flow encountered the ambient flow (with a component in the opposite direction from the divergent wind) around the periphery of the wetter soil patch, low-level convergence ensued. Thus, upward motion was enhanced around the periphery of wetter soil. This was best exemplified by S_2.

- In some instances, collision between PIMSs provided regions of convergence, leading to upward motion and moist convection.

- Larger soil moisture anomalies were more able to retain their signatures despite the smoothing operation, and their associated perturbation fields in sea-level pressure, low-level wind and vertical motion were more prominent.

- Smaller soil moisture anomalies were more easily smoothed out by the objective analysis filter. As a result, smaller soil moisture anomalies were not well represented in the smoothed soil moisture initialization (i.e., with cutoff wavelength of 80 km), leading to underestimated PIMS and precipitation (associated with the PIMS) in exp. API80 for both Case 980726 and Case 990802.

- The PIMSs generated by the larger soil moisture anomalies ($\sim$100 km in size) were weakly dependent on the internal finer scale features. However, wet soil anomalies

of 30-40 km in size were still able to trigger convection, contrary to 2-D idealized simulations by Yan and Anthes (1988) in which they found strips of dry/moist land of 100-200 (24 and 48) km in width were (were not) effective in initiating convective precipitation. Our results were more consistent with those of Chen and Avissar (1994b) in which they found that even for land surface moisture discontinuity on the order of 20 km, strong precipitation could still be produced. Thus, in explicit simulations of convection, the model initialization should resolve soil moisture patches of tens of kilometers in size in order to well represent the PIMSs associated with the soil moisture anomalies.

- Exp. HOM50 (relatively wet soil at 50% saturation in the entire cloud-resolving grid) delayed convection and reduced the domain-averaged precipitation rate and accumulation for Case 980726 and Case 990802. Previous research with models using different convective parameterizations produced different results in terms of domain-averaged accumulated precipitation in wet soil regimes (e.g., Gallus and Segal 2000). This is the disadvantage of convective parameterization because of the different closures and grid-spacing dependencies in different schemes. Therefore, modelers using convective parameterization should be cautious when encountering wet soil regimes.

- Pielke (2001) noted that although wetter soil increases latent heat flux into the atmosphere, raising the CAPE, deep convection may be more difficult due to the reduced sensible heat flux. However, Chen et al. (2001a) suggested that if convection does occur over wetter soil, it would be more severe and rain more heavily. We found that just before significant convection started in exps. HOM50, API, and HOM31 for Case 980726, the maximum upward motion in grid 3 at 700-hPa was 4.5, 3, 2.7 m s^{-1}, respectively. A similar trend was also seen in Case 990802. Our findings seem to confirm the ideas proposed by Pielke (2001) and Chen et al. (2001a).

- Low-level convergence provided by a quasi-stationary front in Case 980726 and a quasi-stationary front and a surface trough in Case 990802 provided a favorable environment for the initiation of convection. Nevertheless, the distribution of soil moisture influenced the location where convection occurred. Wet soil suppressed convection, but around the periphery of wet soil moisture anomalies, vertical motion and moist convection were enhanced. This is consistent with the idea of a negative feedback between soil moisture and moist convection proposed by Emori (1998).

- The *negative feedback between soil moisture and moist convection is different from the positive feedback between soil moisture and precipitation in a baroclinic wave.* Using a 2D semi-geostrophic model, Castelli and Rodriguez-Iturbe (1995) found that when the ascending-moist (descending-dry) areas the baroclinic wave developed on top of a wetter (drier) soil, the frontal collapse was reached sooner and the estimated precipitation higher. A conceptual diagram of the feedback between soil moisture and moist convection is shown in Fig. 6.9.

- Long-lived convective cells interacted with larger soil moisture anomalies in which the convective cells tended to track along the periphery of the larger wet soil moisture anomalies. This effect was caused by enhanced convergence and upward motion along the periphery of the wet soil moisture anomaly, serving as a focusing mechanism for convection to develop.

6.3 Suggestions for Future Work

Although the Oklahoma Mesonet has the highest resolution (an average station spacing of 50 km) in soil moisture measurement, there are missing data temporally and spatially (at least for the time period in this study). Perhaps in the Mesonet archive, there exists a

complete dataset at other times and one can investigate whether an anti-correlation exists between soil moisture and convection over Oklahoma and prove, disprove, and/or refine the theory of negative feedback in soil moisture and convective precipitation.

Besides conventional networks and remote sensing (e.g., low-frequency microwave remote sensors), other options should be explored to retrieve and/or measure soil moisture, for example, using an artificial neural network (ANN) to estimate soil moisture. Dr. Hongli Jiang, a research scientist, in our group has been working with an ANN model to obtain a better estimate of soil moisture. The ANN used by Jiang was originally developed in the Department of Hydrology at the University of Arizona to infer precipitation from satellite data (Hsu et al. 1997). Jiang has recently obtained some encouraging results with the ANN. The ANN approach has great potential and has only attracted attention in the atmospheric and oceanographic community recently (Hsieh and Tang 1998). Thus, there is much room for research in the application of ANN to soil moisture estimation.

In this study, we were limited by computing resources and forced to choose quasi-stationary MCSs in order to confine the MCS in the cloud-resolving grid. One could use a larger domain to simulate non-stationary MCSs, e.g., for Great Plains MCSs that have origins in the Rockies. For such cases, less organized convection begins over the Rockies and the convective cells move east towards the Great Plains where they undergo "upscaling" processes and develop into MCSs. Although the surface fluxes are more crucial during the developmental stage of the MCS, the dynamics involved is nonlinear. It would be of interest to investigate how the initial soil moisture affects the *entire lifecycle* of the MCS with a large cloud-resolving grid. Also, the limited area of our cloud-resolving grid limits the true influence of the PIMSs, making our results a bit more conservative. In addition, the short duration of the experiments cannot adequately answer the question as to the time scale of the memory of soil moisture anomalies of $\sim$100 km in size. When more powerful

computing resources become available to the research community, we can afford to run real-data cloud-resolving simulations over a much larger area and address these issues.

In both Case 980726 and Case 990802, large-scale forcing initiated convection (a quasi-stationary front for Case 980726 and a surface trough and a quasi-stationary front for Case 990802). It would be of interest to examine the sensitivity of soil moisture initialization in conjunction with various degrees of large-scale forcing. We have attempted to do so by altering the low-level baroclinicity[1] (the quasi-stationary front in Case 980726) with a PV "surgery" technique (Huo et al. 1998, 1999; Zhang et al. 2002) based on the piecewise PV inversion developed by Davis and Emanuel (1991). The advantage of this technique is that for a given PV anomaly, the inverted mass and wind fields are balanced. Thus, the model will not lose the altered initial conditions through excitation of gravity waves when a PV anomaly is removed. However, the altering of the low-level baroclinicity was more problematic than anticipated due to the difficulties in isolating the PV anomaly (associated with the quasi-stationary front) and the non-local effects of the inversion. Nevertheless, the piecewise PV inversion technique could still be employed to construct an idealized large-scale *balanced* atmospheric initial condition, and the strength of the large-scale forcing can be altered. For example, one can superpose inverted wind and mass fields associated with a specified baroclinic zone (representing a quasi-stationary front) on top of a balanced zonal background flow. We can vary the degree of baroclinicity to simulate the strength of the quasi-stationary front. In both Case 980726 and 990802, upper-level PV anomalies did not play a role, but for other MCSs, especially MCCs, upper-level PV anomalies often do play a role. We can study the sensitivity of strength of upper-level PV anomalies by superposing inverted wind and mass fields associated with a specified upper-level PV anomaly and altering the magnitudes of the inverted wind and mass fields.

[1]The surface potential temperature is considered a "surrogate" PV or PV embedded in an infinitesimally thin layer (Hoskins et al. 1985).

In this study, the heterogeneites in vegetation were not as drastic as those in soil moisture. Future studies could impose more drastic heterogeneites in vegetation and test whether the PIMSs generated by heterogeneites in vegetation can be similar in magnitude to PIMSs generated by heterogeneites in soil moisture.

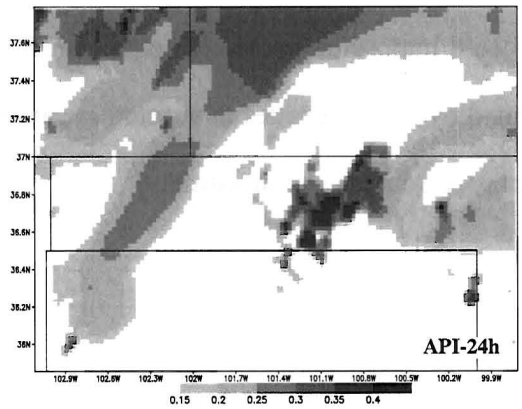

Figure 6.1 Volumetric soil moisture (m^3 m^{-3}) at 2 cm below the surface in grid 3 for exp. API-24h in Case 980726 at 26/1200.

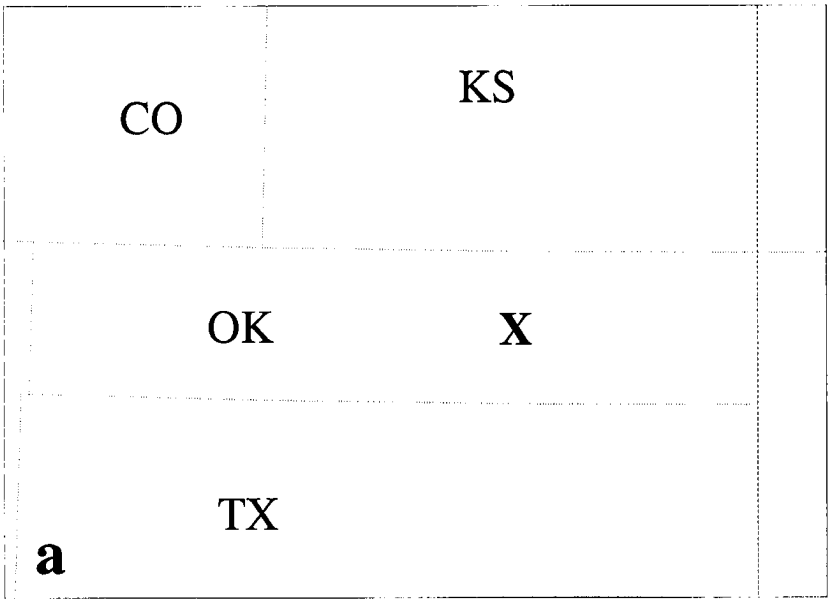

Figure 6.2 a) Map indicating the location at which the sounding was taken in (b) and (c). b) Skew T-log p diagram for temperature (^{o}C), dew point temperature (^{o}C), and wind (m s^{-1}) on 1200 UTC 26 July 1998 at 'X' in (a) for exp. API. A full (half) barb is 5 (2.5) m s^{-1}. c) Same as (b) but for exp.API-24h.

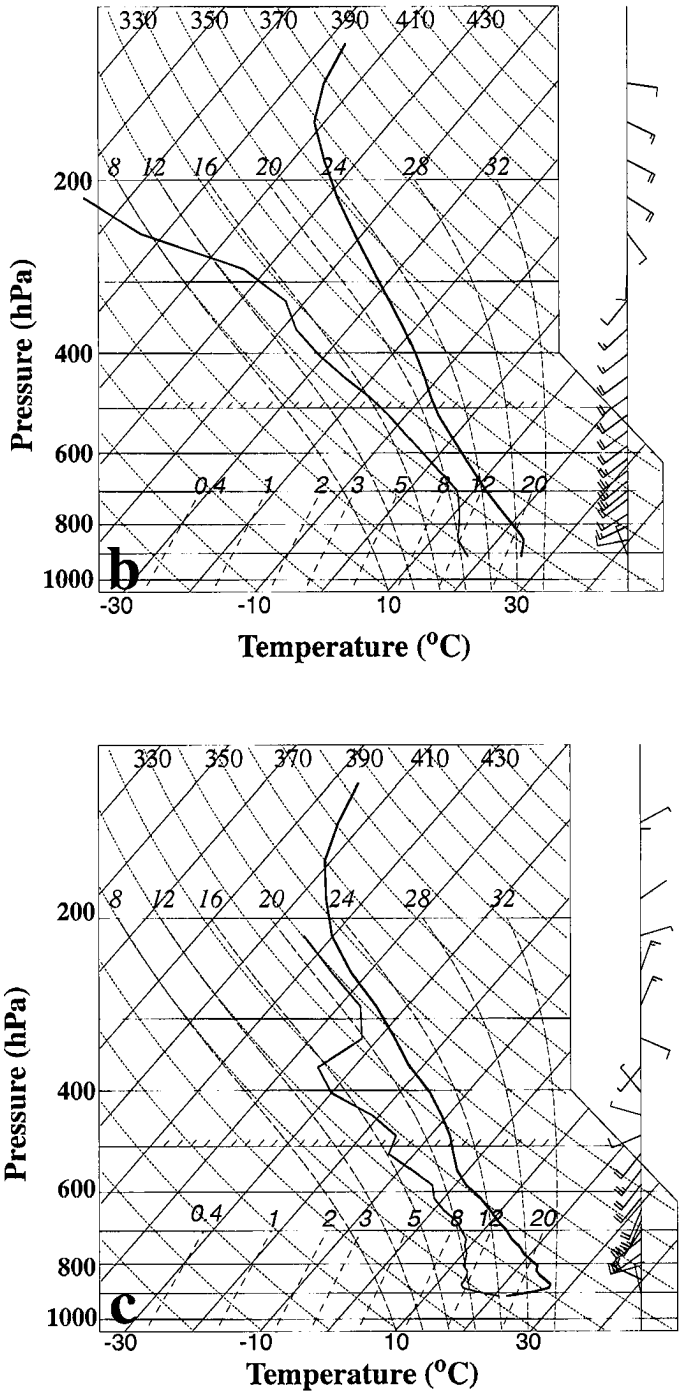

Figure 6.2 Continued.

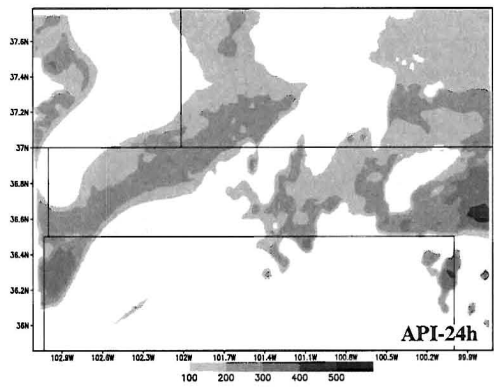

Figure 6.3 As in Fig. 4.8a but for exp. API-24h in Case 980726 at 26/1600.

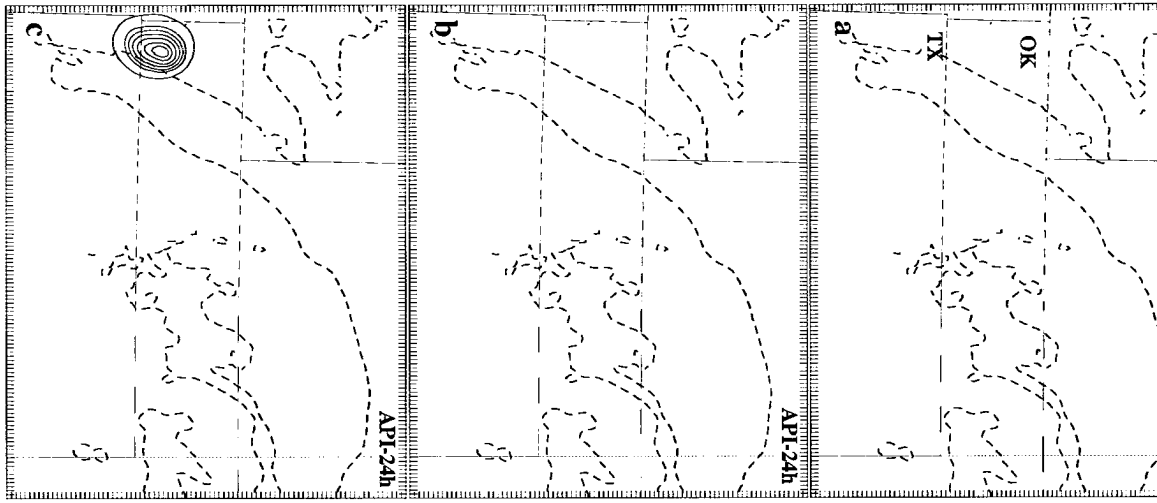

Figure 6.4 As in Fig. 4.13a but for exp. API-24h at a) 26/1915; b) 26/2145; c) 26/2300. Dashed contour represents the 50% saturation in soil moisture at 26/1200.

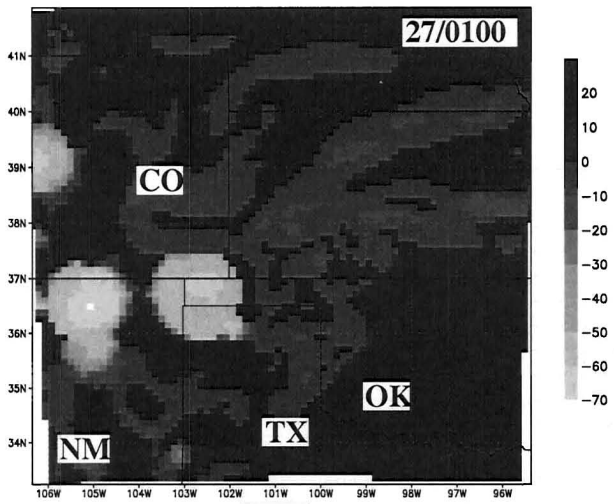

Figure 6.5 As in Fig.4.7a but for exp. API-24h in Case 980726 at 27/0100.

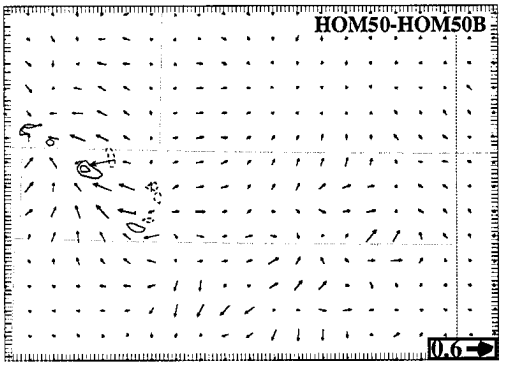

Figure 6.6 As in Fig. 4.11a but for exp. HOM50-HOM50B in Case 980726 at 26/ 1800. Exp. HOM50B is the same as exp. HOM50 except that the grid 3 LAI in exp. HOM50B has a homogeneous value of 2.9.

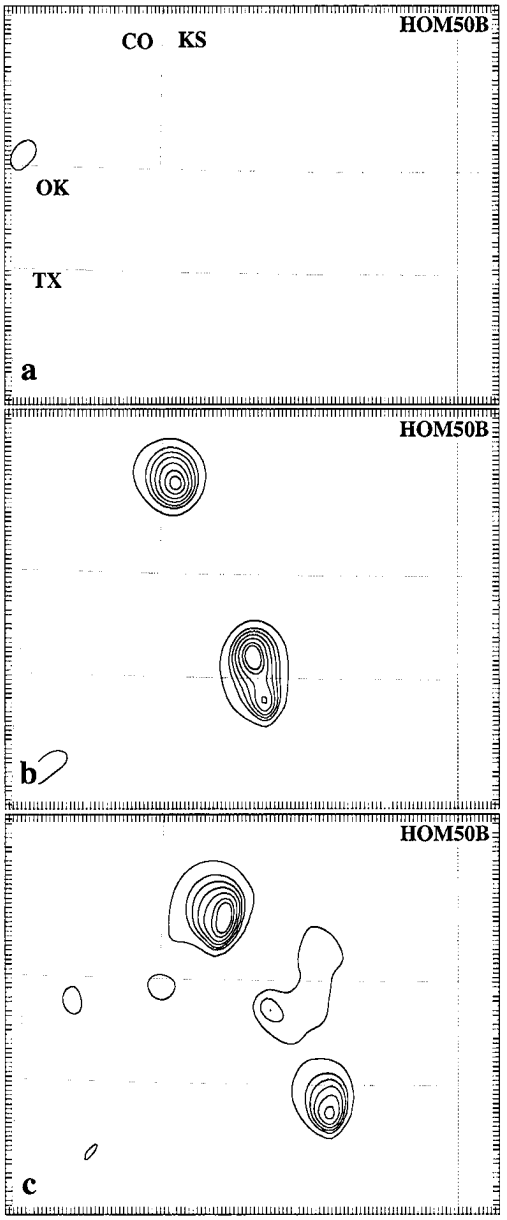

Figure 6.7 As in Fig. 4.13a but for exp. HOM50B at a) 26/1915; b) 26/2145; c) 26/2300.

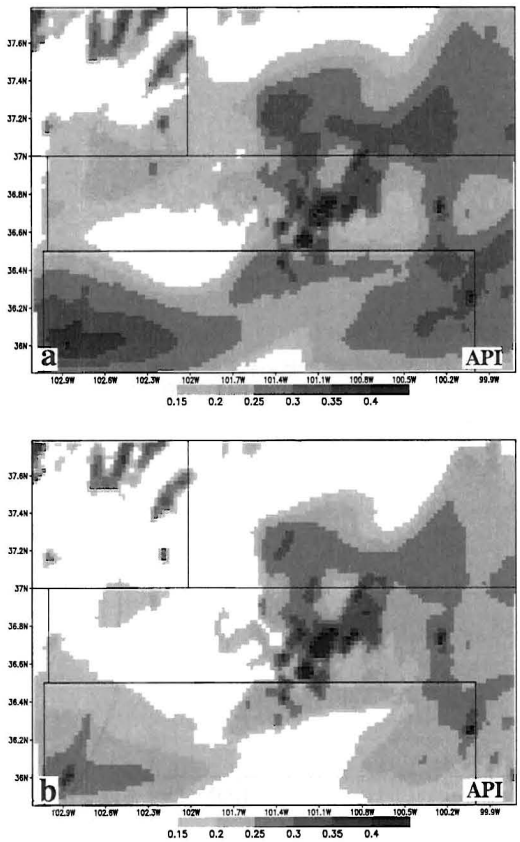

Figure 6.8 Volumetric soil moisture (m^3 m^{-3}) at 2 cm below the surface in grid 3 for exp. API in Case 980726 at a) 27/1200; b) 28/1200.

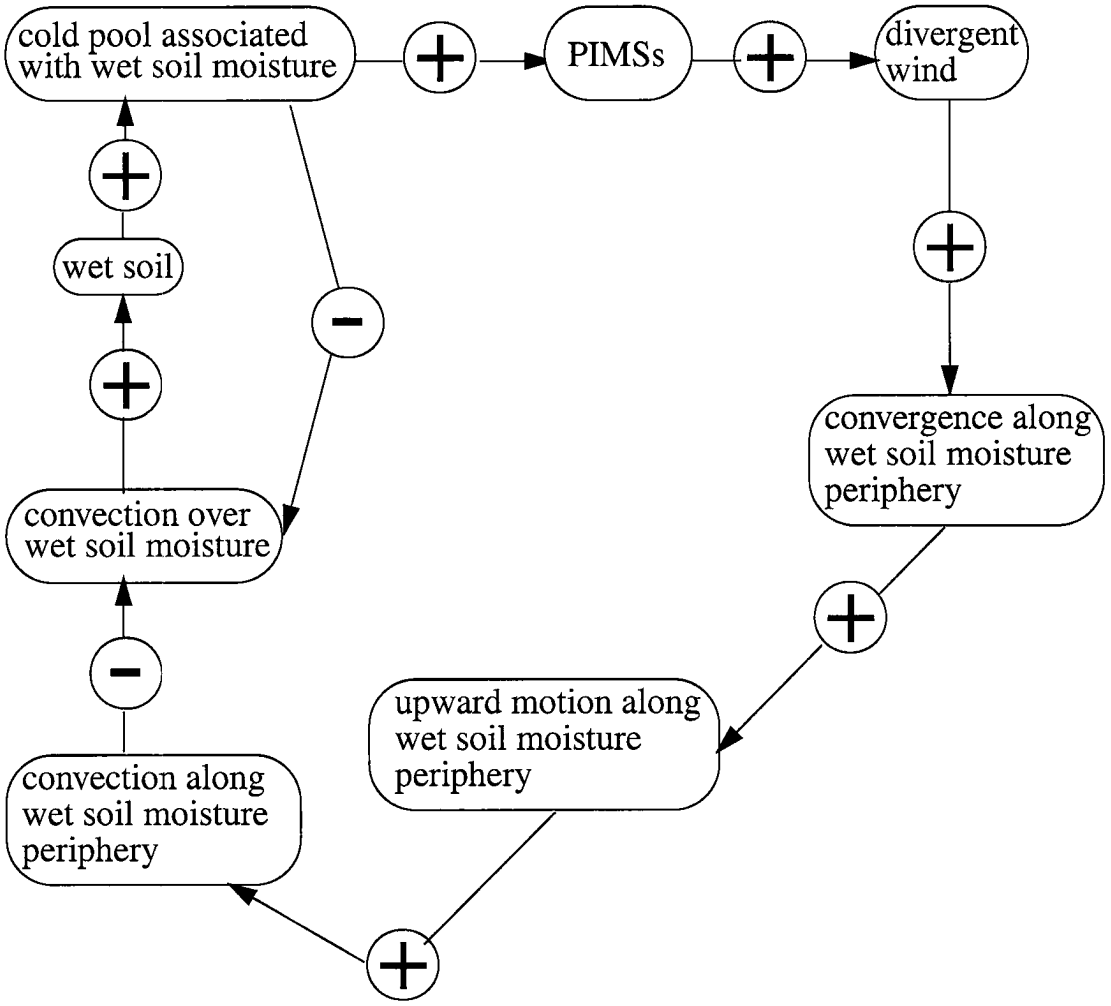

Figure 6.9 Conceptual diagram of soil moisture-moist convection feedback. "+" and "-" symbols represent positive and negative feedbacks, respectively. The soil moisture anomaly is assumed to be ~100 km in size.

Bibliography

Anthes, R. A., 1977: A cumulus parameterization scheme utilizing a one-dimensional cloud model. *Mon. Wea. Rev.*, **105,** 270–286.

Arakawa, A. and V. R. Lamb, 1977: *Methods of computational physics*. Academic Press, 174-265 pp.

Arakawa, A. and W. H. Schubert, 1974: Interaction of a cumulus cloud ensemble with the large-scale environment. Part I. *J. Atmos. Sci.*, **31,** 674–701.

Ashby, C. T., W. R. Cotton, and R. McAnelly, 2001: Impact of soil moisture initialization on a simulated flash flood. Preprints, *Proceedings on the 15th Conference on Precipitation Extremes: Prediction, Impacts, and Responses, 14-19 January 2001*. Albuquerque, NM, American Meterological Society, 260-263.

Avissar, R. and R. A. Pielke, 1991: The impact of plant stomatal control on mesoscale atmospheric circulations. *Agric. Forest Meteor.*, **54,** 353–372.

Barnes, S. L., 1964: A technique for maximizing details in numerical weather map analysis. *J. Appl. Meteor.*, **3,** 396–409.

Bell, G. D. and J. E. Janowiak, 1995: Atmospheric circulation associated with the Midwest floods of 1993. *Bull. Amer. Met. Soc.*, **76,** 681–696.

Bernardet, L. R. and W. R. Cotton, 1998: Multiscale evolution of a derecho-producing mesoscale convective system. *Mon. Wea. Rev.*, **126,** 2991–3015.

Bernardet, L. R., L. D. Grasso, J. E. Nachamkin, C. A. Finley, and W. R. Cotton, 2000: Simulating convective events using a high-resolution mesoscale model. *J. Geophys. Res.*, **105,** 14963–14982.

Betts, A. K., 1974: The scientific basis and objectives of the U.S. subprogram for the GATE. *Bull. Amer. Meteor. Soc.*, **55,** 304–313.

Betts, A. K. and M. J. Miller, 1986: A new convective adjustment scheme. Part II: Single column tests using GATE wave, BOMEX, and arctic air-mass data sets. *Quart. J. Roy. Meteor. Soc.*, **112,** 693–709.

Bluestein, H. B., 1992: *Storm and Cloud Dynamics. Volume 2: Observations and theory of weather systems.* Oxford University Press, 594 pp.

Bluestein, H. B. and M. H. Jain, 1985: The formation of mesoscale lines of precipitation: Severe squall lines in Oklahoma during the spring. *J. Atmos. Sci.*, **42,** 1711–1732.

Brown, J. M., 1979: Mesoscale unsaturated downdrafts driven by rainfall evaporation: A numerical study. *J. Atmos. Sci.*, **36,** 313–338.

Carlson, T. N. and D. A. Ripley, 1997: On the relation between NDVI, fractional vegetation cover, and leaf area index. *Remote Sens. Environ.*, **62,** 241–252.

Castelli, F. and I. Rodriguez-Iturbe, 1995: Soil moisture-atmosphere interaction in a moist semigeostrophic model of baroclinic instability. *J. Atmos. Sci.*, **52,** 2152–2159.

Chang, J.-T. and P. J. Wetzel, 1991: Effects of spatial variations of soil moisture and vegetation on the evolution of a prestorm environment: A numerical case study. *Mon. Wea. Rev.*, **119,** 1368–1390.

Chen, F. and R. Avissar, 1994a: The impact of land-surface wetness heterogeneity on mesoscale heat fluxes. *J. Appl. Met.*, **33,** 1323–1340.

Chen, F. and R. Avissar, 1994b: Impact of land-surface moisture variability on local shallow convective cumulus and precipitation in large-scale models. *J. Appl. Met.*, **33,** 1382–1401.

Chen, F., R. A. Pielke, Sr., and K. Mitchell, 2001a: Development and application of land-surface models for mesoscale atmospheric models: Problems and promises. Lakshmi, V., J. Alberston, and J. Schaak, editors, *Observations and Modeling of the Land-Surface Hydrological Processes*, pages 107–135. American Geophysical Union.

Chen, F., T. T. Warner, and K. Manning, 2001b: Sensitivity of orographic moist convection to landscape variability: A study of the Buffalo Creek, Colorado, flash flood case of 1996. *J. Atmos. Sci.*, **58,** 3204–3223.

Cheng, W.Y.Y., T. Wu, and W. R. Cotton, 2001: Large-eddy simulations of the 26 November 1991 FIRE II cirrus case. *J. Atmos. Sci.*, **58,** 1017–1034.

Choudhury, B. J. and B. J. Blanchard, 1983: Simulating soil water recession coefficients for agricultural water sheds. *Water Resources Bull.*, **19,** 241–247.

Clark, C. A. and R. W. Arritt, 1995: Numerical simulations of the effect of soil moisture and vegetation cover on the development of deep convection. *J. Appl. Meteor.*, **34,** 2029–2045.

Copeland, J. H., R. A. Pielke, and T.G.F. Kittel, 1996: Potential climatic impacts of vegetation change: A regional modeling study. *J. Geophys. Res.*, **101,** 7409–7418.

Cotton, W. R. and R. A. Anthes, 1989: *Storm and Cloud Dynamics*. Academic Press, 883 pp.

Cotton, W. R., M.-S. Lin, R. L. McAnelly, and C. J. Trembeck, 1989: A composite model of mesoscale convective complexes. *Mon. Wea. Rev.*, **117,** 765–783.

Cotton, W. R., R. A. Pielke, Sr., R. L. Walko, G. E. Liston, C. J. Tremback, H. Jiang, R. L. McAnelly, J. Y. Harrington, and M. E. Nicholls, 2002: RAMS 2001: Current status and future directions. *Meteor. Atmos. Phys.*, In press.

Dalu, G. A. and R. A. Pielke, 1993: Vertical heat fluxes generated by mesoscale atmospheric flow induced by thermal inhomogeneities in the PBL. *J. Atmos. Sci.*, **50,** 919–926.

Dalu, G. A., R. A. Pielke, R. Avissar, G. Kallos, M. Baldi, and A. Guerrini, 1991: Linear impact of thermal inhomogeneities on mesoscale atmospheric flow with zero synoptic wind. *Ann. Geophys.*, **9,** 641–647.

Davis, C. A. and K. A. Emanuel, 1991: Potential vorticity diagnostics of cyclogenesis. *Mon. Wea. Rev.*, **119,** 1929–1953.

Dirmeyer, P. A., 1995: Problems in initializing soil wetness. *Bull. Amer. Met. Soc.*, **76(11),** 2234–2240.

Dirmeyer, P. A. and J. Shukla, 1993: Observational and modeling studies of the influence of soil moisture anomalies on the atmospheric circulation. Shukla, J., editor, *Predictions of Interannual Climate Variations*, pages 1–23. Series I, Vol. 6, Springer-Verlag.

Djurić, D., 1994: *Weather Analysis*. Prentice-Hall, 304 pp.

Eastman, J. L., M. B. Coughenour, and R. A. Pielke, Sr., 2001a: Does grazing affect regional climate? *J. Hydromet.*, **2,** 243–253.

Eastman, J. L., M. B. Coughenour, and R. A. Pielke, Sr., 2001b: The effects of CO2 and landscape change using a coupled plant and meteorological model. *Global Change Biology*, **7,** 797–815.

Emori, S., 1998: The interaction of cumulus convection with soil moisture distribution: An idealized simulation. *J. Geophys. Res.*, **103 (D8),** 8873–8884.

Entekhabi, D., I. Rodriguez-Iturbe, and F. Castelli, 1996: Mutual interaction of soil moisture state and atmospheric processes. *J. Hydro.*, **184,** 3–17.

Fast, J. D. and M. D. McCorcle, 1991: The effect of heterogeneous soil moisture on a summer baroclinic circulation in the central United States. *Mon. Wea. Rev.*, **119,** 2140–2167.

Finley, C. A., R. A. Pielke, and W. R. Cotton, 2001: Numerical simulation of tornadogenesis in a high-precipitation supercell. Part I: Storm evolution and transition into a bow echo. *J. Atmos. Sci.*, **58,** 1597–1629.

Fritsch, J. M., R. J. Kane, and C. R. Chelius, 1986: Contribution of mesoscale convective weather systems to the warm-season precipitation in the United States. *J. Clim. App. Met.*, **25,** 1333–1345.

Fujita, T. T., 1959: Precipitation and cold air production in mesoscale thunderstorm systems. *J. Meteorol.*, **16,** 454–466.

Gallus, W. A. and M. Segal, 2000: Sensitivity of forecast rainfall in a Texas convective system to soil moisture and convective parameterization. *Wea. Forecast.*, **15,** 509–525.

Gamache, J. F. and R. A. Houze, 1982: Mesoscale air motions associated with a tropical squall line. *Mon. Wea. Rev.*, **110,** 118–135.

Golaz, J.-C., H. Jiang, and W. R. Cotton, 2001: A large-eddy simulation study of cumulus clouds over land and sensitivity to soil moisture. *Atmos. Res.*, **59-60,** 373–392.

Grasso, L. D., 1996: *Numerical simulation of the May 15 and April 26, 1991 thunderstorms*. Ph.D. dissertation, Colorado State University, Fort Collins.

Grasso, L. D., 2000a: The dissipation of a left-moving cell in a severe storm environment. *Mon. Wea. Rev.*, **128,** 2797–2815.

Grasso, L. D., 2000b: A numerical simulation of dryline sensitivity to soil moisture. *Mon. Wea. Rev.*, **128,** 2816–2834.

Grasso, L. D. and W. R. Cotton, 1995: Numerical simulation of a tornado vortex. *J. Atmos. Sci.*, **52,** 1192–1203.

Greene, E. M., G. E. Liston, and R. A. Pielke, Sr., 1999: Relationships between landscape, snowcover depletion, and regional weather and climate. *Hydrological Processes*, **13,** 2453–2466.

Grell, G. A., 1993: Prognostic evaluation of assumptions used by cumulus parameterizations. *Mon. Wea. Rev.*, **121,** 764–787.

Harrington, J. Y., 1997: *The effects of radiative and microphysical processes on simulated warm and transition-season Arctic stratus*. Ph.D. dissertation, Colorado State University, Fort Collins.

Harrington, J. Y., M. P. Meyers, R. L. Walko, and W. R. Cotton, 1995: Parameterization of ice crystal conversion processes due to vapor deposition for mesoscale models using double-moment basis functions. *J. Atmos. Sci.*, **52,** 4344–4366.

Harrington, J. Y., T. Reisin, W. R. Cotton, and S. M. Kreidenweis, 1999: Cloud resolving simulations of Arctic stratus. Part II: Transition-season clouds. *Atmos. Res.*, **51,** 45–75.

Hill, G. E., 1974: Factors controlling the size and spacing of cumulus clouds as revealed by numerical experiments. *J. Atmos. Sci.*, **31,** 646–673.

Holton, J. R., 1967: The diurnal boundary layer wind oscillation above sloping terrain. *Tellus*, **19,** 119–205.

Hoskins, B. J., M. E. McIntyre, and A. W. Robertson, 1985: On the use and significance of isentropic potential vorticity maps. *Q. J. R. Meteorol. Soc.*, **111,** 877–946.

Hoxit, L. R., C. F. Chappell, and J. M. Fritsch, 1976: Formation of mesolows or pressure troughs in advance of cumulonimbus. *Mon. Wea. Rev.*, **104,** 1419–1428.

Hsie, E.-Y., R. A. Anthes, and D. Keyser, 1984: Numerical simulation of frontogenesis in a moist atmosphere. *J. Atmos. Sci.*, **41,** 2581–2594.

Hsieh, W. W. and B. Tang, 1998: Applying neural network models to prediction and data analysis in meteorology and oceanography. *Bull. Amer. Met. Soc.*, **79(9),** 1855–1870.

Hsu, K.-L., X. Gao, S. Sorooshian, and H. V. Gupta, 1997: Precipitation estimation from remotely sensed information using artificial neural networks. *J. App. Met.*, **36,** 1176–1190.

Huo, Z., D.-L. Zhang, and J. R. Gyakum, 1998: An application of potential vorticity inversion to improving the numerical prediction of the March 1993 superstorm. *Mon. Wea. Rev.*, **126,** 424–436.

Huo, Z., D.-L. Zhang, and J. R. Gyakum, 1999: Interaction of potential vorticity anomalies in extratropical cyclogenesis. Part II: Sensitivity to initial perturbations. *Mon. Wea. Rev.*, **127,** 2563–2575.

Janjic, Z. I., 1994: The step-mountain eta coordinate model: Further development of the convection, viscous sublayer and turbulence closure model schemes. *Mon. Wea. Rev.*, **122,** 928–945.

Johnson, R. H. and P. J. Hamilton, 1988: The relationship of surface pressure features to the precipitation and air flow structure of an intense midlatitude squall line. *Mon. Wea. Rev.*, **116,** 1444–1472.

Kain, J. S. and J. M. Fritsch, 1990: A one-dimensional entraining/detraining plume model and its application convective parameterization. *J. Atmos. Sci.*, **47,** 2784–2802.

Klemp, J. B. and R. B. Wilhelmson, 1978: The simulation of three-dimensional convective storm dynamics. *J. Atmos. Sci.*, **35,** 1070–1096.

Koch, S. E., A. Aksakal, and J. T. McQueen, 1997: The influence of mesoscale humidity and evapotranspiration fields on a model forecast of a cold-frontal squall line. *Mon. Wea. Rev.*, **125,** 384–409.

Kunkel, K. E., S. A. Changnon, and J. R. Angel, 1993: Climatic aspects of the 1993 Mississippi River Basin Flood. *Bull. Amer. Met. Soc.*, **75,** 811–822.

Kuo, S. L., 1974: Further studies of the parameterization of the effect of cumulus convection on large-scale flow. *J. Atmos. Sci.*, **31,** 1232–1240.

Laing, A. G. and J. M. Fritsch, 2000: The large-scale environments of the global populations of mesoscale convective complexes. *Mon. Wea. Rev.*, **128,** 2756–2776.

Lilly, D. K., 1962: On the numerical simulation of buoyant convection. *Tellus*, **14,** 148–172.

Liston, G. E. and R. A. Pielke, 2001: A climate version of the Regional Atmospheric Modeling System. *Theor. Appl. Climatology*, **68,** 155–173.

Liu, Y. and R. Avissar, 1999: A study of persistence in the land-atmosphere system using a general circulation model and observations. *J. Clim.*, **12,** 2139–2153.

Lu, L., R. A. Pielke, G. E. Liston, W. J. Parton, D. Ojima, and M. Hartman, 2001: Implementation of a two-way interactive atmospheric and ecological model and its application to the central United States. *J. Clim.*, **14,** 900–919.

Maddox, R. A., 1980: Mesoscale convective complexes. *Bull. Amer. Meteor. Soc.*, **61,** 1374–1387.

Maddox, R. A., 1983: Large-scale meteorological conditions associated with midlatitude, mesoscale convective complexes. *Mon. Wea. Rev.*, **111,** 1475–1493.

Manabe, S., 1969: Climate of the ocean circulation: Part I. *Mon. Wea. Rev.*, **97,** 739–774.

McAnelly, R. L. and W. R. Cotton, 1986: Meso-β-scale characteristics of an episode of meso-α-scale convective complexes. *Mon. Wea. Rev.*, **114,** 1740–1770.

McAnelly, R. L. and W. R. Cotton, 1989: The precipitation life cycle of mesoscale convective complexes over the central United States. *Mon. Wea. Rev.*, **117,** 784–808.

McAnelly, R. L., J. E. Nachamkin, W. R. Cotton, and M. E. Nicholls, 1994: Upscale evolution of MCSs: Doppler radar analysis and analytical investigation. *Mon. Wea. Rev.*, **125,** 1083–1110.

McCorcle, M. D., 1988: Simulation of surface-moisture effects on the Great Plains low-level jet. *Mon. Wea. Rev.*, **116,** 1705–1720.

Mellor, G. L. and T. Yamada, 1982: Development of a turbulence closure model for geophysical fluid problems. *Rev. Geophys. Space Phys.*, **20,** 851–875.

Meyers, M. P., R. L. Walko, J. Y. Harrington, and W. R. Cotton, 1997: New RAMS cloud microphysics parameterization. Part II: The two-moment scheme. *Atmos. Res.*, **45,** 3–39.

Nachamkin, J. E. and W. R. Cotton, 2000: Interactions between a developing mesoscale convective system and its environment. Part II: Numerical simulation. *Mon. Wea. Rev.*, **128,** 1225–1244.

Namias, J., 1959: Persistence of mid-tropspheric ciculations between adjacent months and seasons. Bolin, B., editor, *The atmosphere and the sea in motion*, pages 240–248. Rossby Memorial Volume.

Olsson, P. Q. and W. R. Cotton, 1997: Balanced and unbalanced circulations in a primitive equation simulation of a midlatitude MCC. Part I: The numerical simulation. *J. Atmos. Sci.*, **54,** 457–478.

Ookouchi, Y., M. Segal, R. C. Kessler, and R. A. Pielke, 1984: Evaluation of soil moisture effects on the generation and modification of mesoscale circulations. *Mon. Wea. Rev.*, **112,** 2281–2292.

Pan, Z., E. Takle, M. Segal, and R. Turner, 1996: Influences of model parameterization schemes on the response of rainfall to soil moisture in the central United States. *Mon. Wea. Rev.*, **124,** 1786–1802.

Pielke, R. A., 2001: Influence of the spatial distribution of vegetation and soils on the prediction of cumulus convective rainfall. *Rev. Geophys.*, **39,** 151–177.

Pielke, R. A., W. R. Cotton, R. L. Walko, C. J. Tremback, W. A. Lyons, L. D. Grasso, M. E. Nicholls, M. D. Moran, D. A. Wesley, T. J. Lee, and J. H. Copeland, 1992: A

comprehensive meteorological modeling system - RAMS. *Meteorol. Atmos. Phys.*, **49,** 69–91.

Pielke, R. A., G. Dalu, J. Eastman, P. L. Vidale, and X. Zeng, 1998: Boundary layer processes and land surface interactions on the mesoscale. Holtslag, A.A.M. and P. G. Duynkerke, editors, *Clear and Cloudy Boundary Layers*, pages 155–176. Royal Netherlands Academy of Arts and Sciences.

Pielke, R. A., T. J. Lee, J. H. Copeland, J. L. Eastman, C. L. Ziegler, and C. A. Finley, 1997: Use of USGS-provided data to improve weather and climate simulations. *Ecological Applications*, **7,** 3–21.

Pielke, R. A., G. E. Liston, J. L. Eastman, L. Lu, and M. Coughenour, 1999a: Seasonal weather prediction as an initial value problem. *J. Geophys. Res.*, **104,** 19463–19479.

Pielke, R. A. and M. Segal, 1986: Mesoscale circulations forced by differential terrain heating. Ray, P. S., editor, *Mesoscale meteorology and forecasting*, pages 516–548. American Meteorological Society.

Pielke, R. A., R. L. Walko, L. Steyaert, P. L. Vidale, G. E. Liston, and W. A. Lyons, 1999b: The influence of anthropogenic landscape changes on weather in south Florida. *Mon. Wea. Rev.*, **127,** 1663–1673.

Pielke, R. A., Sr., 2002: *Mesoscale Meteorological Modeling.* Academic Press, 2nd edition, 676 pp.

Rutledge, S. A., 1986: A diagnostic modeling study of the stratiform region associated with a tropical squall line. *J. Atmos. Sci.*, **43,** 1356–1377.

Rutledge, S. A. and R. A. Houze, 1987: A diagnostic study of the trailing stratiform region of a midlatitude squall line. *J. Atmos. Sci.*, **44,** 2640–2656.

Sanders, F. and K. A. Emanuel, 1977: Momentum budget and temporal evolution of a mesoscale convective system. *J. Atmos. Sci.*, **34,** 322–330.

Sawyer, J. S., 1946: Cooling by rain as a cause of pressure rise in convective squalls. *Quart. J. Roy. Meteor. Soc.*, **72,** 168.

Segal, M. and R. W. Arritt, 1992: Nonclassical mesoscale circulations caused by surface sensible heat-flux gradients. *Bull. Amer. Met. Soc.*, **73,** 1593–1604.

Segal, M., R. Avissar, M. C. McCumber, and R. A. Pielke, 1988: Evaluation of vegetation effects on the generation and modification of mesoscale circulations. *J. Atmos. Sci.*, **45,** 2268–2292.

Segal, M., W. Schreiber, G. Kallos, R. A. Pielke, J. R. Garratt, J. Weaver, A. Rodi, and J. Wilson, 1989: The impact of crop areas in northeast Colorado in midsummer mesoscale thermal circulations. *Mon. Wea. Rev.*, **117,** 809–825.

Sellers, P. J., C. J. Tucker, G. J. Collatz, S. O. Los, C. O. Justice, D. A. Dazlich, and D. A. Randall, 1994: A global 1 degree by 1 degree NDVI data set for climate studies. Part 2: The generation of global fields of terrestrial biophysical parameters from the NDVI. *Int. J. Rem. Sens.*, **15,** 3519–3545.

Shaw, B. L., R. A. Pielke, and C. L. Ziegler, 1997: A three-dimensional numerical simulation of a Great Plains dryline. *Mon. Wea. Rev.*, **125,** 1489–1506.

Smagorinsky, J., 1963: General circulation experiments with the primitive equations. Part I: The Basic experiment. *Mon. Wea. Rev.*, **91,** 99–164.

Smull, B. F. and R. A. Houze, 1985: A midlatitude squall line with a trailing region of stratiform rain: Radar and satellite observations. *Mon. Wea. Rev.*, **113,** 117–133.

Smull, B. F. and R. A. Houze, 1987a: Dual-Doppler radar analysis of a mid-latitude squall line with a trailing stratiform rain. *J. Atmos. Sci.*, **44,** 2128–2148.

Smull, B. F. and R. A. Houze, 1987b: Rear inflow in squall lines with trailing stratiform precipitation. *Mon. Wea. Rev.*, **115,** 2869–2889.

Stohlgren, T. J., T. N. Chase, R. A. Pielke, Sr., T. G. F. Kittel, and J. S. Baron, 1998: Evidence that local land use practices influence regional climate, vegetation, and stream flow patterns in adjacent natural areas. *Global Change Biology*, **4,** 495–504.

Tripoli, G. J. and W. R. Cotton, 1982: The Colorado State University Three-Dimensional Cloud/Mesoscale Model. Part I: General theoretical framework and sensitivity experiments. *Atmos. Res.*, **18,** 185–219.

Tripoli, G. J. and W. R. Cotton, 1989a: A numerical study of an observed orogenic mesoscale convective system. Part I: Simulated genesis and comparison with observations. *Mon. Wea. Rev.*, **117,** 273–304.

Tripoli, G. J. and W. R. Cotton, 1989b: A numerical study of an observed orogenic mesoscale convective system. Part II: Analysis of governing dynamics. *Mon. Wea. Rev.*, **117,** 305–328.

Vetterling, W. T., S. A. Teukolsky, and W. H. Press, 1992: *Numerical recipes: Example book (FORTRAN).* Cambridge University Press, 245 pp.

Walko, R. L., L. E. Band, J. Baron, T. G. F. Kittel, R. Lammers, T. J. Lee, D. Ojima, R. A. Pielke, Sr., C. Taylor, C. Tague, C. J. Tremback, and P. L Vidale, 2000: Coupled atmosphere-biophysics-hydrology models for environmental modeling. *J. Appl. Meteor.*, **39,** 931–944.

Weisman, M. L., J. B. Klemp, and R. Rotunno, 1988: Structure and evolution of numerically simulated squall lines. *J. Atmos. Sci.*, **45,** 463–485.

Weisman, M. L., W. C. Skamarock, and J. B. Klemp, 1997: The resolution dependence of explicitly modeled convective systems. *Mon. Wea. Rev.*, **125,** 527–548.

Wu, T., W. R. Cotton, and W.Y.Y. Cheng, 2000: Radiative effects on the diffusional growth of ice particles in cirrus clouds. *J. Atmos. Sci.*, **57,** 2892–2904.

Xian, Z. and R. A. Pielke, 1991: The effects of width of landmasses on the development of sea breezes. *J. App. Met.*, **30,** 1280–1304.

Yan, H. and R. A. Anthes, 1988: The effects of variations in surface moisture on mesoscale circulations. *Mon. Wea. Rev.*, **116,** 192–208.

Yang, R., M. J. Fennessy, and J. Shukla, 1994: The influence of initial soil wetness on medium-range surface weather forecasts. *Mon. Wea. Rev.*, **122,** 471–485.

Zhang, D.-L., W.Y.Y. Cheng, and J. R. Gyakum, 2002: The impact of various potential vorticity anomalies on multiple frontal cyclogenesis events. *Quart. J. Roy. Meteor. Soc.*, **128,** 1847–1877.

Zipser, E. J., 1982: Use of a conceptual model of the life cycle of mesoscale convective systems to improve very-short-range forecasts. Browning, K., editor, *Nowcasting*, pages 191–204. Academic Press.